Monitoring kinetic processes in polymeric colloids by Fluorescence Correlation Spectroscopy

Dissertation
zur Erlangung des Grades
'Doktor der Naturwissenschaften'
(Dr. rer. nat.)
im Promotionsfach Chemie

am Fachbereich Chemie, Pharmazie und Geowissenschaften
der Johannes Gutenberg–Universität Mainz

vorgelegt von

Dipl.-Ing. David Schäffel

geboren in Dresden

Mainz, 2014

Die vorliegende Arbeit wurde im Zeitraum von November 2011 bis Oktober 2014 am Max-Planck-Institut für Polymerforschung in Mainz unter der Anleitung von ... und ... angefertigt.

Tag der mündlichen Prüfung: 25. 11. 2014
Dekan: ...
Erster Berichterstatter: ...
Zweiter Berichterstatter: ...
Dritter Berichterstatter: ...

One of the principal objects of theoretical research in any department of knowledge is to find the point of view from which the subject appears in its greatest simplicity.

Josiah Williard Gibbs

Table of contents

Abstract

Polymeric colloids with sizes in the nanometer range are considered among the most promising candidates for encapsulation and the delivery of drugs. Various systems ranging from solid or nanogel particles to polymeric micelles are prepared and their properties optimized with respect to drug loading capacity, stability, long circulation times, targeted delivery and controlled release. In this endeavor, it is important to have good knowledge about the physical processes governing the formation, the structure and the kinetic stability of the polymeric colloids. However, investigating these processes, for nanometer sized objects dispersed and constantly diffusing in a continuous media is not an easy task and requires advanced experimental techniques. In this thesis I describe studies demonstrating that dual color fluorescence cross-correlation spectroscopy (DC FCCS) can provide important informations about the interaction and the exchange between dispersed nanometer sized colloids.

First, I considered the process of nanoparticle formation from emulsion droplets that is one of the most common approaches for nanoparticles preparation. I showed that DC FCCS allows to directly monitor the occurrence of coalescence between the emulsion droplets that is considered as one of the major reasons for the large size distribution of the obtained nanoparticles.

Second, I studied the equilibrium exchange of building molecules between amphiphilic diblock copolymer micelles. As a model system I choose a linear-brush block copolymer architecture forming micelles with a thin and bulky corona. Using DC FCCS I studied the exchange in different solvents and at various temperatures. Depending on the quality of solvent the exchange time can be shifted by orders of magnitude allowing extensive tuning of the molecular exchange.

A property which all these polymeric colloids have in common is their polydispersity. In the last part of my work, I explored the effect of polydispersity and fluorescent labeling in FCS experiments using polymers as model systems. I found that a suitable modification of the standard analytical FCS model can be used to describe the FCS correlation curves measured in such systems. The validity of my approach was confirmed by comparison with gel permeation chromatography experiments and Brownian dynamics simulations.

Zusammenfassung

Polymerbasierte Kolloide mit Größen im Nanometerbereich werden als aussichtsreiche Kandidaten für die Verkapselung und den Transport von pharmazeutischen Wirkstoffen angesehen. Daher ist es wichtig die physikalischen Prozesse, die die Bildung, Struktur und kinetische Stabilität der polymerbasierten Kolloide beeinflussen, besser zu verstehen. Allerdings ist die Untersuchung dieser Prozesse für nanometergroße Objekte kompliziert und erfordert fortgeschrittene Techniken. In dieser Arbeit beschreibe ich Untersuchungen, bei denen Zwei-Farben-Fluoreszenzkreuzkorrelationsspektroskopie (DC FCCS) genutzt wurde, um Informationen über die Wechselwirkung und den Austausch von dispergierten, nanometergroßen Kolloiden zu bekommen.

Zunächst habe ich den Prozess der Polymernanopartikelherstellung aus Emulsionstropfen untersucht, welcher einen der am häufigsten angewendeten Prozesse der Nanopartikelformulierung darstellt. Ich konnte zeigen, dass mit DC FCCS eindeutig und direkt Koaleszenz zwischen Emulsionstropfen gemessen werden kann. Dies ist von Interesse, da Koaleszenz als Hauptgrund für die breite Größenverteilung der finalen Nanopartikel angesehen wird.

Weiterhin habe ich den Austausch von Mizellen bildenden Molekülen zwischen amphiphilen Diblock Kopolymermizellen untersucht. Als Modellsystem diente ein Linear-Bürste Block Kopolymer, welches Mizellen mit einer dichten und kurzen Korona bildet. Mit Hilfe von DC FCCS konnte der Austausch in verschiedenen Lösungsmitteln und bei verschiedenen Temperaturen beobachtet werden. Ich habe herausgefunden, dass in Abhängigkeit der Qualität des Lösungsmittels die Zeit des Austausches um Größenordnungen verschoben werden kann, was eine weitreichende Einstellung der Austauschkinetik ermöglicht.

Eine Eigenschaft die all diese Kolloide gemeinsam haben ist ihre Polydispersität. Im letzten Teil meiner Arbeit habe ich am Beispiel von Polymeren als Modellsystem untersucht, welchen Effekt Polydispersität und die Art der Fluoreszenzmarkierung auf FCS Experimente haben. Eine Anpassung des klassischen FCS Modells kann die FCS Korrelationskurven dieser Systeme beschreiben. Die Richtigkeit meines Ansatzes habe ich mit dem Vergleich zur Gel-Permeations-Chromatographie und Brownschen Molekulardynamiksimulationen bestätigt.

1. Introduction

Our today's world is not conceivable without polymers. Their unique nature allows extensive tuning of their properties which have evoked entry in all kinds of modern human life. Polymers are abundantly used as structural materials for construction and manufacturing as well as for packaging and other every day application. Especially during the last years research on conductive polymers have impinged and boosted the development of organic solar cells.[2] Here again the properties of polymers such as mechanical flexibility and easy fabrication *e.g.* ink-jet printing or injection molding urge scientists to dream of solving humanities energy problems one day.[3]

Another current issue is the application of polymers as biomaterials. Besides nowadays well established usage of polymers *e.g.* as surgical suture material or in artificial knee and hip joint replacement,[4] particularly during the last decades the idea of encapsulating drug molecules, proteins, RNA or DNA into nanosized carriers has provoked enhanced research in this direction.[5] The injection of these kind of drug delivery agents into the organism shall on one hand facilitate the distribution within the body but on the other hand allow specific targeting and uptake. Among the various nanosized carriers, polymeric colloids are considered of being the most promising candidates.[5,6] However, the relevant properties of the polymeric colloids need to be associated with their structure and dynamical behavior. It is of importance to elucidate the pertinent mechanisms within synthesis and/or self assembly to gain access to their reliable preparation and application.[7] Regarding this, their complexity makes these kind of investigations very challenging. The intrinsic size of a few nm accompanied with dynamics in the μs-range requires advanced experimental techniques and scientific instrumentation.

In this respect, Fluorescence Correlation Spectroscopy (FCS) is offering an interesting alternative. FCS monitors fluorescence intensity fluctuations due to *e.g.* diffusion of the tracers through a very small confocal observation volume ($V < 1$ fL). Autocorrelation of the recorded fluorescence intensity signal makes diffusion coefficient and size as well as concentration of the tracers accessible. Initially FCS was developed as a tool in life sciences and biophysics where it is still predominantly

used.[8,9] However, especially during the last 15 years the technique has also found widespread application in polymer and colloid science.[10,11]

1.1. FCS to study polymeric colloids

The probably most abundantly used application of FCS is the determination of the hydrodynamic radius (R_h) from the mean decay time of the FCS autocorrelation curve using equations 2.16 - 2.18. Therefore, a prerequisite is that the observed species are fluorescent. Combining that with the single photon sensitivity provided by modern equipment, such as avalanche photo diodes, FCS allows to investigate size, concentration, aggregation and loading of colloids.[10]

Rigler and Meier[12] studied the encapsulation efficiency of nanocontainers (NCs) formed by amphiphilic triblock copolymers. As a small molecular probe they used sulforhodamine a low molecular weight fluorescent dye as well as the fluorescently marked protein avedin. The FCS autocorrelation curves provided the hydrodynamic radius of the of the single dye, avedin and the NCs. The R_h for the latter were found to be in the order of $\approx$ 75 nm. Moreover, a comparison of the fluorescent brightness of the fluorescent molecules from experiments where no NCs where present and the NCs with encapsulated species allowed the authors to estimate the amount of their encapsulation. Providing that the laser intensity was the same in the experiments the number of encapsulated molecules could be determined by dividing the fluorescent brightness of the NCs through that of the single fluorescent molecules.

In another study Jaskiewicz *et al.*[13] examined the uptake of silica (SiO_2) and polystyrene (PS) nanoparticles into polymeric bilayer vesicles formed by the amphiphilic diblock copolymer poly(dimethylsiloxane)-*block*-poly(2-methyloxazoline) (PDMS-*b*-PMOXA). The uptake constitutes a "minimal" model system for studying the adsorption and transmembrane transport in the absence of membrane proteins and polysaccharides. PS and SiO_2 possessed an R_h of 16 nm and 14 nm respectively whereas the vesicles where found to have a R_h of meanly 95 nm. Among other techniques, the authors used FCS to gain insight into the kinetics of uptake as displayed in figure 1.1. Fluorescently labeled particles were mixed with non-labeled vesicles and FCS measurements conducted. The authors investigated an increase in size from 16 nm after two minutes to roughly 100 nm after two hours verifying the

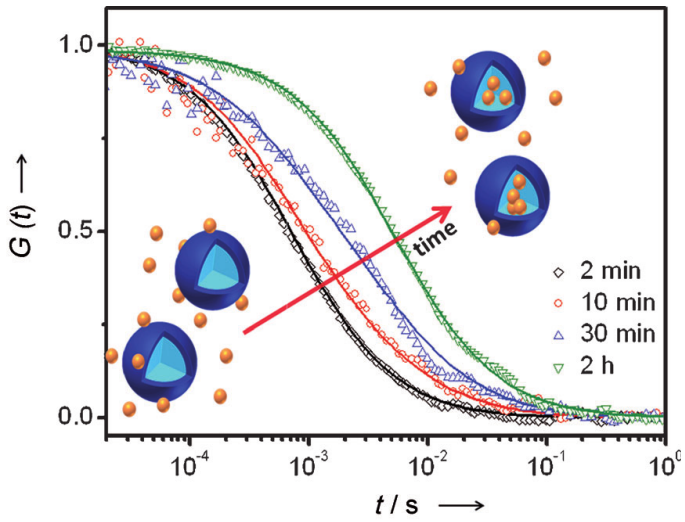

Figure 1.1: FCS autocorrelation curves of the loading of PS nanoparticles into PDMS-*b*-PMOXA bilayer vesicles. The symbols are the experimental curves whereas the lines correspond to fits. [13]

uptake of the nanoparticles into the vesicles.

Another promising candidate as drug carrier system in particular with respect to siRNA transport for gene therapy was recently presented by Nuhn and coworkers.[14] They synthesized well-defined amphiphilic reactive ester block copolymers. The polymers undergo aggregation in polar aprotic solvents such as dimethyl sulfoxide. The authors used the resulting assemblies as precursors while covalently cross-linking their hydrophobic reactive core which resulted in the formation of stabilized nanohydrogel particles. Furthermore, by stoichiometric adjusting the amount of added cross-linker additional reactive sites where maintained to further allow conjugation with siRNA. FCS experiments of single fluorescently labeled siRNA and the conjugated nanohydrogel particles verified the successful conjugation. The single siRNA provided a much smaller diffusion time and thus size than the nanohydrogel particles.

FCS was also used to determine the critical micelle concentration (CMC) in solutions of amphiphilic block copolymers as shown by Bonné *et al.*[15,16] They used a block copolymer comprising of 2-methyl-2-oxazoline and 2-nonyl-2-oxazoline as the hydrophilic and hydrophobic part, respectively. To access a broader range of copolymer concentration they mixed fluorescently labeled copolymers with non-labeled ones. At the CMC and above it is not sufficient to fit the decay of the FCS autocor-

relation curve with a single diffusion time (equation 2.15) which is corresponding to the diffusion of fluorescently labeled single polymer chains. A second, slower decay time is observed which can be associated with the diffusion of micelles as shown in figure 1.2. The same authors studied the effect of block copolymer architecture on

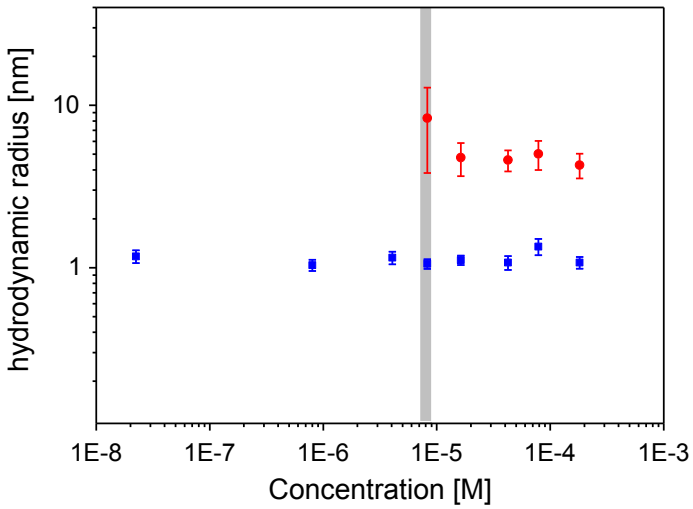

Figure 1.2: Micelle formation of Poly(2-oxazoline) copolymers in water studied by FCS. Blue squares indicate single chains whereas the red circles correspond to micelles. The CMC is emphasized with the grey bar. Labeled and non-labeled polymers were mixed. [16]

the size of micelles.[17] The hydrodynamic radius of triblock copolymers, with the hydrophobic block in the middle, was compared with the one of diblock copolymers having similar molecular weight and especially the same length of the hydrophobic block. Their findings could show that the triblock copolymers lead to micelles with a lower size. This however may be explained with steric considerations. For triblock copolymers, the hydrophobic block stretches over the whole micelle determining the core size whereas this is not the case for diblock copolymers.

1.2. Limits of classical FCS

As discussed above, nowadays FCS is more and more applied to study polymeric colloids.[8,9] When considering aggregation, binding or loading, a prerequisite of the successful application of FCS is that the interacting species may be discriminated by size. Thus, a distinct change of the R_h of the detected species before and after the

assembly is mandatory.[18] A good example is the work of Jaskiewicz *et al.*[13] which I already introduced in the last section. The uptake of comparably small fluorescent nanoparticles possessing a R_h of about 16 nm into the significantly bigger vesicles with a mean R_h of 95 nm results in a distinct size increase of the detected species (see also figure 1.1). If no significant changes of the size of the investigated species are detectable during assembly the classical FCS technique is not appropriate for their detection. A reasonable question here is of course what means significant. An experiment with sufficient statistical accuracy means the correlation of at least ~ 2 million detected photons (average count rate ~ 25 kHz during a 120 seconds measurement). Considering the Gaussian distribution of the experimental results and thus a Gaussian error propagation an typical FCS experiment yields a hydrodynamic radius commonly comprising a standard error of ~ 5 to 15 %.

Here, I will consider two thought experiments. First, the merging and thus coalescence of spherical nanodroplets which might occur constantly in emulsions. If, for example, in average two "daughter" droplets of say $R_{h.1} = 50$ nm and $R_{h.2} = 60$ nm coalesce volume conservation will lead to $R_{h.3} \simeq 69$ nm of the "mother" droplets. Another example is the association of polymers. I consider a polymer with a statistical segment length of *e.g.* $b = 0.5$ nm and a degree of polymerization $X = 500$ and assume the chains to exhibit ideal Gaussian behavior. Having the root mean square end-to-end distance vector of the chains $\sqrt{\langle \vec{r}^2 \rangle} = b\sqrt{X}$, the radius of gyration $R_g = \sqrt{\langle \vec{r}^2 \rangle / 6}$ and the relation $R_h = R_g/1.3$[19] an association of meanly two chains from $X = 500$ to 1000 would theoretically increase the hydrodynamic radius from 3.5 nm to 4.9 nm.[20]

Both examples show that for such studies the R_h should be detected with an accuracy of at least ~ 15 %. Thus, within the standard error of such an experiment of ~ 5 to 15 % the size change should still be detectable. However, all these assumption require ideal behavior and no experimental pitfalls or distortions, neither from the samples, such as occasionally occurring aggregates, nor from the setup, *e.g.* non-stable laser sources or not perfectly aligned optics. If additionally the sample exhibits a size dispersity, no in R_h will be detectable.

Thus, classical FCS, only measuring the R_h, might not be appropriate in such cases. However, another advantage of FCS is its selectivity towards fluorescently labeled species. In this respect dual-color fluorescence cross-correlation spectroscopy (DC FCCS), an enhancement of the classical FCS technique, is able to detect inter-

actions between two differently labeled species. Briefly, the fluorescence fluctuations of the two differently labeled species are recorded in two detection channels. Moreover, their associated diffusion results in similar fluorescence fluctuation signals. An intensity cross-correlation of the independently recorded signals gives a quantitative measure about the interaction process. The method was first introduced in 1997 by Schwille and coworkers.[21] Within this work the authors studied the binding of two single stranded DNA segments, both fluorescently labeled with different dyes. Moreover, they could monitor the kinetics of the DNA hybridization and deduce the kinetic rate constant.

1.3. Motivation

In this thesis I used DC FCCS to study the interaction and exchange between polymeric colloids that can not be detected by size change only. Two processes were studied. One is the preparation of polymeric nanoparticles from emulsion droplets as templates and the second is the dynamic equilibrium exchange of building molecules between diblock copolymer micelles.

Concerning the preparation of polymeric nanoparticles, the solvent evaporation process from miniemulsion droplets (SEED) is an important procedure. Here, a polymer is dissolved in an organic solvent and dispersed in an aqueous phase to form nanodroplets whereas solvent evaporation leads to the formation of nanoparticles.[22–24] Concerning medical applications, an advantage is the use of pre-polymerized polymers which results in radical and residue free nanoparticles.[30,31] However, an intrinsic drawback of the technique which considerably shrinks the possibility of application is the comparably large size distribution of the final nanoparticles. Here the question is where is the size polydispersity originating from. Dynamic light scattering (DLS) measurements reveal that coalescence is the reason.[32,33] However, measurements relying on size might be altered by *e.g.* swelling of the polymers or other artifacts. Thus, I used DC FCCS to study the influence of coalescence on the SEED process directly.[34,35]

Other colloidal systems that are considered as promising candidates for drug carrier devices are amphiphilic diblock copolymer micelles.[39–41] However, even in thermodynamic equilibrium there persists a constant exchange of building molecules be-

tween the micelles.[36–38] Yet, the exchange may influence the drug carrier properties *e.g.* stability, controlled release and loading capabilities. Thus, not only because of fundamental interest but also to further optimize and tune the properties of such micelles a better understanding of their properties is required. So far the only fully quantitative method which was applied is time resolved small angle neutron scattering (TR-SANS) which is comparably time consuming and elaborate.[44,45] I used DC FCCS to study the equilibrium chain exchange of diblock copolymer micelles comprising a bulky corona to identify the mechanism of exchange in framework of the existing theories.[46]

A property which all synthesized polymers and colloids have in common is polydispersity. Only few studies exist on how to account for polydispersity by FCS.[47–49] Moreover, it is common, and in terms of a moderate polydispersity also reliable, to use the monodisperse FCS model to fit polydisperse data.[10] However, besides the size distribution of the diffusing species, their eventual distribution of fluorescence brightness also plays an important role. I studied the influence of different fluorescent brightness distributions using polymers as a model system and introduce a new FCS model accounting for the polydispersity of polymers.

Part I.

Fundamentals

2. Fluorescence Correlation Spectroscopy

This chapter gives an overview about Fluorescence Correlation Spectroscopy (FCS). A short introduction into the history of FCS is followed by an explanation of its concepts. The basic principles of fluorescence are delineated and the experimental realization of FCS is outlined. Furthermore, the focus is set on the theory and mathematical description of the FCS autocorrelation and DC FCCS cross-correlation functions.

2.1. Historical sketch

In 1972 the principle of FCS was first described by Madge, Elson and Webb.[53] In this very first FCS publication the authors reported how they measure the binding of ethidium bromide to DNA. This was followed by concrete experimental realizations[54,55] and several works on the application of FCS to investigate *e.g.* translational diffusion,[56] rotational dynamics[57,58] and laminar flow.[59] Despite these pioneering works the potential and application of FCS remained limited due to a poor signal-to-noise ratio, non-stable laser emission, low quantum-yield fluorescent molecules and inefficient detection. An essential enhancement was the combination of the FCS principle with confocal microscopy as suggested by Rigler *et al.* in 1993.[60] The confocal principle[61] ensures a very small observation volume allowing higher concentrations of the fluorescent molecules and thus improvement of the signal-to-noise ratio. Over the years development of single-photon-counting avalanche photo-diodes (SPAD), stable laser sources as well as synthesis of more efficient high quantum yield fluorescent molecules contributed essentially to the spreading of FCS as an investigative tool within the scientific community.[62] Due to its non-invasiveness the technique has predominately established as a tool being utilized in life sciences and biophysics.[8,9] However, especially during the last decade FCS became more and more used in polymer, colloid and interface science.[10,11]

2.2. Introduction to fluorescence fluctuation analysis

For the most spectroscopic techniques the relevant information is drawn from the perturbation of the thermodynamic equilibrium of the studied system and its relaxation back to it. In FCS, fluorescent molecules are excited in order to trace the fluorescence intensity fluctuations caused *e.g.* by their local equilibrium concentration fluctuation measured in a small observation volume. Although in such an experiment only very few down to single molecules are in average inside the observation volume, FCS does no insist to measure single molecule events. Rather the autocorrelation and thus averaging over a statistically sufficient number of single molecule events ensures appropriate information about random stochastic processes such as diffusion or other molecular phenomena.[63] Taking translational diffusion as an example the fluorescence intensity fluctuations caused thereby contain information about the diffusion coefficient of the investigated species or inversely about the local viscosity of its environment. Additional information about the concentration and brightness of the species observed can be obtained.[18] Moreover a variety of processes spanning a time scale from 10^{-9} to several seconds can be studied. The only condition is that the investigated processes cause fluorescence fluctuations in thermodynamic equilibrium.[64]

Another way to analyze of the fluorescence intensity fluctuations is using the information contained within the photon count histogram (PCH). A PCH is a histogram where the number of detected photons per bin are plotted against the count of bins with a particular number of detected photons. Thereby, in a PCH a fixed bin-size is considered. Analysis includes modeling the Poisson-statistics of the fluorescent molecules inside the observation volume as well as describing the statistics of photon emission and detection.[65,66] Slightly different approaches have been developed named PCH analysis[65,67–69] and fluorescence intensity distribution analysis (FIDA).[66,70] Both enable similar capabilities of distinguishing fluorescent molecules by means of their emission properties.

2.3. Basics of fluorescence

Irradiation of molecules with light of a certain frequency ν may result in absorption of the light.[72] Considering the wave-particle dualism the energy of the absorbed light quantum or photon is quantified by $E_\mathrm{A} = h\nu_\mathrm{A}$. Thereby, absorption of microwave (MW) or infrared (IR) light results in excitation of rotational or vibrational states of the molecule. If visible (VIS) or ultraviolet (UV) light is absorbed, excitation of an electron from its electronic ground state $\mathbf{S_0}$ to an excited electronic state, *e.g.* $\mathbf{S_1}$, occurs. The process is depicted in figure 2.1 in a so-called Jablonski diagram.[71] After absorption, non-radiative relaxation to the vibrational ground state of the excited electronic state may be followed by radiative relaxation of a photon with

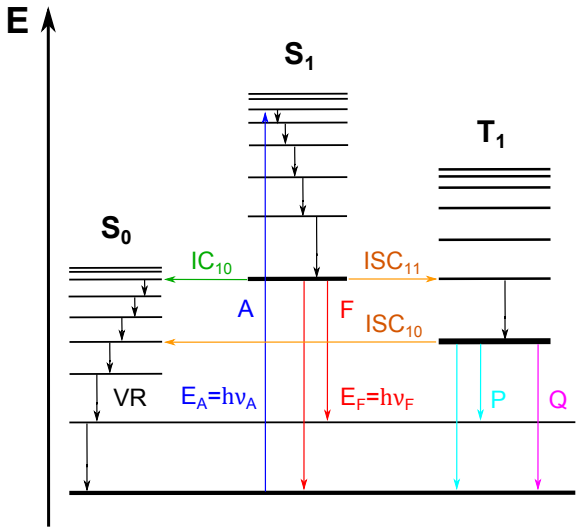

Figure 2.1: A Jablonski diagram showing the energy states of a molecule in a simplified manner. The thick lines represent the electronic and thin lines the vibrational states. After energy uptake, e.g. due to absorption A of a photon with energy $E_\mathbf{A} = h\nu_\mathbf{A}$ from the singlet ground state $\mathbf{S_0}$ to the first excited singlet state $\mathbf{S_1}$ several routes of energy dissipation back to the ground state exist. Besides vibrational relaxation VR, the molecule can emit a photon from $\mathbf{S_1}$ with energy $E_\mathbf{F} = h\nu_\mathbf{F}$ which is called fluorescence F. Another possibility is intersystem crossing ISC to a triplet state $\mathbf{T_1}$ including different multiplicities between vibrational states which may result in phosphorescence P. Internal conversion IC happens between states of similar multiplicity and energy can further dissipate via quenching Q, e.g. due to molecules collisions.[71]

lower energy $E_F = h\nu_F$ back to the electronic ground state. This process is termed fluorescence and the light which is emitted is called fluorescence light. Additionally processes such as internal conversion may result in non-radiative relaxation from higher to lower electronic states. Typical times for non-radiative relaxations are 10^{-12} s which means that in almost all cases fluorescence occurs from the lowest vibrational states of the excited electronic states since fluorescence lifetimes are in the range of $10^{-9} - 10^{-8}$ s.

The similarity between fluorescence and internal conversion is that the molecule remains within the singlet state and thus no change in net-spin of the valence electrons is present. However, spin-conversion of an electron can result in excitation of the molecule to the first triplet state $\mathbf{T_1}$ which is symmetry forbidden. So is the transition back from $\mathbf{T_1}$ to $\mathbf{S_0}$ which also results in emission of a photon and is called phosphorescence. This means that the probability of this event is very low resulting in triplet lifetimes typically orders of magnitude higher than those of fluorescence. The fluorescent molecules used within this thesis possess triplet lifetimes in the range of $10^{-6} - 10^{-5}$ s. Another process of how energy from an excited electronic state of a molecule can be dissipated involves association and interaction of different molecules and is called quenching. One example is the fluorescence resonance energy transfer (FRET).[71]

2.4. Experimental realization

An essential contribution to the break through and thus widespread application of FCS was the combination of the FCS principle with confocal microscopy as first described by Rigler and coworkers.[60] A today's FCS setup comprises an epi-illuminated converted confocal microscope[61] as schematically shown in figure 2.2. An excitation light source (blue in figure 2.2), in most cases a laser, is fiber-coupled into the confocal microscope, expanded, and colinearized to fill the aperture of the microscope objective. A dichroic mirror reflects the excitation light into the aperture of the microscope objective. In general, objectives with a high numerical aperture ($NA > 1$) are chosen to enhance the detection efficiency of the setup which is associated with low working distances of typically less then 200 μm. The objective focuses the laser beam to a diffraction limited spot into the sample resulting in excitation

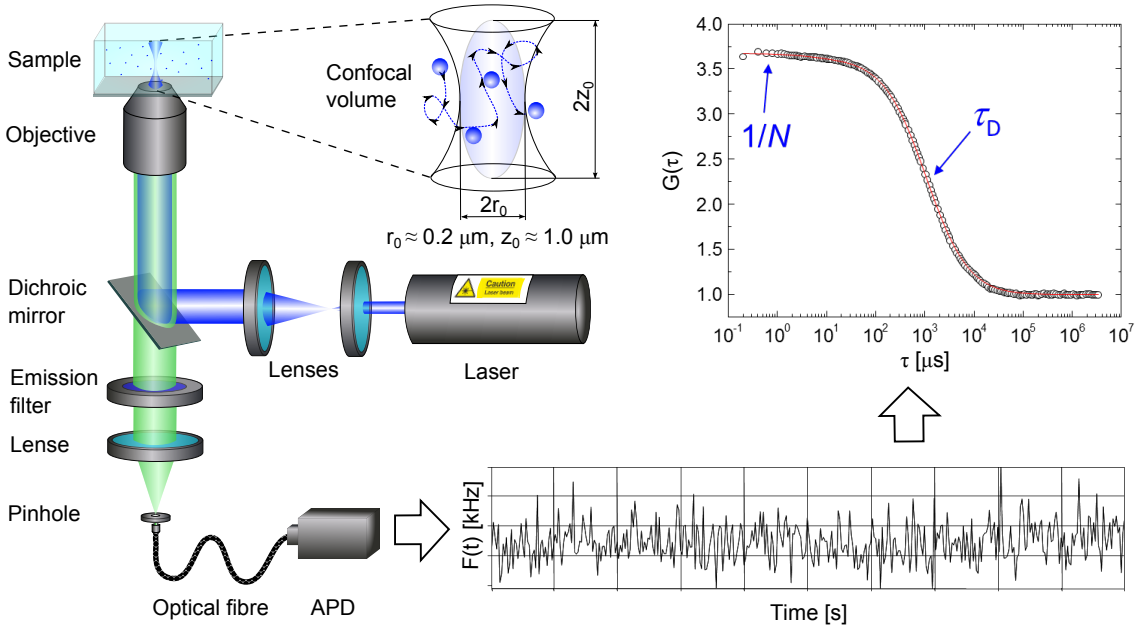

Figure 2.2: A schematic of a confocal FCS setup and its working principle. See text for details.

(see also figure 2.1) of the contained fluorescent tracers. Red-shifted fluorescence light (green in figure 2.2) is emitted and collected with the same microscope objective followed by transmission through the dichroic mirror into the detection beam path of the microscope. An emission filter ensures that scattered excitation light is almost completely stopped. Following the fluorescence in the detection beam path, the next crucial element is the pinhole which cuts off the fluorescence not coming from the focal plane within the excitation volume. Therefore, a proper adjustment of the pinhole regarding all spatial dimensions and its diameter are mandatory. The pinhole enhances particularly the axial resolution of the setup and the signal-to-noise ratio.[61] Within a well adjusted confocal FCS setup an observation volume of less than 1 fL can be achieved.[18] The small observation volume ensures high spatial resolution of the technique combined with high sensitivity towards fluorescent tracers.[62]

2.5. Theory and data analysis

The aim of a FCS measurement is the extraction of quantitative data of the observed system such as concentration, diffusion coefficient or hydrodynamic radius. In order to do so the application of an appropriate model is mandatory. Here I will give the derivation of the most important equations in FCS for the case of translational three-dimensional diffusion serving as a background for the following chapters of my thesis.[18,62–64]

2.5.1. The autocorrelation function

The general form of an intensity autocorrelation function is:[53,54,56]

$$g(\tau) = \lim_{T\to\infty} \frac{1}{T} \int_0^T I(t)I(t+\tau)d\tau = \langle I(t)I(t+\tau)\rangle \,. \tag{2.1}$$

Here T is the measurement time, $I(t)$ is the measured fluorescence intensity and τ the lag time whereby $\langle\ \rangle$ denotes the time-average. In order to derive the analytical FCS

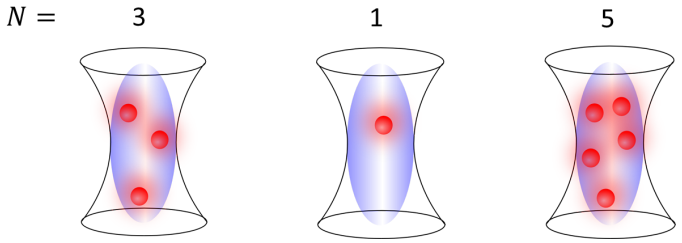

Figure 2.3: The FCS observation volume occupied by a certain number of fluorescent tracers governed by Poisson statistics.

model it is important to mention that in general the underlying processes in FCS can be considered as ergodic, meaning that the time-average equals the ensemble-average. Considering the fluorescence intensity fluctuations $\delta I(t) = I(t) - \langle I(t)\rangle$ around the mean fluorescence $\langle I(t)\rangle$ and normalization leads to the normalized form of the autocorrelation function:[18]

$$G(\tau) = \frac{\langle I(t)I(t+\tau)\rangle}{\langle I(t)\rangle^2} = 1 + \frac{\langle \delta I(t)\delta I(t+\tau)\rangle}{\langle I(t)\rangle^2}. \tag{2.2}$$

Moreover, the occupancy of the FCS observation volume (Fig. 2.2 & 2.3) by a certain number N of fluorescent tracers is governed by a Poisson distribution.[18,62]

$$P(N) = Poi(N, \langle N \rangle) = \frac{\langle N \rangle^N \exp\left(-\langle N \rangle\right)}{N!} \tag{2.3}$$

If all the intensity fluctuations $\delta I(t)$ arise due to concentration fluctuations $\delta C(t) \propto \delta N(t)$ inside the FCS observation volume than clearly $\delta I(t) \propto \delta N(t)$. Since for a Poisson distribution the variance $\sigma^2 = \langle (I(t) - \langle I(t) \rangle)^2 \rangle$ equals the mean value $\mu = \langle I(t) \rangle$, at the time $\tau = 0$ equation 2.2 reads

$$G(0) = 1 + \frac{1}{\langle N \rangle} \tag{2.4}$$

which shows that the amplitude of the autocorrelation curve $G(0)$ is inverse proportional to the mean value of fluorescent tracers inside the FCS observation volume.[73] This becomes also phenomenologically evident if we consider $G(0)$ as a display of the fluorescence fluctuations $\delta I(t)$ relative to the mean fluorescence $\langle I(t) \rangle$.

The next step towards a closed form solution of the FCS autocorrelation function is the physical description of the confocal observation volume. Therefore, we have to consider the *point spread function* (PSF) of the microscope objective. The PSF describes how a point source of light in a sample at $\vec{r}$ is transferred to an image at $\vec{r}'$.[60,61] Furthermore, we delineate the transmission function of the pinhole of the confocal microscope with a circular disk function $circ(...)$ to deduce the *collection efficiency function* (CEF)[55,74] of the optical system as the convolution of the transmission function of the pinhole and the PSF of the objective.[60,61]

$$\mathrm{CEF}(\vec{r}) = \frac{1}{\Delta} \iint_{IP} \mathrm{circ}\left(\frac{\vec{r}'}{s_0}\right) \mathrm{PSF}(\vec{r} - \vec{r}')dx'dy' \tag{2.5}$$

Here Δ is a normalization factor and s_0 is the radius of the pinhole projected into the sample which means it is the physical radius of the pinhole divided by the magnification of the objective. The convolution is done in the image plane (IP) perpendicular to the optical axis z. Multiplying the CEF with the excitation intensity I_{ex} results

in the *molecular detection efficiency* (MDE).[60]

$$\mathrm{MDE}(\vec{r}) = I_{\mathrm{ex}}(\vec{r})\mathrm{CEF}(\vec{r}) \tag{2.6}$$

A good approximation of the MDE is the so-called Gauss-Gauss-Lorentzian which models the MDE in the plane perpendicular to the optical axis with a two-dimensional Gaussian function whereas the z dependence parallel to the optical axis is modeled by a Lorentzian one.[74] This approach however, does not lead to a explicit analytical form of the desired autocorrelation function $G(\tau)$. Therefore, most frequently the MDE is sufficiently well described with a three-dimensional Gaussian which often leads to an analytical solution of $G(\tau)$.[18]

$$\mathrm{MDE}_g(\vec{r}) = \mathrm{MDE}_g(0)\ \exp\left(-2\frac{x^2+y^2}{r_0}\right)\exp\left(-2\frac{z^2}{z_0}\right) \tag{2.7}$$

z_0 and r_0 represent the axial and radial dimensions of the FCS observation volume, respectively. They are defined as the distance from the center of the Gaussian MDE to the point where the maximum intensity has decayed to the $1/e^2$ part in the particular direction. The size of the observation volume is defined as the effective volume V_{eff} which has an explicit value in case of three-dimensional Gaussian MDE:[18]

$$V_{eff} = \frac{\left(\int_\Omega \mathrm{MDE}(\vec{r})d\vec{r}\right)^2}{\int_\Omega \mathrm{MDE}^2(\vec{r})d\vec{r}} \approx \pi^{\frac{3}{2}} r_0^2 z_0 \tag{2.8}$$

where $\Omega \in \mathbb{R}^3$. Clearly, the fluorescence intensity $I(t)$ and their respective fluctuations $\delta I(t)$ are proportional to the MDE resulting in

$$I(t) = \varepsilon \int_\Omega \mathrm{MDE}(\vec{r})C(\vec{r},t)d\vec{r} \tag{2.9a}$$

$$\delta I(t) = \varepsilon \int_\Omega \mathrm{MDE}(\vec{r})\delta C(\vec{r},t)d\vec{r} \tag{2.9b}$$

with $\delta C(\vec{r},t) = C(\vec{r},t) - \langle C(\vec{r},t)\rangle$. ε is called the molecular brightness and is a variable that concatenates the excitation intensity amplitude, detection efficiency of the optical system as well as the absorption cross-section and quantum yield of the dye since these parameters are almost impossible to decouple from each other.[18,62]

For computational convenience we assume that ε is a constant. Having equations 2.9a and 2.9b in hand a conflation with equation 2.2 yields

$$G(\tau) = 1 + \frac{\int_{\Omega}\int_{\Omega'} \mathrm{MDE}(\vec{r})\mathrm{MDE}(\vec{r}')\phi(\vec{r},\vec{r}',\tau)d\vec{r}d\vec{r}'}{\langle C\rangle^2 \left(\int_{\Omega} \mathrm{MDE}(\vec{r})d\vec{r}\right)^2} \tag{2.10}$$

inasmuch as we define the concentration correlation

$$\phi(\vec{r},\vec{r}',\tau) = \langle \delta C(\vec{r}',0)\delta C(\vec{r},\tau)\rangle \tag{2.11}$$

Further, the transport of the tracers crossing the FCS observation volume has to be modeled. Considering free three-dimensional diffusion and thus Brownian motion without any convection or flow the circumstance can be described by Fick's second law of diffusion:[72]

$$\frac{\partial}{\partial\tau}\phi(\vec{r},\vec{r}',\tau) = D\nabla^2_{\vec{r}}\phi(\vec{r},\vec{r}',\tau) \tag{2.12}$$

with D being the diffusion coefficient. Having the initial condition $\phi(\vec{r},\vec{r}',\tau=0) = \langle C\rangle\,\delta(\vec{r}-\vec{r}')$, the general closed form solution of equation 2.12 can be found by Fourier transformation with respect to $\vec{r}$ resulting in[18]

$$\phi(\vec{r},\vec{r}',\tau) = \frac{\langle C\rangle}{(4\pi D\tau)^{\frac{3}{2}}}\exp\left(-\frac{(\vec{r}-\vec{r}')^2}{4D\tau}\right) \tag{2.13}$$

Applying equations 2.8 and 2.13 on equation 2.10 we obtain

$$G(\tau) = 1 + \frac{1}{\langle C\rangle\, V_{eff}\left(1+\frac{4D\tau}{r_0^2}\right)\sqrt{1+\frac{4D\tau}{z_0^2}}} \tag{2.14}$$

Finally having $\langle N\rangle = \langle C\rangle\, V_{eff}$ and defining the structural parameter S as the ratio between axial and radial dimensions of the FCS observation volume $S = z_0/r_0$ we get[18,62,64,73]

$$G(\tau) = 1 + \frac{1}{\langle N\rangle\left(1+\frac{\tau}{\tau_{\mathrm{D}}}\right)\sqrt{1+\frac{\tau}{S^2\tau_{\mathrm{D}}}}} \tag{2.15}$$

with

$$\tau_{\mathrm{D}} = \frac{r_0^2}{4D} \tag{2.16}$$

being the lateral diffusion time of the fluorescent species through V_{eff}. The Stokes-Einstein equation[72]

$$R_{\mathrm{h}} = \frac{k_{\mathrm{B}}T}{6\pi\eta D} \tag{2.17}$$

relates the hydrodynamic radius R_{h} with the diffusion coefficient D whereby η is the solvent viscosity, k_{B} the Boltzmann-constant and T the absolute temperature. It has been shown by Starchev *et al.* that for species larger than a few tens of nanometers the size of the observed species has to be taken into account while relating diffusion coefficient and diffusion time:[75]

$$\tilde{\tau}_{\mathrm{D}} = \frac{r_0^2 + R_{\mathrm{h}}^2}{4D} \tag{2.18}$$

2.5.2. Multiple species FCS

A more general form of the FCS autocorrelation function (Eq. 2.15) considers different non-interacting species with individual diffusion times $\tau_{\mathrm{D}i}$ which may also exhibit individual molecular brightnesses ε_i respectively.

$$G(\tau) = 1 + \frac{\sum_{i=1}^{n} M_i(\tau;\tau_{\mathrm{D}i}) \langle N_i \rangle \varepsilon_i^2}{\left(\sum_{i=1}^{n} \langle N_i \rangle \varepsilon_i\right)^2} \tag{2.19}$$

Here $M_i(\tau;\tau_{\mathrm{D}i})$ considers the motion type e.g. diffusion or additional convection. Table 2.1 gives an overview about the most common motion types. For any further description and detailed derivations I refer to the literature.[18,53,54,56,59,60,76–84]
Equation 2.19 considers a discrete number of n species with different motion types $M(\tau;\tau_{\mathrm{D}})$ and possibly different brightnesses ε_i. However, certain species investigated with FCS such as emulsion droplets, nanoparticles and polymers may exhibit a continuous distribution of their size and thus diffusion times.[47,49] We can consider the continuous case of equation 2.19 by introducing a distribution function

$$\int_0^\infty P(\tau_{\mathrm{D}}) d\tau_{\mathrm{D}} = 1 \tag{2.20}$$

Table 2.1: Description and analytical solutions of the most common FCS motion types.

Motion type	$M(\tau;\tau_D)$
free 3D diffusion [18,53,54,56,60]	$\frac{1}{\left(1+\frac{\tau}{\tau_D}\right)\sqrt{1+\frac{\tau}{S^2\tau_D}}}$
free 2D diffusion [53,76]	$\frac{1}{\left(1+\frac{\tau}{\tau_D}\right)}$
convection and free 3D diffusion [59,77,78]	$\frac{1}{\left(1+\frac{\tau}{\tau_D}\right)\sqrt{1+\frac{\tau}{S^2\tau_D}}}\exp\left[-\left(\frac{\tau}{\tau_f}\right)^2\frac{1}{\left(1+\frac{\tau}{\tau_D}\right)}\right]$
3D diffusion in an evanescent field [79–84]	$\frac{1}{4\left(1+\frac{S^2\tau}{\tau_D}\right)}\left[\left(1-\frac{\tau}{2\tau_D}\right)\exp\left(\frac{\tau}{4\tau_D}\right)erfc\left(\sqrt{\frac{\tau}{4\tau_D}}\right)+\sqrt{\frac{\tau}{\pi\tau_D}}\right]$

such as e.g. a Gaussian or Schulz-Zimm distribution taking into account the particular problem. A complete treatment in this issue results in:

$$G(\tau)=1+\frac{\int_0^\infty M(\tau;\tau_D)P(\tau_D)\varepsilon(\tau_D)^2d\tau_D}{\langle N\rangle\left(\int_0^\infty P(\tau_D)\varepsilon(\tau_D)d\tau_D\right)^2}. \tag{2.21}$$

A more profound discussion concerning this topic is given in another part of my thesis (7).

2.5.3. Triplet contribution

The transport processes described may not be the single source of fluorescence fluctuation that are detectable in a FCS experiment. Considering single molecule emitters such as dyes, an excitation of the dye from the ground singlet state to an excited singlet state may lead to intersystem crossing to a triplet state [71] (see also Fig. 2.1). In contrast to the mean residence time of the electron in the excited singlet state also described as fluorescence lifetime which is typically in the range of a few ns [71] the triplet-lifetime can be orders of magnitude larger. [62] Common commercially avail-

able dyes such as e.g. Rhodamine6G® or AlexaFluor488® exhibit triplet-lifetimes between 1 and 10 μs. As long as a fluorescent dye remains in a triplet state it cannot be excited and thus appears to be dark. Comprising the ensemble temporally measured this results in a fraction not excitable, apparently leading to a rise of the amplitude of the autocorrelation function $G(0)$.[18] In a FCS autocorrelation curve the triplet is conspicuous as an additional decay (Fig. 2.4). Deriving an analytical

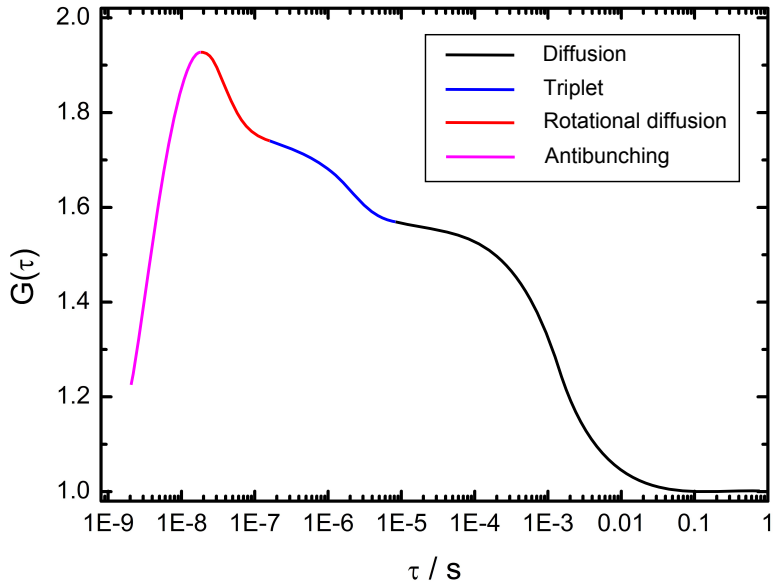

Figure 2.4: Scheme of an FCS curve highlighting the different photo-physical and dynamic processes detectable at different time-scales.

description for the triplet decay in the FCS autocorrelation curve includes modeling the rate equations for the system undergoing singlet-singlet, singlet-triplet and triplet-singlet transitions and adding this source of fluctuations to the Diffusion-equation (Eq. 2.12). Solving this problem is mathematically cumbersome and for a detailed derivation I refer to the literature.[85,86] However, the solution may be written as:

$$G_{\mathrm{T}}(\tau) = 1 + \frac{f_{\mathrm{T}}}{1 - f_{\mathrm{T}}} \exp\left(-\frac{\tau}{\tau_{\mathrm{T}}}\right). \tag{2.22}$$

Here the triplet contribution is characterized by the triplet-lifetime τ_{T} and the triplet-fraction f_{T} describing the mean fraction of fluorescent molecules excited to the triplet state. Inasmuch as no altering of the diffusion properties of the observed species occurs equation 2.15 may be combined with equation 2.22 to yield a

triplet-rectified FCS autocorrelation function:[18]

$$G(\tau) = 1 + \left[1 + \frac{f_{\mathrm{T}}}{1 - f_{\mathrm{T}}} \exp\left(-\frac{\tau}{\tau_{\mathrm{T}}}\right)\right] \frac{1}{\langle N \rangle} M(\tau; \tau_{\mathrm{D}}). \tag{2.23}$$

2.5.4. Rotational dynamics

Performing FCS experiments with linearly or circularly polarized lasers can result in what is known as "photoselection" meaning the preferential absorption of polarized laser light oscillating parallel to the absorption dipole of the fluorescent molecule.[57,62,87] Therefore, in the temporal magnitudes of typically $10^{-8} - 10^{-7}$ s fluorescence intensity fluctuations can occur which may give additional raise in the autocorrelation curve as shown in figure 2.4. This contribution reflects the rotational dynamics of the observed fluorescent molecule. Since the mathematical derivation turns out to be elaborate and within my thesis I did not study rotational dynamics I refer to the literature.[57,58,87–89] However, if the fluorescent lifetimes are much smaller than the rotational diffusion of the fluorescent molecules and they posses an approximately spherical shape as a first order approximation a single exponential decay has been proposed:[87,89–91]

$$G_{\mathrm{rot}} = 1 + \rho \exp\left(-\frac{\tau}{\tau_{\mathrm{rot}}}\right). \tag{2.24}$$

Here τ_{rot} represent the rotational correlation-time[90] whereas as a first order approximation $\tau_{\mathrm{rot}} = 1 \backslash (6 D_{\mathrm{rot}})$ with D_{rot} being the rotational diffusion coefficient.[58] ρ is a factor which depend on the geometry of the experiment and the degree of polarization of the fluorescent molecule.[91] As for the case of triplet the rotation-term can be added as a factor to the autocorrelation function.[87,90]

2.5.5. Antibunching

The fastest phenomenon that can be investigated with FCS is the so-called photon-antibunching which is distinguishable in a drop of the correlation function at very short times ($< 10^{-8}$ s) as depicted in figure 2.4.[92] Photon-antibunching is a direct evidence for the particle interpretation of light and thus for its quantum mechanical nature.[93,94] In a simple picture, after excitation a single fluorescent molecule emits

a photon. Afterwards a finite time has to elapse depending on the probability of excitation until the molecule is excited again. Moreover, after excitation in average the fluorescence-lifetime of the molecule vanishes until fluorescent relaxation to the ground state occurs.[95] This means that the shorter the times get ($\tau \rightarrow 0$), the probability of detecting a photon in an FCS experiment vanishes and therefore no correlation is feasible. The contribution of antibunching to the FCS autocorrelation function can be modeled by the following exponential dependency:[92,94,96]

$$G_{\mathrm{AB}} = 1 - \exp\left(-\frac{\tau}{\tau_{\mathrm{AB}}}\right). \tag{2.25}$$

At this point it is necessary to mention that the typical timescales of photon-antibunching ($10^{-9} - 10^{-8}$ s) and rotational diffusion ($10^{-8} - 10^{-7}$ s) are not accessible with a conventional FCS setup comprising one APD. The apparent dead-time of an APD which lies at round 10^{-7} s mainly due to the electronic signal processing induces these temporal limitations. To access times below the dead-time of an APD two photo-diodes in an Hanbury Brown and Twiss setup are necessary.[97–99] Briefly, the emitted fluorescence is separated into two independent detection channels, each compromising an APD and a time-correlated single photon counting card (TCSPC) for synchronized data acquisition. Cross-correlation (Eq. 2.27) of the data detected in the two channels results in what is known as full correlation FCS (fcFCS)[92,96,100] containing information of times below the dead time of a single APD. Finally concatenating the contributions of antibunching, rotational diffusion, triplet, and translational motion a fcFCS function reads:

$$\begin{aligned} G(\tau) =& 1 + \left[1 - \exp\left(-\frac{\tau}{\tau_{\mathrm{AB}}}\right)\right]\left[1 + \rho\exp\left(-\frac{\tau}{\tau_{\mathrm{rot}}}\right)\right] \\ & \left[1 + \frac{f_{\mathrm{T}}}{1 - f_{\mathrm{T}}}\exp\left(-\frac{\tau}{\tau_{\mathrm{T}}}\right)\right]\frac{1}{\langle N\rangle}M(\tau;\tau_{\mathrm{D}}). \end{aligned} \tag{2.26}$$

2.6. Dual-color Fluorescence Cross Correlation Spectroscopy

Cross-correlation analysis may be seen as a more general approach of what I have described in the previous chapters although with respect to FCS it can be regarded as a modification of the conventional form of the technique. One purpose is that intrinsic properties or artifacts of the excitation or detection devices, *e.g.* "Afterpulsing" of the photo-diode are circumvented to be non-present in the analysis.[62] In principle cross-correlation analysis involves correlation of two independently obtained fluorescence intensity traces. These intensity traces may be recorded by different independent detection devices or discriminated computationally by software due to emission properties such as fluorescence lifetime requiring TCSPC.[101]

Besides a huge spectrum of variations the most abundantly used variants of FCCS are dual-beam cross-correlation where two observation volumes are created and spatially separated in direction of a flow[102] and dual-color FCCS. The latter technique was first described and experimentally implemented in 1997 by Schwille and coworkers.[21] As the name already distinguishes it involves excitation with two different wavelength lasers. An overview about dual-color FCCS will be given in the following chapters.

2.6.1. The DC FCCS setup

The DC FCCS setup comprises of a confocal microscope as does the conventional FCS. A schematic of the setup and its working principle is shown in figure 2.5. Two laser beams of different wavelength shown and named "blue" and "red" for simplicity are simultaneously collimated into the microscope. A dichroic mirror reflects both excitation beams into the back aperture of an objective which focuses them into the sample. Here it is of importance that both foci are spatially overlapping forming one "common" observation volume. The sample contains two types of fluorescently labeled tracers: one excitable with the "blue" and the other excitable with the "red" laser. Both types of fluorescent labels are excited and their fluorescence collected with the same objective. The dichroic mirror transmits the fluorescence light which further passes the pinhole and another dichroic mirror separating the fluorescence of the "blue" and "red" tracers into two independent detection chan-

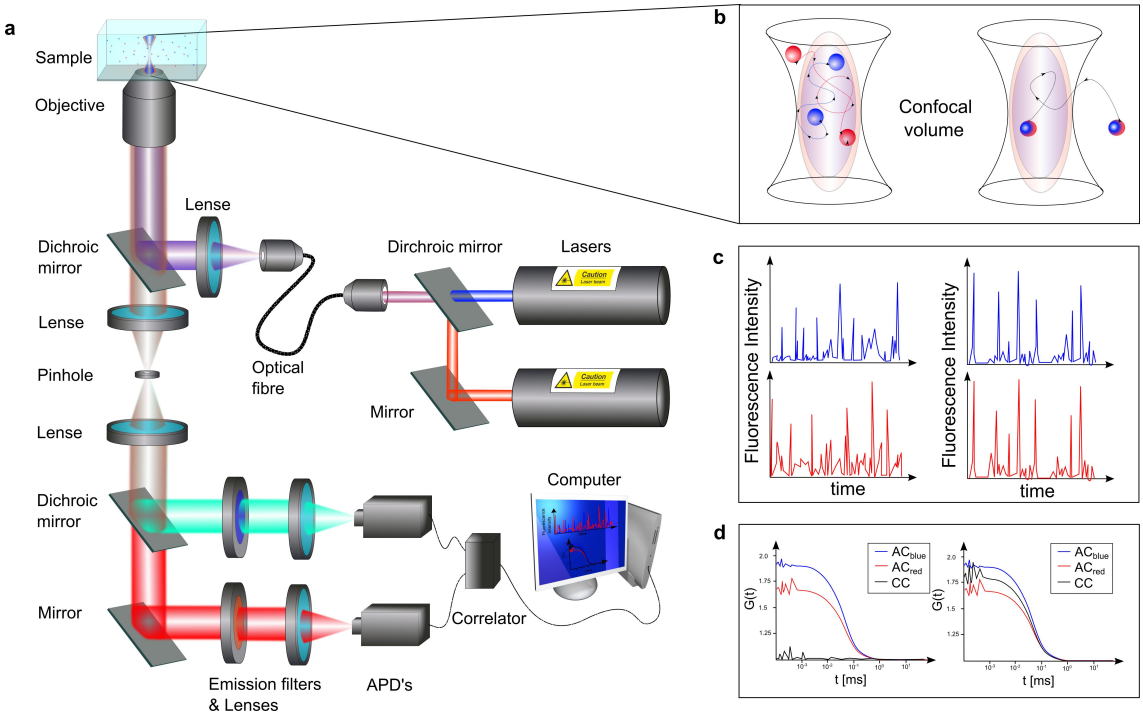

Figure 2.5: (a) Schematic setup of dual-color FCCS. (b) The two spatially overlapping observation volumes created by the "blue" and "red" laser with differently labeled species diffusing either independently (left) or linked (right). (c) Fluorescence fluctuation and the (d) corresponding correlation curves in relation to b.

nels each comprising a photo diode. The fluorescent traces of "blue" and "red" are simultaneously recorded and cross-correlated either by hardware or software.

Regarding the fluorescent species, two extreme cases are conceivable (Fig. 2.5b). First, the differently labeled fluorescent species are diffusing independently through the observation volume. Second, only dual-colored species are present. The latter case results in a huge coincidence between both intensity traces whereas almost no concurrency is detectable when the "blue" and "red" species are diffusing independently (Fig. 2.5c). Cross-correlation (Eq. 2.27) of the intensity traces results in a cross-correlation curve being almost zero for only single-colored species being present and significantly higher for dual-colored species (Fig. 2.5d). Additionally the autocorrelation curves of both channels are obtained.

2.6.2. The cross-correlation function

In similarity to equation 2.2 the cross-correlation function reads:[21]

$$G_{\mathrm{CC}}(\tau) = \frac{\langle I_1(t) I_2(t+\tau)\rangle}{\langle I_1(t)\rangle \langle I_2(t)\rangle} = 1 + \frac{\langle \delta I_1(t) \delta I_2(t+\tau)\rangle}{\langle I_1(t)\rangle \langle I_2(t)\rangle}. \tag{2.27}$$

with $I_1(t)$ and $I_2(t)$ being the measured fluorescence intensity and $\delta I_1(t)$ as well as $\delta I_2(t)$ the fluorescence intensity fluctuations in channel 1 and 2 respectively.

Any time when light interacts with matter and faces refractory index changes diffraction occurs. Diffraction limits the resolution and thus the smallest theoretical achievable dimensions of the FCS observation volume. The radial resolution of a confocal microscope reads[61]

$$r_{\min} = \frac{0.61\bar{\lambda}}{NA} \tag{2.28}$$

and in axial direction[61]

$$z_{\min} = \frac{1.5n\bar{\lambda}}{NA^2} \tag{2.29}$$

Here $\bar{\lambda}$ considers the excitation and emission wavelength which may be approximated as the geometric mean $\bar{\lambda} \approx \sqrt{\lambda_{\mathrm{ex}}\lambda_{\mathrm{em}}}$. NA is the numerical aperture of the objective with $NA = n\sin\alpha$ where n is the refractory index of the immersion liquid and α half of the opening angle of the microscope objective. Equations 2.28 and 2.29 show that the dimensions of the V_{eff} depend on wavelength. Thus, in accordance to equation 2.8 for the effective "common" volume $V_{eff.\mathrm{x}}$ in the DC FCCS case we can write[21]

$$V_{eff.\mathrm{X}} = \frac{\int_\Omega \mathrm{MDE}_1(\vec{r})d\vec{r} \int_\Omega \mathrm{MDE}_2(\vec{r})d\vec{r}}{\int_\Omega \mathrm{MDE}_1(\vec{r})\mathrm{MDE}_2(\vec{r})d\vec{r}} \approx \pi^{\frac{3}{2}} \frac{(r_1^2 + r_2^2)}{2} \sqrt{\frac{(z_1^2 + z_2^2)}{2}} \tag{2.30}$$

taking into account diffraction and the resulting different sized observation volumes $V_{eff.1}$ and $V_{eff.2}$ created due to the different wavelength lasers. Considering different types of motions (see also table 2.1) and species while remembering equation 2.19, the general form of the autocorrelation functions of the independent signals of the two detection channels read[103]

$$G_{\mathrm{AC}.1}(\tau) = 1 + \frac{\sum_{i=1}^{m} M_{1.i}(\tau;\tau_{\mathrm{D}i}) \langle C_{1.i}\rangle \varepsilon_{1.i}^2}{V_{eff.1} \left(\sum_{i=1}^{m} \langle C_{1.i}\rangle \varepsilon_{1.i}\right)^2} \tag{2.31a}$$

$$G_{\mathrm{AC}.2}(\tau) = 1 + \frac{\sum_{j=1}^{n} M_{2.j}(\tau;\tau_{\mathrm{D}j})\,\langle C_{2.j}\rangle\,\varepsilon_{2.j}^{2}}{V_{eff.2}(\sum_{j=1}^{n}\langle C_{2.j}\rangle\,\varepsilon_{2.j})^{2}}. \tag{2.31b}$$

Here the sums also include the double-labeled species and the numbers either 1 or 2 indicate the respective detection channel. Similarly the cross-correlation can be written as:[103]

$$G_{\mathrm{CC}}(\tau) = 1 + \frac{\sum_{k=1}^{o} M_{\mathrm{x}.k}(\tau;\tau_{\mathrm{D}k})\,\langle C_{\mathrm{x}.k}\rangle\,\varepsilon_{1.k}\varepsilon_{2.k}}{V_{eff.\mathrm{x}}\,(\sum_{i=1}^{m}\langle C_{1.i}\rangle\,\varepsilon_{1.i})\,(\sum_{j=1}^{n}\langle C_{2.j}\rangle\,\varepsilon_{2.j})} \tag{2.32}$$

where the subscript x denotes only the double-labeled species with quantity o having $o \leq m$ and $o \leq n$.

Since the cross-correlation curve does only appear when a significant amount of dual-colored species with respect to the single-colored ones is present in the sample, the sole occurrence of a cross-correlation immediately enables a tentative statement. However, to be more predictive we have to deduce an expression for straightforward calculation of the absolute value of the concentration of dual-labeled species. This requires the assumption that all species of a "color" possess the same fluorescent brightness.[21] Thus, the amplitudes of the correlation curves can be written as:

$$G_{\mathrm{AC}.1}(0) = 1 + \frac{1}{V_{eff.1}\,(\sum_{i=1}^{m}\langle C_{1.i}\rangle)} \tag{2.33a}$$

$$G_{\mathrm{AC}.2}(0) = 1 + \frac{1}{V_{eff.2}(\sum_{j=1}^{n}\langle C_{2.j}\rangle)} \tag{2.33b}$$

$$G_{\mathrm{CC}}(0) = 1 + \frac{\sum_{k=1}^{o}\langle C_{\mathrm{x}.k}\rangle}{V_{eff.\mathrm{x}}\,(\sum_{i=1}^{m}\langle C_{1.i}\rangle)\,(\sum_{j=1}^{n}\langle C_{2.j}\rangle)}. \tag{2.33c}$$

Inserting 2.33a and 2.33b into 2.33c results in

$$G_{\mathrm{CC}}(0) = 1 + \frac{V_{eff.1}V_{eff.2}\,[G_{\mathrm{AC}.1}(0)-1]\,[G_{\mathrm{AC}.2}(0)-1]\sum_{k=1}^{o}\langle C_{\mathrm{x}.k}\rangle}{V_{eff.\mathrm{x}}} \tag{2.34}$$

showing that inasmuch as no altering of the fluorescent properties, no chemical reactions and no fast exchange of fluorescent molecules between the dual-colored species occurs, the amplitude of the cross-correlation curve is direct proportional to the concentration of dual-colored species: $G_{\mathrm{CC}}(0) \propto \sum_{k=1}^{o}\langle C_{\mathrm{x}.k}\rangle$.[18,21,62,103] This means by

knowing the concentrations of the single-colored species (therein the dual-colored are included) due to their amplitudes (Eq. 2.4) and careful reference measurements to obtain size and shape of the observation volumes, the concentration of dual-colored species can be calculated.

2.6.3. Volume overlap and cross-talk

As stated above a DC FCCS experiment and the desired quantitative evaluation of dual-colored species requires an accurate determination of the observation volume as well as consideration of setup related aspects being *a priori* present. A very important requirement for correct application of DC FCCS is the knowledge about overlap of the observation volumes. The figure of the DC FCCS setup (Fig. 2.5) shows how the alignment should ideally be: The shorter wavelength observation volume lies completely inside the higher wavelength one. However, this does not need to be the case since *e.g.* dispersion of the optics, insufficient correction for chromatic aberration, or misalignment of the pinhole(s) can lead to not fully overlapping observation volumes as shown in figure 2.6.[103,104] Consequently, the

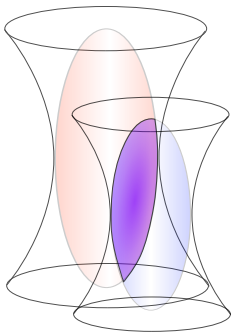

Figure 2.6: A scheme of a misaligned DC FCCS setup with not fully overlapping observation volumes.

volume where dual-colored species create similar fluorescence intensity fluctuations in both channels (the purple area in figure 2.6) is smaller as theoretically expected. Thus, $G_{\mathrm{CC}}(0)$ will be lower with respect to $G_{\mathrm{AC.1}}(0)$ and $G_{\mathrm{AC.2}}(0)$ as for the fully overlapping case revealing an apparently lower concentration of dual-colored species. However, a good approximation and straightforward way of facing this problem is the introduction of a correction factor K into equation 2.34 correcting for the false

negative cross-talk:[103]

$$G_{\mathrm{CC.K}}(0) = 1 + K\frac{V_{eff.1}V_{eff.2}\left[G_{\mathrm{AC.1}}(0)-1\right]\left[G_{\mathrm{AC.2}}(0)-1\right]\sum_{k=1}^{o}\langle C_{\mathrm{x}.k}\rangle}{V_{eff.\mathrm{x}}}. \tag{2.35}$$

The approach requires a sample containing only dual-colored species. Since for a 100 % double-colored sample $\sum_{k=1}^{o}\langle C_{\mathrm{x}.k}\rangle = \sum_{i=1}^{m}\langle C_{1.i}\rangle = \sum_{j=1}^{n}\langle C_{2.j}\rangle$ with $o = m = n$ a K-factor between 0 and 1 can be deduced.

So far we have tacitly assumed that the emission spectra of the differently colored fluorescent species do not overlap and strictly splitting into the respective detection channels occurs with "perfect" optical elements. This does not need to be completely fulfilled in a real experiment resulting particularly in detection of the shorter wavelength fluorescence in the detector which intrinsically shall only detect the longer wavelength fluorescence.[21,71,104] This phenomenon is called detector cross-talk and results in a false raise of $G_{\mathrm{CC}}(0)$ revealing artificially a higher concentration of dual-colored species. A straightforward approach is a rectification of $G_{\mathrm{CC}}(0)$ after measurement as demonstrated by Bacia and Schwille.[104] First, the undesired cross-talk has to be specified using a sample which only contains the species emitting at a shorter wavelength. The fluorescence is recorded in both channels to determine the detector bleed-through $\kappa_{1/2}$ in a calibration measurement:

$$\kappa_{1/2} = \frac{F_2^{cal.}}{F_1^{cal.}} \tag{2.36}$$

Here the subscripts describe the "color" and 1 means the shorter wavelength. F is the count-rate, thus the photon counts per second detected in the respective channels 1 and 2. The second step is the definition of the detector cross-talk rectified cross-correlation amplitude:[104]

$$G_{\mathrm{CC.CT}}(0) = G_{\mathrm{AC.1}}(0)\frac{\left[\left(\frac{G_{\mathrm{CC}}(0)}{G_{\mathrm{AC.1}}(0)}\right) - \kappa_{1/2}\left(\frac{F_1}{F_2}\right)\right]}{\left[1-\kappa_{1/2}\left(\frac{F_1}{F_2}\right)\right]}. \tag{2.37}$$

An important remark here is that a "complete" rectification also includes the detector cross-talk correction of the sample with 100 % dual-colored species used for the overlap determination and evaluation of the K-factor (Eq. 2.35).

2.7. Artifact suppressing

FCS and DC FCCS experiments are often distorted by artifacts, aggregates or other undesired signals especially when measuring in complex systems. A typical way of overcoming this dilemma is splitting the time trace T into n time intervals and individual correlation followed by hand-selection of the good curves and averaging whereas the distorted ones are discarded. This approach although possible with the standard software has several disadvantages. First, hand-selection is subjective and in principle scientifically not reliable. Second, hand-selection can become extremely cumbersome when several dozens or even hundreds of curves are recorded. And third, hand-selection does not enable small ΔT or, with other words, a splitting into a huge number of curves n since this results in enormous time consumption.

A much faster and better way especially when dealing with a huge number of curves is the automation of the splitting and in particular of the rejection. Within my thesis I implemented a standard multi-tau algorithm[105] as MATLAB® script which allows to be flexible towards starting bin-time and bin-time doubling rates. Moreover I wrote a program able to split the Zeiss-ConfocCor 2® raw-data in n user-defined time-intervals ΔT. Typically I chose a ΔT of 0.5 s revealing 600 curves for usual 300 s measurement. Then each ΔT is independently correlated and the data stored. The following important step is the evaluation of the goodness of the data which is based on[106]

$$dG_k(\tau_i) = \left\langle \left(G_k(\tau_i) - \langle G_j(\tau_i) \rangle_{j \neq k} \right)^2 \right\rangle_i . \tag{2.38}$$

dG_k is thereby a measure of the difference or deviation of a curve k from the others ($dG_k = 0$ is the mean). The next step is the determination of the maximum dG_k which is named dG_{max} and sorting of the dG_k's. Normalization from $dG_{max} = 1$ and $dG_{mean} = 0$ is followed by a user defined setting of a threshold between 0 and 1 above which the curves are discarded. Since often a lot of curves are discarded, I implemented the possibility to increase the starting bin-time to accelerate correlation. Typically I chose $\tau_{min} = 1$ μs for the goodness-evaluation and after the rejection step I re-correlate the remaining curves with $\tau_{min} = 0.2$ μs for a better resolution.

A slightly different way of applying the algorithm does not use the squaring as in

equation 2.38 but maintains the algebraic signs of the dG_k's:

$$dG_k(0) = \left\langle \left(G_k(\tau_i) - \langle G_j(\tau_i) \rangle_{j \neq k} \right) \left| G_k(\tau_i) - \langle G_j(\tau_i) \rangle_{j \neq k} \right| \right\rangle_i \tag{2.39}$$

In general the routine works similar to the one described above. However the user is now able to set an upper and a lower threshold between 1 and -1. This allows not only discarding distorted curves, but also to keep especially the ones which lag in similarity to the most.

Applying the algorithm on DC FCCS data is straightforward. The only difference is that the rejection of a curve of channel "1" does also depend on the quality of the respective curve of channel "2" and vice versa.

3. Polymeric colloids

This chapter is introduced by a brief definition of colloids. Alteration mechanism and strategies for its prevention are presented. Moreover emulsions and polymeric nanoparticles and their fabrication especially important in terms of my thesis are discussed. As another example for polymeric colloids, diblock copolymer micelles are considered. Therefore the fundamental thermodynamics and scaling analysis are delineated to conclude with a description of the dynamic equilibrium of diblock copolymer micelles.

3.1. Introduction to colloidal systems

Colloidal system are heterogeneous systems which consist of a continuous phase in which another phase is dispersed.[107,108] These phases are named continuous and dispersed phase. Our everyday life is influenced by such systems. Fog for example is an aerosol, a colloidal dispersed system in which water droplets are dispersed in a continuous gas phase. Another well-known colloidal system is milk a liquid-liquid dispersion or emulsion. Distributed solid particles in a continuous liquid phase, *e.g.* blood, ink and paint, are known as suspensions. Colloids possesses sizes between several nm up to μm which influence strongly their properties. In principle, when the diameter of the colloids is higher than half of the wavelength of the lower limit of visible light, scattering leads to an optically turbid dispersion. Once the dimensions go down to molecular sizes ($<$ nm) the mixture is homogeneous and is called true solution. From the thermodynamic point of view a true solution possesses a negative change of Gibbs free energy of mixing $\Delta G_{\mathrm{m}} < 0$. In contrast thereto, for all kinds of colloidal dispersed systems ΔG_{m} is positive since otherwise the phases would dissolve in each other.[72,109,110]

A heterogeneous system consisting of at least two phases implies the existence of an interface. It is defined as the area where different kinds of molecules adjoin each other.[111] Every kind of molecule induces forces in all spatial directions which are meanly counterbalanced by the surrounding molecules of similar kind in the bulk. However, different molecules induce different forces which means at an interface the

forces are not counterbalanced resulting in an effective tension of the interface σ_A and an interfacial energy γ_A. Considering again the change of Gibbs free energy, ΔG is proportional to the change of interfacial area: $\Delta G = \gamma_A \Delta A$. Thus, any reduction of interfacial area $-\Delta A$ leads to an reduction of $-\Delta G$ and is by means of thermodynamics favorable.[107,108] Colloids possess of a very high surface area which makes their properties so unique and interesting. This is the reason why stabilization against any type of reduction of interfacial area is required which will be discussed in the following section.

3.2. Altering & stabilization of colloids

Stability of colloidal systems is a crucial requirement for maintenance of their properties. As stated above the "global" reason for a reduction of interfacial area is the reduction of Gibbs free energy.[72] However, local interactions such as electrostatic ones are the reason for approach and finally aggregation.[112] In emulsions, coalescence may follow.[113] In the following subsections I will give a short overview about electrostatic interactions of colloids being actually the reason for aggregation and a discussion of how they can be overcome. Osmotic pressure differences inducing Oswald ripening[114] and the prevention of it will also be discussed.

3.2.1. Attraction between colloids

One reason for interaction between colloids are forces due to the interactions of dipoles, so-called Van der Waals (VdW) forces.[72] As shown by Hamaker in 1937 having no ion-coverage or -shielding the interactions between similar kind of colloids will always be attractive inasmuch as no overlapping of the electron orbitals is considered.[115] Moreover there are three different kinds of VdW forces existing. One is, permanent dipoles such as *e.g.* methanol interact and induce alignment of the different polar endings towards each other (Keesom-interactions). So called Debye-interactions mean the induction of dipoles to non-polar polarizable molecules due to the interaction with polar molecules possessing a dipole moment. Furthermore, besides permanent dipoles, oscillation of electrons may induce spontaneous fluctuations of the electronic charge density even in non-polar molecules resulting in the exhibition of temporal dipole moments which further interact with other polar and

non-polar molecules.[116] However, considering single dipoles, *e.g.* single molecules the VdW-potential $U_{\mathrm{VdW}}(D)$ for all the interactions shows a very steep dependence on separation D such as:[111]

$$U_{\mathrm{VdW}}(D) = -\frac{C_{\mathrm{VdW}}}{D^6}. \tag{3.1}$$

Here C_{VdW} accounts for the above mentioned interaction type and their particular contributions. Coming from single dipoles to ensembles of molecules such as colloids, all interactions of each molecule of a colloid with the molecules of the interacting colloid and vice versa have to be considered.[115] Treating this problem mathematically, the colloid surfaces are approximated as being flat resulting in:

$$U_{\mathrm{VdW}}(D) = -\frac{\pi^2 C_{\mathrm{VdW}} \rho_1 \rho_2}{12\pi D^2}. \tag{3.2}$$

Where $\pi^2 C_{\mathrm{VdW}} \rho_1 \rho_2$ is also known as the Hamaker-constant A_{H} with ρ_i being the respective densities.[115] Importantly, the interaction potential between two colloids approximated as two flat surfaces decays with a $1/D^2$ dependency leading to a much longer ranged attraction than for single molecules.

3.2.2. Strategies for stabilization of colloids

Considering charged surfactants adsorbing to the interface of colloids, their charge will lead to electrostatic repulsion between them. However, within a continuous phase in which ions are dissolved, due to multiple ion shielding effects no simple modeling of this behavior is applicable.[112] Thus, instead of using Coulomb's law we have to consider the Poisson-equation describing the decay of any potential. The one-dimensional approach having only the dimension D assuming infinitely expanded flat surfaces can be written as:

$$\varepsilon\varepsilon_0 \frac{\partial^2 \Psi(D)}{\partial D^2} = -\rho_{\mathrm{e}} \tag{3.3}$$

with ε_0 and ε being the vacuum permittivity and the permittivity of the continuous phase. ρ_{e} describes the local charge density of counterions. Boltzmann statistics apply for ρ_{e} and by assuming the presence of only monovalent ions we can write[111]

$$\rho_e = c_0 e \left[\exp\left(\frac{-e\Psi(D)}{k_B T}\right) - \exp\left(\frac{e\Psi(D)}{k_B T}\right)\right] \tag{3.4}$$

Here $e\Psi(D)$ accounts for the energy to bring a monovalent ion from infinity to distance D and c_0 is the concentration of the ions whereas e is the modulus of the electron charge and k_B the Boltzmann constant. Combining equations 3.3 with 3.4 and solving the obtained differential equation assuming the boundary conditions $\Psi(D=0) = \Psi_0$ and $\Psi(D \to \infty) = 0$ results in[111,112]

$$\Psi(D) = 64 c_0 k T \kappa^{-1} \tanh^2\left(\frac{e\Psi_0}{4k_B T}\right) \exp\left(-D\kappa\right). \tag{3.5}$$

which is known as the full one-dimensional solution of the Poisson-Boltzmann equation. Here $\lambda_D = \kappa^{-1}$ is called the Debye-length with

$$\lambda_D = \sqrt{\frac{\varepsilon\varepsilon_0 k_B T}{2 c_0 e^2}}. \tag{3.6}$$

The Debye length is the distance at which the surface potential Ψ_0 is decayed to $\Psi_0 \exp^{-1}$. In case of "low" potentials meaning $e\,|\Psi| << k_B T$ a sufficient simplification is the series expansion of equation 3.3 and neglection of all but the linear term. This results in $\Psi(D) = \Psi_0 \exp\left(-\kappa D\right)$.[111] The decay of the potential gets steeper inasmuch as the ion concentration is increased. This means the addition of salt to a colloidal dispersed system may lead to destabilization.

Combining the VdW attraction and the electrostatic repulsion potential of two infinitely expanded flat surfaces together results in what is typically called the DLVO-potential

$$U_{DLVO}(D) = 64 c_0 k T \kappa^{-1} \tanh^2\left(\frac{e\Psi_0}{4k_B T}\right) \exp\left(-D\kappa\right) - \frac{A_H}{12\pi D^2}. \tag{3.7}$$

named as that due to the scientists Derjaguin, Verwey, Landau and Overbeek who discovered it.[111,112,117] As already mentioned above the addition of salt tremendously influences the "shape" of the overall potential as depicted in figure 3.1. Salt ions shield the electrostatic repulsion potential. This means that a decrease of salt concentration results in less shielding and thus a higher contribution of the repulsion term in equation 3.7. At very close proximities however, the overall potential

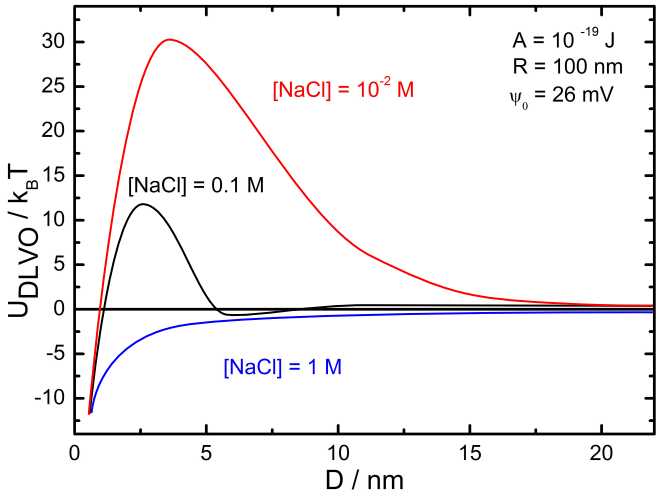

Figure 3.1: The DLVO-potential $U_{\mathrm{DLVO}}(D)$ in units of k_BT against the separation distance of two spherical objects D at different salt concentrations. [112]

gets negative which means aggregation will proceed. The importance therefore lies in the maximum of the potential. A $U_{\max} > 15k_{\mathrm{B}}T$ is considered as being stable.[107,108,111] Dispersions trapped in the second potential minimum as shown in figure 3.1 at a sodium chloride concentration of 0.1 M possess a relatively low barrier of re-dispersion. This phenomenon is called flocculation and is reversible.

Besides ionic surfactants for electrostatic stabilization on base of the DLVO-theory,[117] non-ionic surfactants, *e.g.* adsorbed or covalently attached polymers may stabilize sterically.[118,119] Considering the continuous phase to be a good solvent for the polymers covering the dispersed phase a full coverage will certainly lead to a elastic compression and thus repulsion of the colloids apart from each other while approaching. Inasmuch as the surface coverage allows a penetration of the polymers an increase of non-favorable polymer-polymer segment interaction is the result. This leads to a reduction of the entropy of mixing or, from another perspective, an increase of osmotic pressure and to an overall increase of the Gibbs free energy of the system.[111] This is unfavorable and pulls the colloids apart from each other. A poor solvent results in the opposite phenomenon. Polymer-solvent interactions are less favorable and thus aggregation of the colloids will proceed.[118]

3.2.3. Ostwald ripening

When emulsions and thus liquid-liquid dispersions are considered, so-called Ostwald ripening can lead to an increase of the size distribution of the dispersed droplet phase.[114] In the following description I will focus on oil in water emulsions. Smaller droplets possess a higher Laplace-pressure P_{Laplace} than bigger ones:[111]

$$P_{\text{Laplace}} = \frac{2\gamma_{\text{A}}}{R} \tag{3.8}$$

Here R is the radius of a spherical droplet. This however means that inasmuch as there is a remaining solubility of the dispersed droplet phase in the continuous phase, the Laplace pressure difference between different sized droplets will induce diffusion from the smaller droplets to the bigger ones which leads to an increase of their size-inhomogeneity (Fig. 3.2).[120,121]

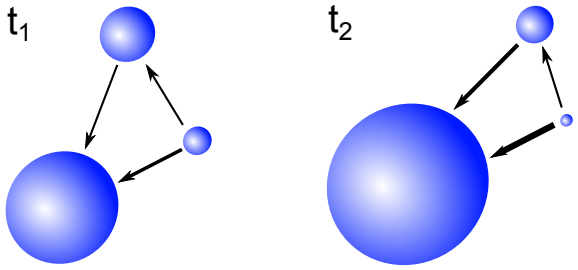

Figure 3.2: Different sized droplets possessing Laplace pressure differences between them. The arrow thicknesses emphasize the magnitude of the difference which develops further with increasing time ($t_2 > t_1$).

A way of circumventing this phenomenon is the utilization of a low molecular weight hydrophobic reagent.[122] It is assumed that the hydrophobic reagent is completely dissolved within the dispersed phase and thus after the emulsification step all the droplets, no matter which size, have the same concentration $c_{\text{h.r.}}$. Since the hydrophobic reagent cannot diffuse through the continuous phase, a diffusion of dispersed phase leads to the rise of osmotic pressure:

$$\Pi_{\text{Osmotic}} = \frac{RTc_{\text{h.r.}}}{M_{\text{h.r.}}} \tag{3.9}$$

opposing the Laplace pressure. Here $M_{\text{h.r.}}$ is the molecular weight of the hydrophobic reagent. Diffusion will only proceed until the raising osmotic pressure counterbal-

ances the Laplace pressure $P_{\text{Laplace}} = -\Pi_{\text{Osmotic}}$ which is schematically shown in figure 3.3.

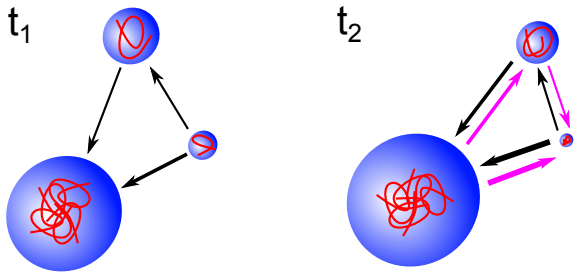

Figure 3.3: Different sized droplets with dissolved hydrophobic reagent. The Laplace pressure difference (black arrows) induces diffusion which leads to the rise of an opposing osmotic pressure difference (purple arrows) counterbalancing each other at a certain point.

3.2.4. Coalescence

In contrast to solid dispersed particles, droplets may deform easily. Considering emulsions, a notable phenomenon is the occurrence of coalescence which basically means the merging of two droplets to form a single daughter droplet.[111] The mechanism is depicted in figure 3.4. Coalescence is considered as one of the major reasons

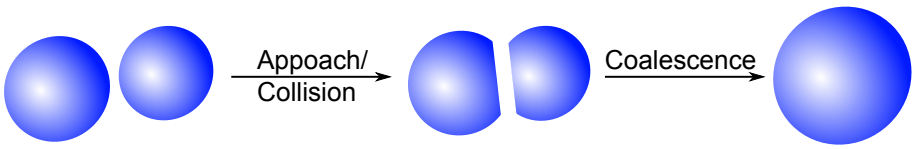

Figure 3.4: Coalescence is introduced by the approach and collision of droplets leading to their merging.

for the huge size distribution observed in nanoparticle dispersions obtained from the miniemulsion solvent evaporation process.[32] Studying this question was one of the major topics of my work and will be discussed in detail in the main part of my thesis.[24,34] However, considering the steps leading to coalescence first of all the electrostatic attraction between the droplets has to be circumvented by an appropriate electrostatic or steric stabilization as discussed above. Furthermore, the coverage of the emulsion droplets with surfactants was found to play a major role.[111,113,123]

3.3. Preparation of polymeric colloids

Polymeric colloids in the nm regime are fabricated from emulsion droplets as precursors. Primary dispersions are obtained from the polymerization of monomer within the droplets. For secondary dispersion, the polymerization is decoupled from the formulation into the colloidal form. In the following subsections I will discuss on these two approaches by means of specified examples.

3.3.1. Emulsion polymerization

In the classical emulsion polymerization, the monomer is dispersed via stirring in a continuous water phase forming a macroemulsion. One feature of macroemulsions is that a relatively high amount of surfactant is added for stabilization leading to droplet sizes between 0.1 μm up to 10 μm and typically a broad size distribution. Kinetically stabilized droplets still possess a thermodynamic driving force for aggregation.[108]

A schematic of the mechanism of emulsion polymerization is depicted in figure 3.5.[124] The monomer is dispersed into droplets and stabilized by surfactants possessing a low but crucial solubility in the water phase. Since the surfactant concentration is above the critical micelle concentration (CMC), micelles assemble having a hydrophobic interior. A water soluble initiator, *e.g.* potassium persulfate $K_2S_2O_8$, initiates polymerization in the water phase. The proceeding addition of monomer to the growing chains increases their hydrophobicity leading to the diffusion of the oligoradicals to the micelles or accumulation of surfactants around them. The monomer droplets act as a reservoir of monomer providing constant diffusion of monomer to the micelles where polymerization proceeds. Polymerization inside the droplets is usually negligible since $\approx 10^{21}$ micelles per liter oppose $\approx 10^{13}$ droplets per liter resulting in orders of magnitude higher surface area of the micelles. The process finishes when all monomer has reacted and the supply of monomer from the droplets vanishes. Final particle size between 0.05 μm up to 5 μm might be achieved.[125,126]

In contrast, if a very high amount of surfactant is used for stabilization, a thermodynamically stable emulsion may form with droplet sizes between 5 nm and 100 nm. High surfactant concentration in this respect typically means 50 - 200 % of

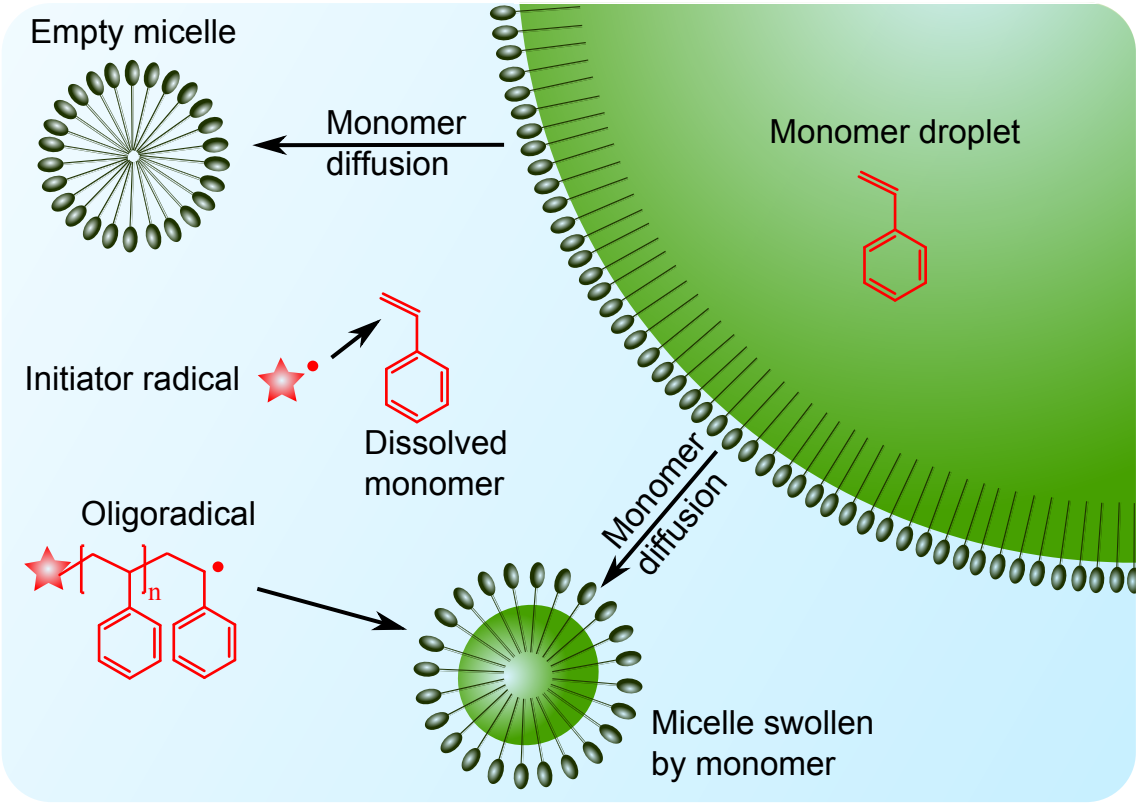

Figure 3.5: Schematic of the mechanism of emulsion polymerization on th example of polystyrene.

the relative weight amount of the dispersed phase. Such types of emulsions are called microemulsions. The polymerization mechanism is similar to the classical or macroemulsion polymerization whereas nanoparticle sizes between 5 nm to 50 nm are obtained.[108,127,128]

3.3.2. Miniemulsion polymerization

Another type of emulsion is named miniemulsion. In comparison to microemulsions the surfactant concentration is low, typically ranging from 0.1 wt% to 20 wt%.[120,129] The surfactant does not fully cover the surface of the dispersed phase. Thus, the typical droplet sizes of miniemulsions between 50 - 500 nm can only be achieved when high shear forces, *e.g.* due to ultrasonication, are applied.[130]

Figure 3.6 highlights the mechanism of miniemulsion polymerization. The difference to emulsion polymerization is the solubility of the initiator in the monomer.

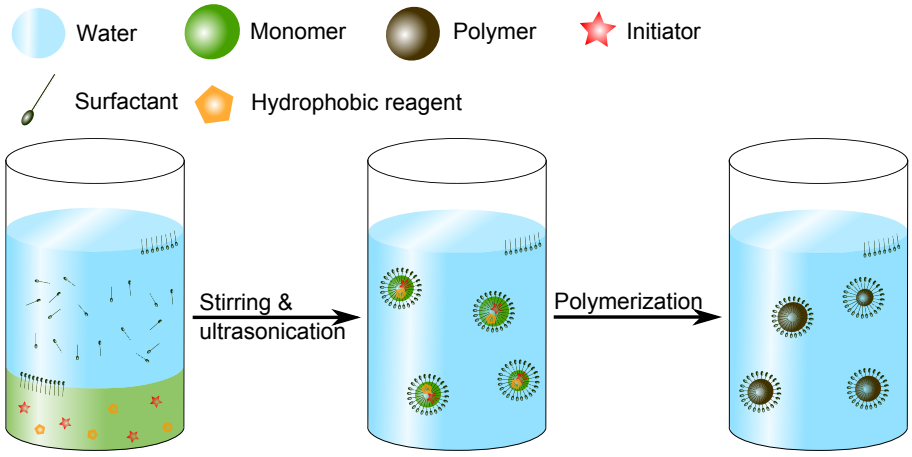

Figure 3.6: The process of miniemulsion polymerization.

Ultrasonication is applied to yield small droplets of monomer covered with surfactant. Upon initiation of the polymerization by *e.g.* increased temperature, every droplet can be regarded as a single independent "nano-reactor".[131,132] Diffusion of monomer may occur between the droplets but shall be suppressed by the addition of a hydrophobic reagent to prevent Ostwald ripening (Figure 3.3).[122] The process is finished in every droplet individually inasmuch as all monomers have reacted or no radicals are left.

3.3.3. The solvent evaporation process from miniemulsion droplets

The solvent evaporation process from miniemulsion droplets (SEED) as templates was first reported in 1977.[22] The procedure was further developed and patented[23] whereas nowadays it is well established in pharmaceutical science for drug encapsulation in biodegradable polymers.[30,31] The major advantage is the possibility of combination of materials and doping of the final nanoparticles, *e.g.* the fabrication of nanoparticles with magnetic properties by adding magnetic nanoparticles.[28,29]

The SEED process is depicted in figure 3.7. A pre-synthesized polymer is dissolved in a good solvent, *e.g.* polystyrene in toluene, surfactant is added and due to stirring and ultrasonication, miniemulsion droplets are obtained comprising the dissolved polymer. The organic solvent evaporates while heating or just over time since its low solubility facilitates diffusion to the water-air interface. Thus, the solubility

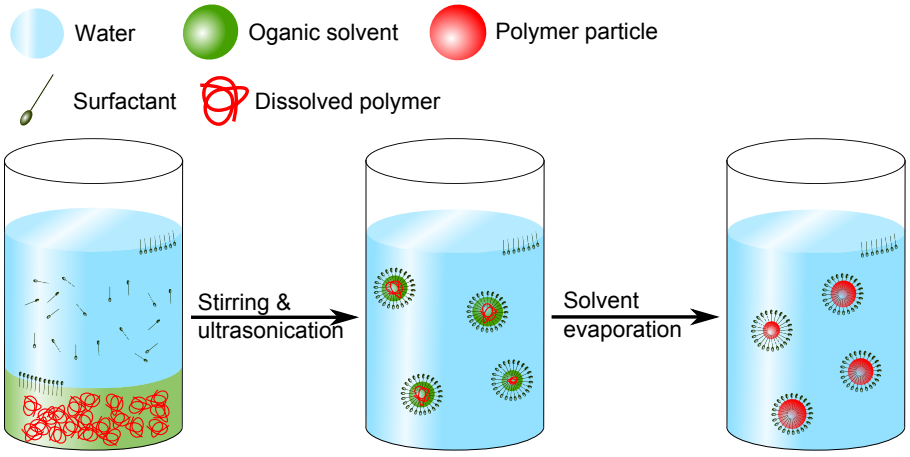

Figure 3.7: The solvent evaporation process from miniemulsion droplets.

of solvent in the continuous phase[133] as well as the ambient pressure strongly influences the evaporation which usually takes hours.[32] What remains are polymeric nanoparticles typically possessing sizes between 50 nm and 500 nm. For controlling size and size distribution of the particles surfactant concentration,[25] intensity and duration of ultrasonication[134] as well as the nature of solvent and viscosity of the polymer solution are important.[135]

3.4. Self-assembly of amphiphilic copolymers

The phenomenon of self-assembly of amphiphilic molecules will be discussed and the driving forces highlighted. A brief thermodynamic view on micellization and the *CMC* is given. Characteristics of assemblies of amphiphilic copolymers in aqueous media are discussed. Moreover the dynamic equilibrium of micellar structures is described.

3.4.1. Fundamentals of micellization

Micelles are aggregates of typically 50 to 1000 amphiphilic molecules which tend to self-assemble above a certain concentration, the *CMC*.[111] Size and shape of the assemblies are governed by energetic and geometric means of the single molecules. In the description given here I consider the formation of micelles in water. The clustering of the hydrophobic chains of the amphiphilic molecules results in the exclusion

of the aqueous phase and thus a minimization of the alkyl-water contacts. Additionally, the alignment of the hydrophilic part of the molecules to the surrounding water is achieved.[107] Figure 3.8 shows a two-dimensional scheme of the formation of micelles from amphiphilic block copolymers.

From the thermodynamic point of view, micelle formation in aqueous media is an entropically driven process.[136,137] This is controversial for the first moment, since the formation of ordered structures will always result in a decrease of entropy which is thermodynamically non-favorable. However, inasmuch as free hydrophobic chains of the amphiphilic molecules are in contact with water, the formation of solvation shells will proceed (see also figure 3.8). Water is not able to form hydrogen bonds with the hydrophobic chains which will result in a more ordered structure of the surrounding water due to the formation of more hydrogen bonds between the water molecules. The degrees of freedom of the water molecules are reduced. This results in the decrease of entropy which is overcome with the release of the hydrogen bond enthalpy.[111,136] At the *CMC*, this enthalpy release is not sufficient which leads to the exclusion of hydrophobic parts from the water by formation of micellar structures accompanied by the collapse of the solvation shells which finally results in an increase of entropy. Note that in contrast to the formation of micellar structures in aqueous

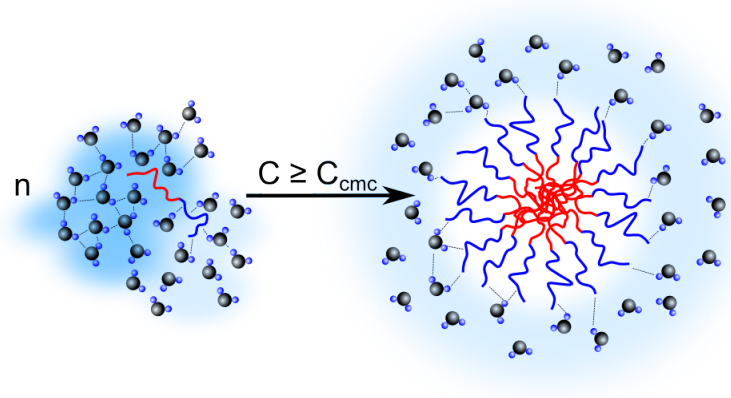

Figure 3.8: The assembly of block copolymers comprising a hydrophilic (blue) and a hydrophobic (red) block to micellar structures in aqueous media. Dotted lines highlight hydrophobic bonding which is more pronounced between the water molecules surrounding the hydrophobic block of the single chains. This results in a more ordered water structure (Degree of order scales with intensity of the bluish background).

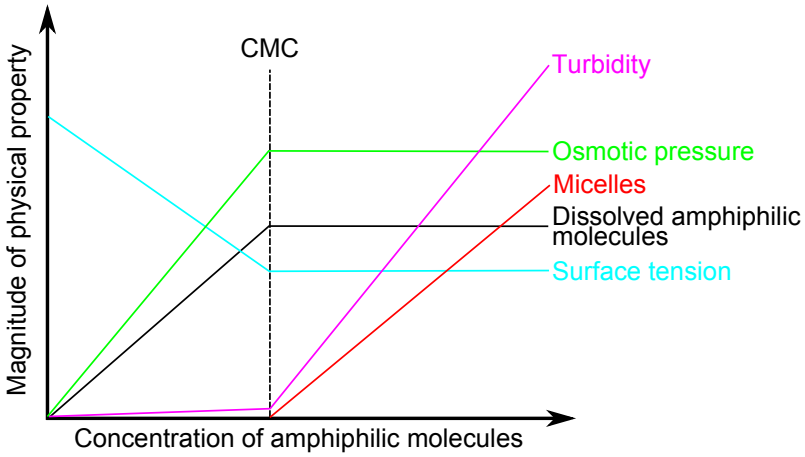

Figure 3.9: The amphiphilic molecule concentration dependency of some physical properties.

media, micelle formation in organic solvents is driven by enthalpic means, specifically by the increase of polymer/polymer segment interactions of the micelle core.[137]

Related to the formation of the micellar structures is the abrupt change of some physical properties of the micellar solution. This behavior is qualitatively depicted in figure 3.9.[107]

3.4.2. Thermodynamics of micellization

One way to approach the thermodynamics of micellization is to regard the micelle formation a kind of phase separation.[111,138] We can consider the chemical potential of the dissolved amphiphilic molecule μ_1 and compare with the chemical potential of the same molecule in a self-assembled structure μ_n. The chemical potential however is the sum of the effective standard chemical potential, μ_1° and μ_n° respectively, and the interactions with other molecules resulting in:[136,138]

$$\mu_1 = \mu_1^{\circ} + kT\ln(X_1) \tag{3.10a}$$

$$\mu_n = \mu_{\mathrm{n}}^{\circ} + \frac{kT}{n}\ln\left(\frac{X_n}{n}\right). \tag{3.10b}$$

Here, X_1 and X_n are the concentrations of dissolved amphiphilic molecules and micellar structures formed by n molecules, respectively (see also figure 3.8). Equi-

librium thermodynamic insists that when assemblies of a species form, the chemical potential μ of identical molecules in different assemblies are the same.[72] Thus, we can write:

$$\mu_n^{\circ} - \mu_1^{\circ} = kT \left[\ln (X_1) - \frac{1}{n} \ln \left(\frac{X_n}{n} \right) \right] \tag{3.11}$$

and at the CMC ($X_1 = CMC$) the second addend of equation 3.11 is negligible resulting in:[107]

$$CMC \approx \exp \left(\frac{\mu_n^{\circ} - \mu_1^{\circ}}{kT} \right). \tag{3.12}$$

The aforementioned equations only apply in the case of non-ionic amphiphilic molecules. When ionic molecules are considered, an additional dependence on the net charge and in particular on the presence and association of counterions on the CMC becomes important.[139,140] Typically, electrostatic repulsion between ionic hydrophilic parts leads to comparably higher CMC's then observed for similar non-ionic amphiphilic molecules.[141,142] However, the screening of electrostatic interactions by adding salt to the system has a drastic effect resulting in decrease of the CMC.[111,143]

3.4.3. Scaling concepts of amphiphilic block copolymer micelles

A wide variety of different block copolymer micelle architectures exist and have been experimentally investigated, *e.g.* spherical micelles[144,145], rod-like micelles[146] and bilayer vesicles.[147] However, in contrast to surfactant micelles, for micellar structures formed by amphiphilic block copolymers, no simple predictions of the shape on base of geometric means are possible. In polymer physics, scaling concepts are the typical way to approach behavior and conformation of single chains and their assemblies. Here I will give a brief introduction into the scaling theory of the assembly of AB block copolymers in selective solvent. Figure 3.10 shows the two limiting diblock copolymer micelle types, namely "star-shaped" micelles having a comparably big corona and "crew-cut" micelles comprising a short corona.[148]

A typical way to approach the problem is a Helmholtz free energy analysis, whereas the Helmholtz free energy F considers the energy of a system which is available to perform work by means of thermodynamics (first-law of thermodynamics: pdV).[72] From know on I consider a single diblock copolymer chain in a spherical micelle provided that the Helmholtz free energy of the system is almost solely gov-

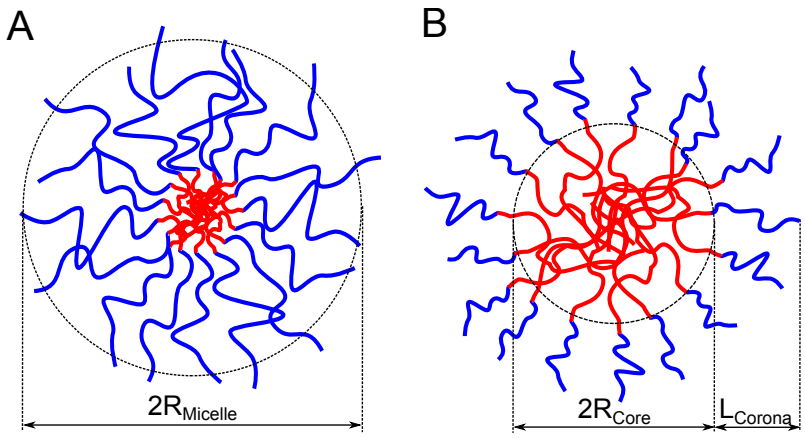

Figure 3.10: The two limiting cases of AB block copolymer micelles. "Starlike" or "hairy" micelles having a comparably thick corona (A) and "crew-cut" micelles comprising a thin corona (B). Parameters characterizing the micelles morphology are delineated.

erned by the Helmholtz free energy of the micelles. This is a good approximation if the system is well above the CMC but below a concentration where micelles would interact with each other.[149] Thus, the Helmholtz free energy of a single chain in a micelle F_{Mic} is the sum of the Helmholtz free energy of the core F_{Core}, corona F_{Corona}, and the interface at the insoluble core block F_{Int}:[37]

$$F_{\mathrm{Mic}} = F_{\mathrm{Int}} + F_{\mathrm{Core}} + F_{\mathrm{Corona}} \tag{3.13}$$

The volume of the micelle core is approximated as

$$V_{\mathrm{Core}} \approx b^3 N_{\mathrm{Core}} f \approx R_{\mathrm{Core}}^3. \tag{3.14}$$

Here, f is the micelle aggregation number, thus the number of polymer chains the micelle is build of and b is the monomer length which is assumed to be similar for core and corona block respectively.[149] The latter equation leads to the Helmholtz free energy of the core interface F_{Int}:

$$F_{\mathrm{Int}} \approx \frac{\gamma R_{\mathrm{Core}}^2}{f} \approx \gamma f^{-1/3} N_{\mathrm{Core}}^{2/3} b^2 \tag{3.15}$$

Since the Helmholtz free energy of a single chain is considered, I divide through f.[37] In this analysis, γ can be taken as the interfacial tension between core form-

ing polymer and solvent due to comparably small interactions between core and corona.[148,150]

The next step is the derivation of the Helmholtz free energy of the core F_{Core}. Above the glass transition it is appropriate to consider the micelle core as a polymer melt. Thus, F_{Core} is determined by the change of configurational entropy of the single chains.[20] The chains are assumed to be stretched over their end-to-end distance vector $\vec{r}$ which is then R_{Core}. This assumption is reasonable since confinement and fixation of one end of the chains on the core-corona interface reduce the configurational entropy. However, it may lead to an overestimation of F_{Core}.[149] Considering Gaussian behavior of a single chain the probability of having an end-to-end distance vector R of the chain is

$$P(N,R) = \left(\frac{3}{2\pi N b^2}\right) \exp\left(-\frac{3R^2}{2Nb^2}\right). \tag{3.16}$$

Thus, the configurational entropy $S(N,R) = k_{\mathrm{B}}\ln\Omega(N,R) = k_{\mathrm{B}}\ln P(N,R)$ and the Helmholtz free energy of the micelle core are determined as:[37,149]

$$S(N,R) = -\frac{3}{2}k_{\mathrm{B}}\frac{R^2}{Nb^2} + S_{\mathrm{o}} \tag{3.17a}$$

$$F(N,R) = \frac{3}{2}k_{\mathrm{B}}T\frac{R^2}{Nb^2} + F_{\mathrm{o}} \tag{3.17b}$$

giving the scaling behavior of the Helmholtz free energy of the core F_{Core} normalized by $k_{\mathrm{B}}T$:[37]

$$\frac{F_{\mathrm{Core}}}{k_{\mathrm{B}}T} \approx \frac{R_{\mathrm{Core}}^2}{N_{\mathrm{Core}}b^2} \approx f^{2/3}N_{\mathrm{Core}}^{-1/3}. \tag{3.18}$$

The most elaborate part in modeling the scaling behavior of F_{Mic} is accounting for the Helmholtz free energy of a single polymer chain within the micelle corona F_{Corona}. For the following consideration I introduce the concept of polymer blobs. If the chain conformation is perturbed, *e.g.* due to interactions or applied external forces within a blob ξ, a part of the polymer chain, the configurational statistics obey Gaussian behavior.[20] Introducing here the polymer brush model of Alexander[151] and de Gennes[152] the dissolved coronal chains are considered as being grafted on the micelle core. Due to the spherical geometry of the core the volume fraction of the corona polymer ϕ_{Corona} reduces with distance r from the core and so do the

perturbations. Thus the blob size increases with r resulting in $\xi = \xi(r)$ which is schematically shown in figure 3.11.[153] The blob size therefore can be written as

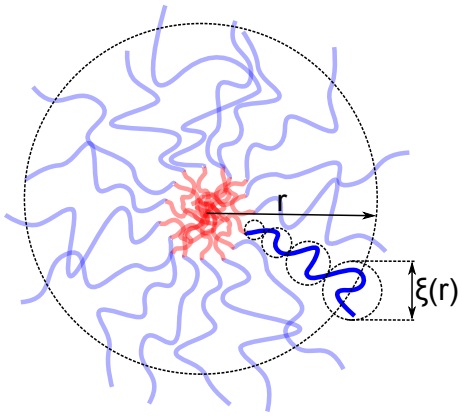

Figure 3.11: A micelle comprising a corona blob size dependency $\xi(r)$ on the distance from its center r.

$\xi(r) = bn(r)^{\nu}$ with ν being the Flory-exponent and $n(r)$ as the number of monomers per blob $\xi(r)$.[149] From here on ν is set to 3/5 to account for excluded volume effects of coronal chains.[20] The spherical shell of thickness $\xi(r)$ approximately possesses the volume $r^2\xi(r)$ which is similar to the volume occupied by all the blobs within this shell $f\xi(r)^3$ which provides $\xi(r) \approx rf^{-1/2}$.[149] This relationship allows the expression of the coronal volume fraction $\phi_{\text{Corona}}(r)$ without blob size parameters:

$$\phi_{\text{Corona}}(r) \approx \frac{n(r)b^3}{\xi(r)^3} \approx f^{2/3}\left(\frac{b}{r}\right)^{4/3} \tag{3.19}$$

Now, $\phi_{\text{Corona}}(r)$ is integrated over the corona thickness $L = L_{\text{Corona}}$ to yield the volume of the corona V_{Corona}

$$V_{\text{Corona}} \approx fN_{\text{Corona}}b^3 \approx \int_{R_{\text{Core}}}^{R_{\text{Core}}+L} \phi_{\text{Corona}}(r)dr^3 \tag{3.20}$$

whereas under the assumption that $L \gg R_{\text{Core}}$ this results in:[37,137,149]

$$L \approx f^{1/5}N_{Corona}^{3/5}b. \tag{3.21}$$

A similar way is chosen to access the Helmholtz free energy of the corona per chain.

Integration over the energy density per blob $k_BT/\xi(r)^3$ yields:[149]

$$\frac{F_{\text{Corona}}}{k_BT} \approx \frac{1}{f}\int_{R_{\text{Core}}}^{R_{\text{Core}}+L} \frac{r^2}{\xi(r)^3}dr \approx f^{1/2}\ln\left(1+\frac{L}{R_{\text{Core}}}\right). \tag{3.22}$$

Now I come back to equation 3.13. For both types of micelles further simplifications can be made. "Star-shaped" micelles comprise an extended corona ($N_{\text{Corona}} \gg N_{\text{Core}}$) providing $F_{\text{Corona}} \gg F_{\text{Core}}$ which makes F_{Core} negligible. The reverse assumptions can be made for "crew-cut" micelles ($N_{\text{Core}} \gg N_{\text{Corona}}$) giving $F_{\text{Core}} \gg F_{\text{Corona}}$.[37] Furthermore, the logarithmic factor in equation 3.22 can be taken as a constant C which results in the Helmholtz free energy per chain in the micelle:[37,149]

$$\frac{F_{\text{Mic}}}{k_BT} \approx \begin{cases} \dfrac{\gamma b^2}{k_BT} f^{-1/3} N_{\text{Core}}^{2/3} + f^{1/2} + C & N_{\text{Corona}} \gg N_{\text{Core}} \\ \dfrac{\gamma b^2}{k_BT} f^{-1/3} N_{\text{Core}}^{2/3} + f^{2/3} N_{\text{Core}}^{-1/3} & N_{\text{Corona}} \ll N_{\text{Core}} \end{cases} \tag{3.23}$$

To find the mean aggregation number $\langle f \rangle$, F_{Mic}/k_BT is minimized in terms of f

$$0 = \frac{\partial}{\partial f}\left(\frac{F_{\text{Mic}}}{k_BT}\right) \approx \begin{cases} -\dfrac{\gamma b^2}{k_BT} f^{-4/3} N_{\text{Core}}^{2/3} + f^{-1/2} & N_{\text{Corona}} \gg N_{\text{Core}} \\ -\dfrac{\gamma b^2}{k_BT} f^{-4/3} N_{\text{Core}}^{2/3} + f^{-1/3} N_{\text{Core}}^{-1/3} & N_{\text{Corona}} \ll N_{\text{Core}} \end{cases} \tag{3.24}$$

resulting in the scaling behavior:[37]

$$\langle f \rangle \sim \begin{cases} N_{\text{Core}}^{4/5} & N_{\text{Corona}} \gg N_{\text{Core}} \\ N_{\text{Core}} & N_{\text{Corona}} \ll N_{\text{Core}} \end{cases} \tag{3.25}$$

Note that I omit all the pre-factors as this is usual in scaling analysis.[37,137,148–155] Moreover, having equation 3.14 in hands, $\langle R_{\text{Core}} \rangle$ reads

$$\langle R_{\text{Core}} \rangle \sim \begin{cases} N_{\text{Core}}^{3/5} b & N_{\text{Corona}} \gg N_{\text{Core}} \\ N_{\text{Core}}^{2/3} b & N_{\text{Corona}} \ll N_{\text{Core}} \end{cases} \tag{3.26}$$

and the mean micelle radius $\langle R_{\text{Mic}} \rangle$:

$$\langle R_{\text{Mic}} \rangle \sim \begin{cases} \langle L \rangle \sim N_{\text{Core}}^{4/25} N_{\text{Corona}}^{2/5} b & N_{\text{Corona}} \gg N_{\text{Core}} \\ \langle R_{\text{Core}} \rangle \sim N_{\text{Core}}^{2/3} b & N_{\text{Corona}} \ll N_{\text{Core}} \end{cases} \tag{3.27}$$

in limits of "star-shaped" and "crew-cut" micelles, respectively. When Gaussian fluctuations around the mean aggregation number $\langle f \rangle$ are assumed, the corresponding standard deviation σ_f may be approximated as:[37,155]

$$\sigma_f \approx \left(\langle f \rangle \frac{\partial^2}{\partial f^2} \left(\frac{F_{\mathrm{Mic}}}{k_{\mathrm{B}}T} \right) (\langle f \rangle) \right)^{-1/2} \sim \begin{cases} N_{\mathrm{Core}}^{1/5} & N_{\mathrm{Corona}} \gg N_{\mathrm{Core}} \\ N_{\mathrm{Core}}^{1/3} & N_{\mathrm{Corona}} \ll N_{\mathrm{Core}} \end{cases} \tag{3.28}$$

3.4.4. The dynamic equilibrium of micellar structures

The equilibrium behavior of small molecule micellar structures was first theoretically described in the 1970's by Aniansson and Wall.[36,156,157] They proposed two mechanisms. First, small deviations from the equilibrium state lead to insertion and expulsion of single molecules or unimers not changing the overall number of micelles:[38]

$$A_{f-1} + A_1 \rightleftharpoons A_f \tag{3.29}$$

where A_i considers an "aggregate" with aggregation number i. The second process describes an association/dissociation equilibrium of micelles and therefore considers also their fusion and fission since the total number of micelles changes.[38] However, as stated by Halperin and Alexander[37] who first extended the Aniansson and Wall theory on block copolymers, the relaxation time associated with micelle fusion/fission may be orders of magnitude larger than τ_{Uni}. Thus the slow exchange, especially with respect to the work presented within my thesis, only plays a minor role. In particular, even if significant micelle fusion and fission is present, unimer exchange will be the dominating process responsible for the exchange of the molecules between micelles as shown by dissipative particle dynamics simulations performed by Li and Dormidontova.[158] Therefore, I focus on a brief description of the theory of unimer exchange between diblock copolymer micelles. A complete derivation of the scaling analysis lies beyond the scope of my thesis and is described in detail elsewhere.[36–38,149,156,157,159]

Regarding equation 3.29 unimer exchange may be expressed as a first order chemical rate equation. Thus, if at $t \to 0$ the exchange is assumed to start, the time correlation function $K(t)$ can be understood as sort of normalized concentration

with $K(t=0) = K_0 = 1$ possessing a rate constant k leading to:[72]

$$\frac{dK}{dt} = -kK \quad \Longrightarrow \quad \int_{K_0}^{K(t)} \frac{dK}{K} = -\int_0^t k dt \quad \Longrightarrow \quad K(t) = \exp\left(-kt\right). \tag{3.30}$$

The unimer exchange, in particular the expulsion of an insoluble block, can be modeled in the framework of Kramers theory.[160] A melt-like micelle core is considered as a source of polymers within a potential well. Along the reaction coordinate, the expulsion and thus outflow is modeled with the stationary one-dimensional Smulochowski equation.[37] Since the outflow from the rim of the well includes the crossing of a potential barrier U, Boltzmann statistics apply. Thus, the rate constant can be expressed as:[37,38]

$$k \approx \frac{1}{\tau_{\mathrm{Uni}}} = \frac{1}{\tau_0} \exp\left(-U\right). \tag{3.31}$$

U therein is mainly determined by the creation of new interfacial area between solvent and core forming polymer γ.[38] When V_{m} is the molar volume of the polymer within the core, U might be written as:[37,38]

$$U = A \frac{\gamma V_{\mathrm{m}}^{2/3} N_{\mathrm{Core}}^{\beta}}{k_{\mathrm{B}} T}. \tag{3.32}$$

Here A and β take into account the conformation of the core block during expulsion. The two border cases of core polymer conformation during expulsion can be a spherical shape or a stretched conformation.[44,161]

$$A = \begin{cases} (36\pi)^{1/3} \\ (8\pi)^{1/3} \end{cases} \qquad \beta = \begin{cases} 2/3 & \text{Spherical} \\ 1 & \text{Stretched} \end{cases} \tag{3.33}$$

The last missing parameter is the relaxation time τ_0. Different scaling approaches have been proposed.[37,38] I follow Bates, Lodge and coworkers and describe the dynamics inside the micelle core in frame of Rouse dynamics.[45] The Rouse model describes a polymer chain by means of N beads connected by springs possessing a root mean square distance of a polymer segment b.[20,162] Each bead comprises a friction coefficient ζ. Thus, in terms of the Einstein relation the diffusion coefficient $D = k_{\mathrm{B}}T/(N\zeta)$ and under assumption of an ideal Gaussian chain $\langle \vec{r}^2 \rangle = Nb^2$

without excluded volume:[20]

$$\tau_{\mathrm{R}} \approx \frac{\langle \vec{r}^2 \rangle}{D} \approx \frac{\zeta}{k_{\mathrm{B}}T} N \langle \vec{r}^2 \rangle \approx \frac{\zeta b^2 N^2}{k_{\mathrm{B}}T} \tag{3.34}$$

may be written. Hence, the Rouse time τ_{R} is a characteristic time a polymer needs to diffuse approximately the distance of his root mean square end-to-end distance vector $\sqrt{\langle \vec{r}^2 \rangle}$. In framework of the problem of dynamic equilibrium exchange between micelles for τ_0 the exact solution of the highest Rouse time is given as:[162]

$$\tau_0 = \tau_{\mathrm{R}} = \frac{\zeta b^2 N_{\mathrm{Core}}^2}{6\pi^2 k_{\mathrm{B}}T}. \tag{3.35}$$

Putting equations 3.30 - 3.35 together the time correlation function reads:

$$K(t, N_{\mathrm{Core}}) = \exp\left[-t \frac{6\pi^2 k_{\mathrm{B}}T}{\zeta b^2 N_{\mathrm{Core}}^2} \exp\left(\frac{-A\gamma V_{\mathrm{m}}^{2/3} N_{\mathrm{Core}}^{\beta}}{k_{\mathrm{B}}T}\right)\right] \tag{3.36}$$

As the double exponential dependency of $K(t)$ on N_{Core} suggests there exists a tremendous influence of the exchange process on degree of polymerization of the core block. Moreover, its polydispersity may significantly broaden the relaxation kinetics. This phenomenon was first taken into account by Lodge, Bates and coworkers.[45] They suggested an integration over a distribution function describing the size polydispersity of the core forming polymer. In particular they found a Schulz-Zimm distribution to fit the situation appropriate:

$$P(N_{\mathrm{Core}}) = \frac{\xi^{\xi+1}}{\Gamma(\xi+1)} \frac{N_{\mathrm{Core}}^{\xi-1}}{\langle N_{\mathrm{Core}} \rangle^{\xi}} \exp\left(\frac{-\xi N_{\mathrm{Core}}}{\langle N_{\mathrm{Core}} \rangle}.\right) \tag{3.37}$$

Here $\xi = 1/(PDI - 1)$ and PDI is the polydispersity index.[45] This finally leads to a time correlation function reading:

$$R(t, N_{\mathrm{Core}}) = \int_1^{\infty} K(t, N_{\mathrm{Core}}) P(N_{\mathrm{Core}}) dN_{\mathrm{Core}}. \tag{3.38}$$

Part II.

Kinetic processes in polymer based colloidal systems

4. FCS directly monitors coalescence during nanoparticle preparation

Dual color fluorescence cross-correlation spectroscopy (DC FCCS) experiments were conducted to study the coalescence and aggregation during the formation of nanoparticles. To assess the generality of the method, three completely different processes were selected to prepare the nanoparticles. Polymeric nanoparticles were formed either by solvent evaporation from emulsion nanodroplets of polymer solutions or by miniemulsion polymerization. Inorganic nanocapsules were formed by polycondensation of alkoxysilanes at the interface of nanodroplets.

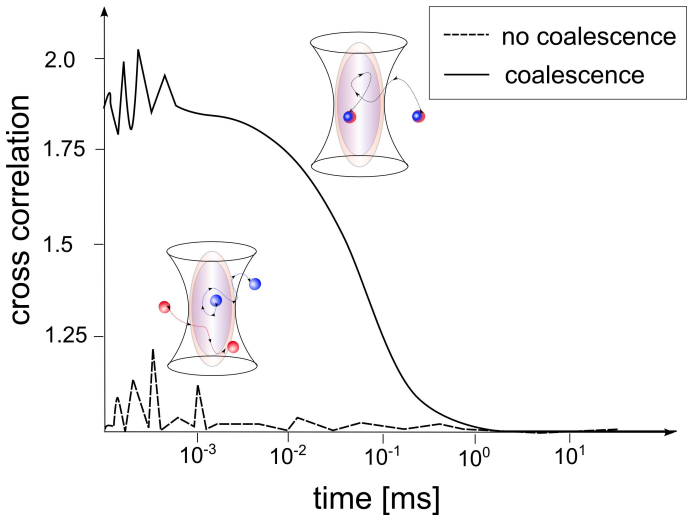

In all cases, DC FCCS provided fast and unambiguous information about the occurrence of coalescence and thus a deeper insight into the mechanism of nanoparticle formation. In particular, it was found that coalescence played a minor role for the emulsion solvent evaporation process and the miniemulsion polymerization, whereas substantial coalescence was detected during the formation of the inorganic nanocapsules. These findings demonstrate that DC FCCS is a powerful tool for monitoring nanoparticles genesis.

Reproduced with permission from:
D. Schaeffel, R. H. Staff, , H.-J. Butt, K. Landfester, D. Crespy, K. Koynov: Fluorescence Correlation Spectroscopy directly monitors coalescence during nanoparticles preparation, *Nano Lett.*, **2012**, *12*(11), 6012-6017.

4.1. Introduction

Synthesis and characterization of nanoparticles play a large role in current materials science with major foci on applications directed on therapeutics[163–165] and energy conversion and storage.[166] For the preparation of nanoparticles, micelles and emulsion droplets are often used as templates for polymerization processes[167] such as conventional emulsion[168] and miniemulsion polymerization[132] or inorganic reactions.[169,170] Emulsified solutions of polymers can be also advantageously used for the formation of polymer nanoparticles[25,26,171,172] and nanocapsules[173] after solvent evaporation from the emulsion droplets (SEED). However, the use of emulsion droplets as templates in chemical or physical processes for the formation of nanoparticles has intrinsic drawbacks originating from the colloidal stability of the emulsions. Indeed, coalescence between droplets and Ostwald ripening of the emulsions are mainly responsible for the nonuniformity of the obtained nanoparticles. In situ quantitative monitoring of coalescence is still a challenge in colloid science. Typically, dynamic light scattering is used to measure the size of droplets and nanoparticles at different stages of the preparation process to retrieve information on coalescence. However, this information is often incomplete or questionable because some phenomena with opposite effects on droplets or particle sizes cannot be easily decoupled. For instance, in the SEED process, the solvent evaporation leads to a shrinking of the droplet size whereas it is simultaneously increased by coalescence between droplets. Thus, new characterization methods that can provide direct information about the extent of coalescence during the preparation of nanoparticles are needed. Fluorescence correlation spectroscopy (FCS) is a powerful technique for studying the dynamics of fluorescent species such as small molecules, macromolecules, or nanoparticles in various environments.[64,174,175] The fluorescent intensity fluctuations caused by the diffusion of the species through a very small ($< f\mathrm{L}$) confocal detection vol-

ume are recorded and analyzed to obtain their diffusion coefficients, hydrodynamic radii, and concentrations.[64] Although initially developed and still predominantly used as a tool in molecular and cell biology,[73,77,176,177] FCS has also found many applications in polymer and colloid science in recent years. In particular, surface diffusion of adsorbed polymers,[178–182] or tracer diffusion in undiluted polymer solutions,[183–188] cross-linked networks,[189–192] and bulk polymers,[193] were studied. The formation of amphiphilic copolymer micelles and vesicles and their interaction with small molecules or nanoparticles was investigated.[13,15,17,147] Furthermore, very recently FCS was successfully applied to measure the size and polydispersity of microemulsion droplets.[47] Herein, we show for the first time how an extension of the classical FCS called dual color fluorescence cross-correlation spectroscopy (DC FCCS)[21,194] can be efficiently used to monitor directly the coalescence and aggregation during nanoparticles preparation from emulsions. We illustrate our general approach on three different but typical nanoparticle preparation methods: the solvent evaporation process from emulsion droplets (SEED), miniemulsion polymerization, and the interfacial polycondensation of alkoxysilanes with emulsion droplets as templates. The latter case allows the fabrication of silica nanocapsules, while polymer nanoparticles are obtained with the two other processes. Representative SEM and TEM micrographs of the three different types of particles are shown in Figure 4.7 of the Supporting Information (SI).

4.2. Experimental section

4.2.1. Synthetic approach

Our strategy is schematically presented in Figure 4.1 with the preparation of polystyrene (PS) nanoparticles by SEED taken as example. The first step is to synthesize two fluorescently labeled polymers with molecular weights similar to the unlabeled ones usually used to prepare the nanoparticles. To that end polymerizable BODIPY "blue" and "red" dyes suitable for FCS experiments were copolymerized with styrene and purified (see SI). Two solutions of labeled polystyrene in chloroform were prepared in two different beakers. Each of the colored polymer solutions was then separately mixed with aqueous solutions of SDS surfactant and sonicated to produce two different emulsions with either "blue" and "red" polymer/ chloroform

droplets in water. Finally the two emulsions were mixed and stirred following the usual SEED preparation procedure until complete evaporation of the chloroform and the formation of stable PS nanoparticles.

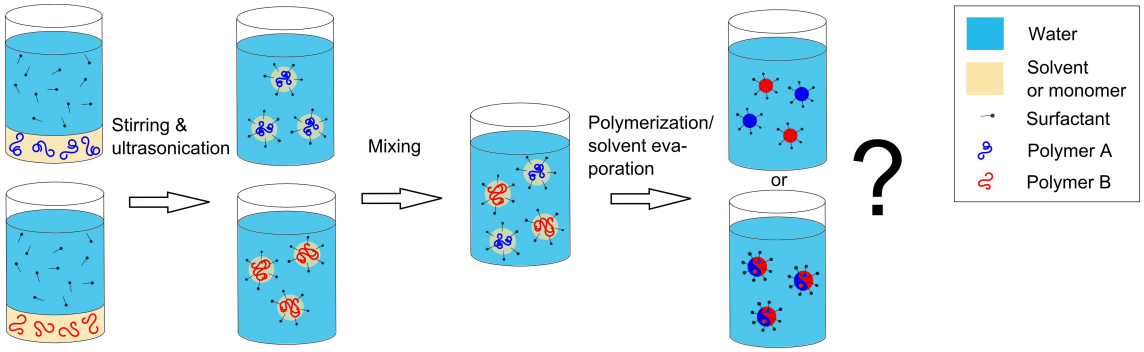

Figure 4.1: Concept of the experiment: two differently fluorescently labeled polymers are dissolved in an organic solvent or monomer and dispersed via stirring and ultrasonication prior to mixing. Polymerization or solvent evaporation leads to the formation of dispersed stable nanoparticles.

The occurrence of coalescence has then a dramatic effect on the labeling of the nanoparticles. Indeed, if coalescence has taken place to a large extent during the evaporation, the final dispersion should be double-colored. On the contrary, the final dispersion should be composed of a mixture of separated "blue" and "red" PS nanoparticles if no or insignificant coalescence has taken place.

4.2.2. Dual color Fluorescence Cross Correlation Spectroscopy

The presence of double-colored nanoparticles in the final dispersion was quantified by dual color fluorescence cross-correlation spectroscopy, an extension of the classical FCS method that is often used in molecular biology for example, for studying DNA hybridization and enzyme kinetics.[21,194] A schematic of the DC FCCS setup is shown in Figure 4.2a.

Two light beams from two lasers operating at different wavelengths, called "blue" and "red" for simplicity, are expanded, made collinear, and focused to a diffraction limited spots into the dispersion of nanoparticles by achromatic microscope objective with high numerical aperture. The created fluorescence light is collected by the same objective and delivered to two single photon counting avalanche photo detectors

(APD) after passing a confocal pinhole, dichroic mirrors, and emission filters. In this way, two subfemtoliter observation volumes V_{b} and V_{r} are created. For an optimal experimental arrangement they are perfectly overlapping in space (which was proved to be the case for our setup), creating an efficient common observation volume V_{br}. When two types of fluorescent species excitable by the "blue" and the "red" laser are independently diffusing through the common observation volume V_{br}, the corresponding temporal fluctuations $\delta F_{\mathrm{b}}(t)$ and $\delta F_{\mathrm{r}}(t)$ of the fluorescent signals monitored in the "blue" and "red" detection channels will be random and not correlated. On the contrary, if double-colored species are formed and diffuse through V_{br}, the fluorescence fluctuations monitored in the two channels will be strongly correlated (see Figure 4.2b and c). Mathematically this can be expressed

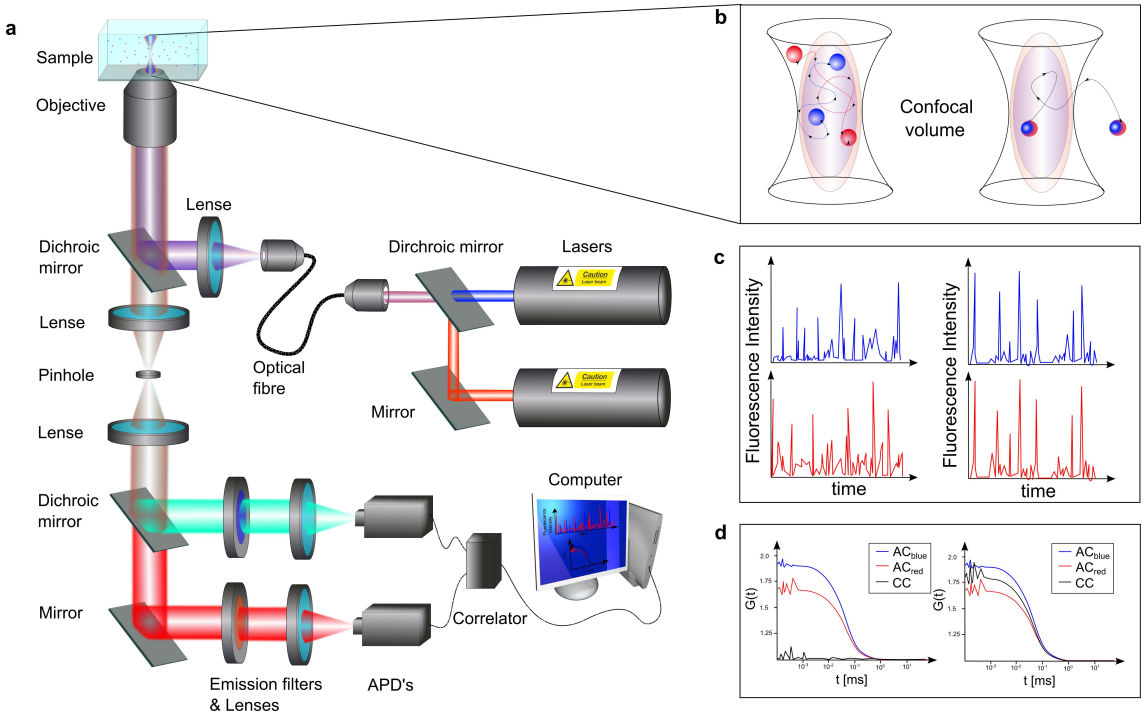

Figure 4.2: (a) Schematic setup of dual-color FCCS. (b) The two spatially overlapping observation volumes created by the "blue" and "red" laser with differently labeled species diffusing either independently (left) or linked (right). (c) Fluorescence fluctuation and the (d) corresponding correlation curves in relation to b.

by a cross-correlation function:[21]

$$G_{\mathrm{br}}(\tau) = \frac{\langle \delta F_{\mathrm{b}}(t) \delta F_{\mathrm{r}}(t+\tau) \rangle}{\langle F_{\mathrm{b}}(t) \rangle \langle F_{\mathrm{r}}(t) \rangle} \tag{4.1}$$

The amplitude $G_{\mathrm{br}}(\tau)$ of the cross correlation function is directly proportional to the concentration of the double-labeled species which is emphasized in Figure 4.2d. Additionally, the autocorrelation functions $G_{\mathrm{b}}(\tau)$ and $G_{\mathrm{r}}(\tau)$ can be also defined using equations analogous to eq. 4.1. By fitting these experimentally acquired auto- and cross-correlation curves with appropriate model functions (see SI), precise information about the average hydrodynamic radius of the nanoparticles, and the concentration and fraction of the double-labeled particles can be obtained. The average concentration of the double-labeled species C_{br} can be computed through:

$$C_{\mathrm{br}} = \frac{G_{\mathrm{br}}(0) V_{\mathrm{br}}}{G_{\mathrm{b}}(0) V_{\mathrm{b}} G_{\mathrm{r}}(0) V_{\mathrm{r}}} \tag{4.2}$$

Furthermore, the cross-correlation amplitude used in eq. 4.2 should be rectified with a factor accounting for the channels cross-talk.[104] Further details on the FCS setup and data evaluation are presented in the SI.

4.3. Results and Discussion

4.3.1. Solvent evaporation process from miniemulsions

Typical auto- and cross-correlation curves for the nanoparticles prepared with the SEED process following the aforementioned procedure (Figure 4.1) are shown in Figure 4.3. For comparison two control samples were also studied. The so called positive control sample (denoted "P") was prepared by dissolving both "colored" polymers together in the organic solvent. Subsequent mixing with water and surfactant followed by ultrasonication produced the emulsion of double-colored droplets and double-colored nanoparticles after solvent evaporation. For the preparation of a negative control sample (denoted "N"), the differently labeled polymers were separately dissolved and processed to two emulsions with different colors. After solvent evaporation, the two dispersions were mixed, resulting in a dispersion containing a mixture of pure "red" and pure "blue" PS nanoparticles. The preparation proce-

dures of the positive and negative control sample are further illustrated in Figure 4.7a,b of the SI, respectively.

As shown in Figure 4.3a, strong cross-correlation (black squares) was observed for the positive control sample. Its amplitude $G_{\mathrm{br}}(0)$ lies between the amplitudes of the autocorrelation curves, $G_{\mathrm{b}}(0)$ and $G_{\mathrm{r}}(0)$, as expected when only dual-labeled species are present in the studied sample. This finding is further confirmed by the almost identical values of the concentrations and hydrodynamic radii of "blue", "red", and "dual-colored" particles obtained from the fits of the autocorrelation and cross-correlation curves (see Table 4.1). The negative control sample SEED-N showed a very low level of cross-correlation (see Figure 4.3b). Using the cross-talk rectified $G_{\mathrm{br}}(0)$ value in eq. 4.2, we calculated that the concentration of dual-labeled particles in the SEED-N sample is almost negligible (see Table 4.1).

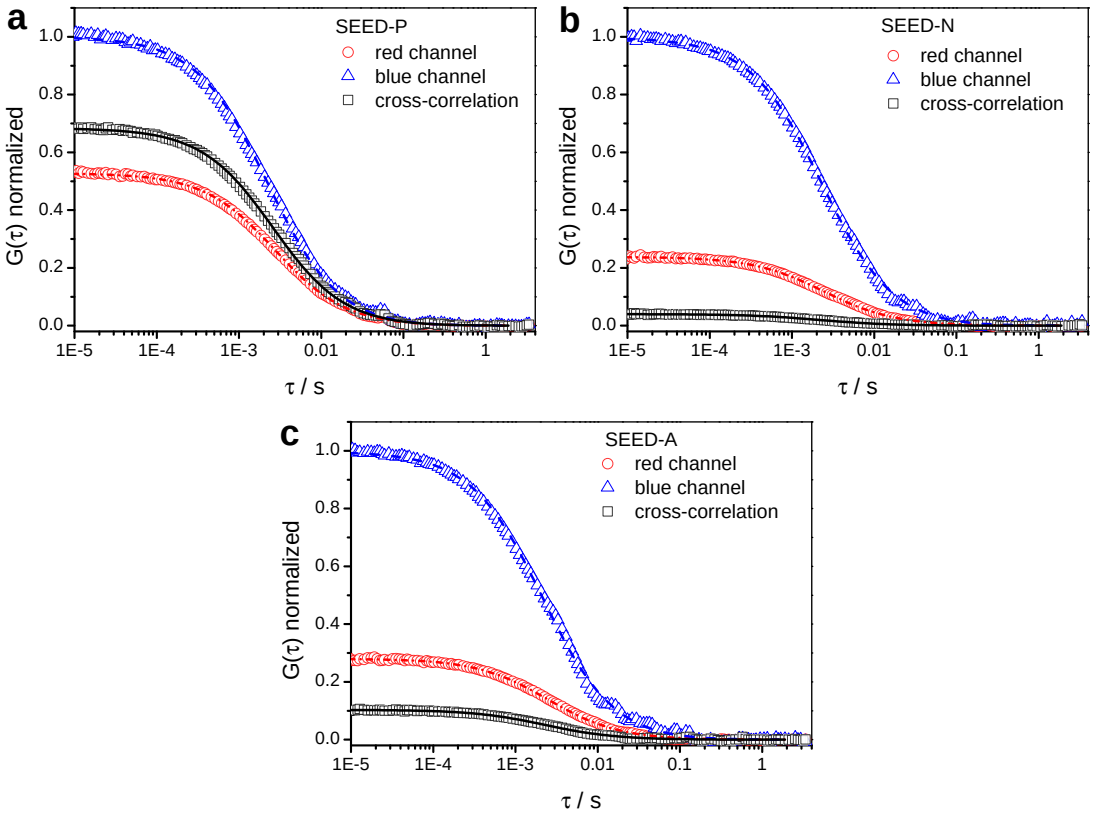

Figure 4.3: Normalized correlation curves (scattered symbols) and corresponding fits (lines) of the DC FCCS samples prepared by solvent evaporation: SEED-P (a), SEED-N (b), and SEED-A (c).

Table 4.1: Concentrations and Hydrodynamic Radii of the Nanoparticles Prepared by the SEED Process Calculated from the Autocorrelation and Cross-Correlation Curves sample channel concentration (nM) hydrodynamic radius (nm)

sample	channel	concentration (nM)	hydrodynamic radius (nm)
SEED-P	AC red	1.70 ± 0.52	51.3 ± 4.0
	AC blue	1.75 ± 0.21	49.6 ± 5.8
	CC	1.71 ± 1.19	52.5 ± 5.2
SEED-N	AC red	1.94 ± 0.60	46.3 ± 3.7
	AC blue	0.91 ± 0.11	51.1 ± 5.7
	CC	0.03 ± 0.02	44.4 ± 9.0
SEED-A	AC red	2.02 ± 0.62	46.8 ± 3.8
	AC blue	1.11 ± 0.13	47.6 ± 5.8
	CC	0.23 ± 0.16	46.5 ± 6.9

This result also shows that no aggregation happened in the final nanoparticle dispersion and verifies that the labeled polymers were not diffusing between the nanoparticles across the continuous phase. The actual (non control) sample SEED-A showed a higher degree of cross-correlation (Figure 4.3c) than the negative control sample, indicating that small but non negligible amount of coalescence between emulsion droplets occurred throughout the SEED process. Theoretically, one step of coalescence in a system with two differently colored droplets with the same initial concentration would lead to a concentration of dual-colored droplets C_{br} (and therefore nanoparticles) equal to half of the total concentration of droplets C_{i} ($C_{\mathrm{i}} = C_{\mathrm{r}} + C_{\mathrm{b}}$). Because in our case C_{br} is much below C_{i} (Table 4.1), the results clearly indicate that there is an average of less than two initial droplets forming one final nanoparticle.

4.3.2. Miniemulsion polymerization

As a second example, we examined the occurrence of coalescence during the synthesis of polystyrene nanoparticles by radical polymerization in miniemulsion with an approach similar to the aforementioned one. Small amounts of the "blue" and "red" labeled polystyrene also used for the investigations on the SEED process were dissolved in the styrene monomer to label the miniemulsion consisting in styrene

droplets dispersed in water. The positive control, negative control, and actual samples were prepared and studied by FCCS. The normalized autocorrelation curves and the corresponding fits are shown in Figure 4.5 of the SI, whereas the calculated values for the concentrations and hydrodynamic radii of "blue", "red", and "dual-colored" species are summarized in Table 4.2. The autocorrelation curves could be appropriately fitted utilizing eq. 4.4 with a two-component decay ($i = 2$). The first component reflects the particles ($R_h > 60$ nm) and the second, much smaller species ($R_h < 5$ nm) that are probably single or small aggregates of labeled polymer chains, given that there was no detectable nonpolymerized dye before the polymerizations (see SI). The amount of small species was significantly reduced by centrifugation. However, a small quantity still remained in the dispersions. Although the solubility of the labeled polymer is very low, some chains might be dissolved in the continuous phase. This hypothesis is supported by the fact that the measured fraction of small species f_i for the red dye (4 %) was lower than f_i for the blue dye (8 %), which can be correlated with the lower hydrophilicity of the red dye compared to the blue dye. Furthermore, as f_i is proportional to both the number concentration and the squared molecular brightness of the particular observed species (eq. 4.4),[64] the absolute quantitative evaluation of their concentrations becomes more complex. The positive control sample MEP-P (Figure 4.5a) exhibited significant cross-correlation. Since the cross-correlation curve exclusively represents the dual-colored nanoparticles whereas the autocorrelation curves also show contributions from the small single-colored species, the value of the cross-correlation amplitude $G_{br}(0)$ is slightly lower than the "ideal" one which should lie between $G_b(0)$ and $G_r(0)$ as described above. In contrast the negative control sample MEP-N (Figure 4.5b) showed only a very low amount of cross-correlation arising from the positive cross-talk of the FCS setup and from a low number of dual-colored nanoparticles aggregates most likely formed during the centrifugation. The actual sample MEP-A (Figure 4.5c) and the negative control sample MEP-N (Figure 4.5b) displayed a similar behavior, which indicates that the coalescence of droplets does not occur significantly during the miniemulsion polymerization of styrene. This observation is consistent with previous small-angle neutron scattering (SANS) measurements on droplets of deuterated styrene before and after polymerization that showed identical sizes.[195]

4.3.3. Interfacial polycondensation to inorganic nanocapsules

As a final example, the formation of silica nanocapsules by interfacial polycondensation of alkoxysilanes was investigated. For this purpose small amounts of the "blue" and "red" labeled PS described above were dissolved in a mixture of tetraethyl orthosilicate (TEOS), toluene, and hexadecane.[196] After mixing with an aqueous solution of surfactant and ultrasonication, TEOS underwent hydrolysis and condensation, yielding silica nanocapsules.[196] The normalized correlation curves for the measured and control samples and their fits are shown in

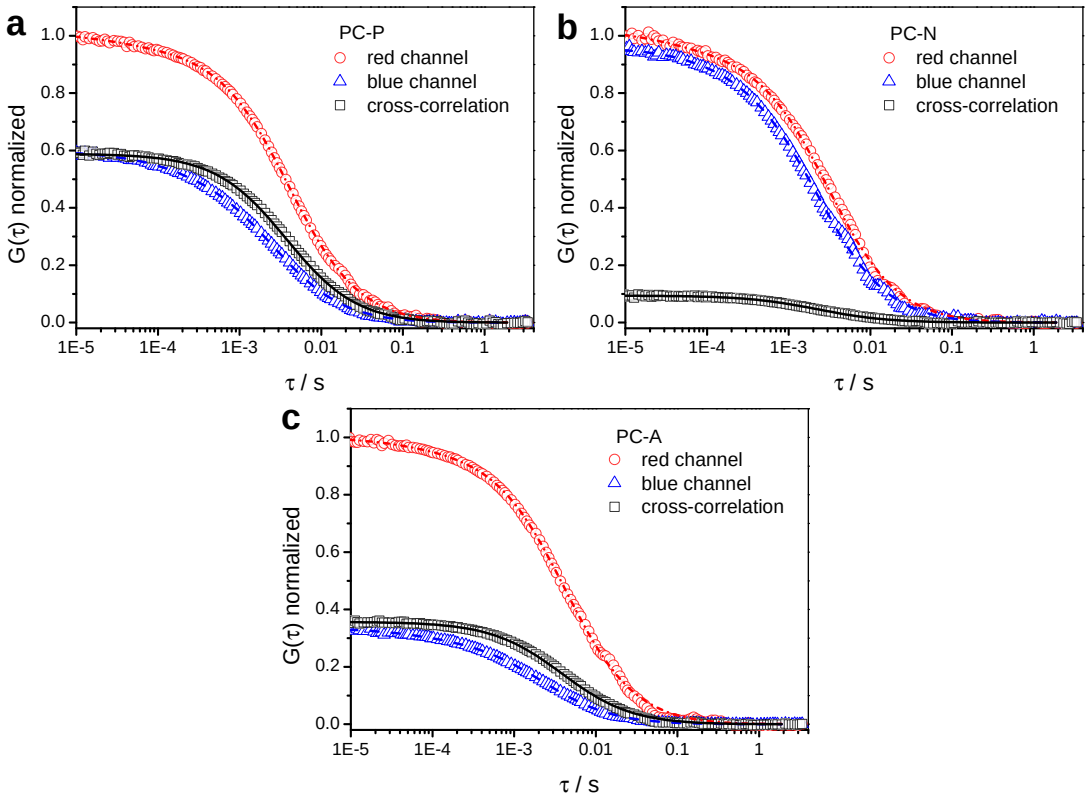

Figure 4.4: Correlation curves (scattered symbols) and corresponding fits (lines) of the DC FCCS samples prepared by interfacial polycondensation: PC-A (a), PC-N (b), and PC-A (c).

Figure 4.4, while the obtained data are summarized in Table 4.3. As in the miniemulsion polymerization two-component fits were required to appropriately represent the autocorrelation curves with the model eq. 4.4. The first component corresponds to the nanocapsules ($R_h > 49$ nm) and the second to a smaller species

($R_h < 3.5$ nm), which are the aforementioned single labeled polymer chains or their aggregates. Centrifugation of the samples to reduce the quantity of small species was not feasible since it caused aggregation of the nanocapsules. As expected, the positive control sample PC-P and the negative control sample PC-N displayed a high and negligible amount of the correlation curves for the actual and the positive control sample PC-A (Figure 4.4c and a) are very similar. This clearly demonstrates that coalescence between droplets of nonfully reacted alkoxysilanes occurred during the preparation of the nanocapsules and yielded dual-colored species. This observation explains the relatively large size distribution of similar silica nanocapsules measured by dynamic light scattering (DLS).[196]

4.4. Conclusion

In conclusion, we demonstrated that DC FCCS is a fast and versatile tool to study and quantify the coalescence of nanodroplets in emulsions or the aggregation of nanoparticles in suspensions. DC FCCS was applied to study three different procedures for the preparation of organic or inorganic nanoparticles. Depending on the process, large or low levels of coalescence could be detected. Our results unambiguously showed that coalescence did not play an important role in the preparation of polystyrene nanoparticles by emulsion-solvent evaporation process and miniemulsion polymerization. However, coalescence was a major factor during the formation of inorganic silica nanocapsules by interfacial polycondensation of alkoxysilanes.

4.5. Supporting Information

4.5.1. Additional data from DC FCCS experiments

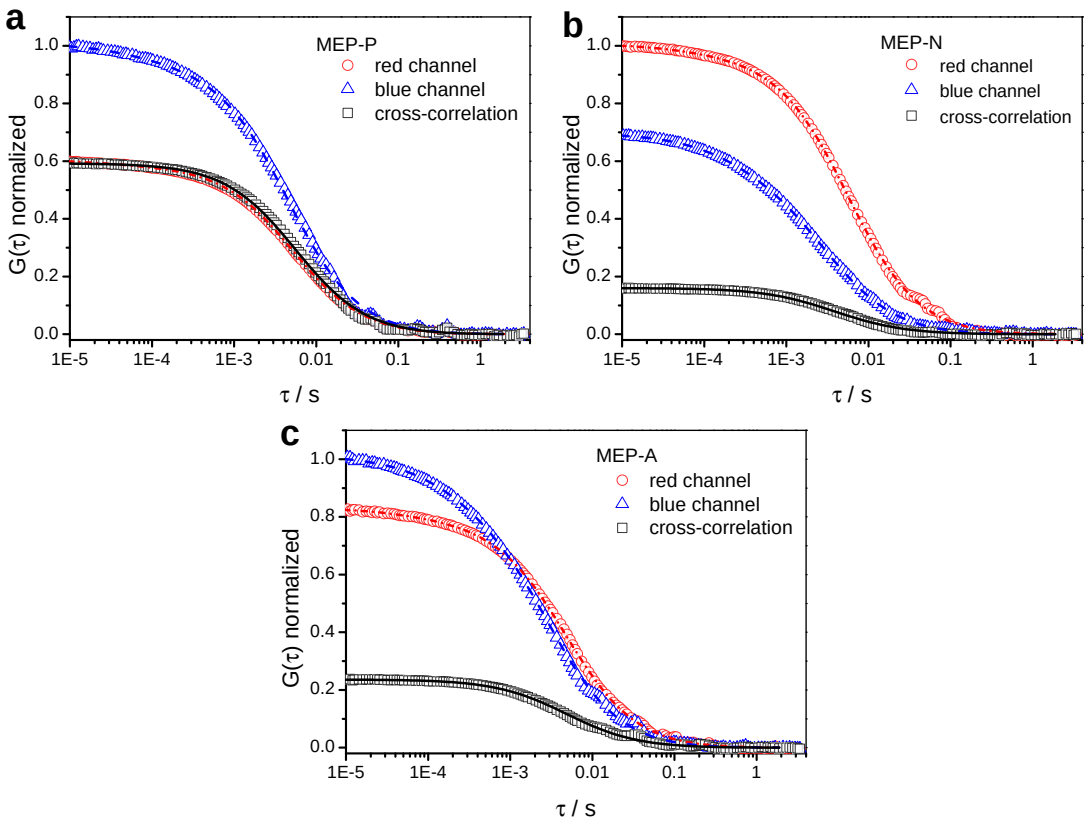

Figure 4.5: Correlation curves (scattered symbols) and corresponding fits (lines) of the DC FCCS samples prepared by miniemulsion polymerization MEP-P (a), MEP-N (b) and MEP-A (c).

Table 4.2: DC FCCS results of the samples obtained from miniemulsion polymerization (MEP). The concentrations and the hydrodynamic radii calculated from the autocorrelation curves are shown in contrast to the cross-correlation between the different channels.

sample	channel	apparent concentration (nM)	fractions	hydrodynamic radius (nm)
	AC red	0.54 ± 0.08	0.96 ± 0.02	82.9 ± 6.4
			0.04 ± 0.01	0.4 ± 0.5
MEP-P	AC blue	0.45 ± 0.06	0.93 ± 0.01	86.4 ± 10.7
			0.07 ± 0.01	1.5 ± 1.5
	CC	0.38 ± 0.18	1	94.2 ± 10.7
	AC red	0.33 ± 0.05	0.96 ± 0.02	88.8 ± 6.9
			0.04 ± 0.01	2.1 ± 1.5
MEP-N	AC blue	0.64 ± 0.09	0.80 ± 0.07	71.3 ± 8.8
			0.20 ± 0.02	5.4 ± 1.5
	CC	0.09 ± 0.04	1	75.4 ± 9.9
	AC red	0.95 ± 0.01	76.4 ± 5.7	
			0.05 ± 0.01	1.1 ± 0.7
MEP-A	AC blue	0.18 ± 0.02	0.82 ± 0.02	63.4 ± 8.0
			0.18 ± 0.01	4.5 ± 1.1
	CC	0.04 ± 0.02	1	84.3 ± 10.6

Table 4.3: DC FCCS results of the samples obtained by polycondensation of alkoxysilanes. The concentrations and the hydrodynamic radii calculated from the autocorrelation curves are shown in contrast to the cross-correlation between the different channels.

sample	channel	apparent concentration (nM)	fractions	hydrodynamic radius (nm)
	AC red	2.90 ± 0.35	0.95 ± 0.01	63.6 ± 4.4
			0.05 ± 0.01	0.49 ± 0.1
PC-P	AC blue	8.07 ± 1.05	0.88 ± 0.02	57.6 ± 10.7
			0.12 ± 0.01	3.1 ± 1.2
	CC	3.73 ± 1.59	1	67.5 ± 6.6
	AC red	2.39 ± 0.32	0.93 ± 0.02	49.4 ± 4.4
			0.07 ± 0.02	0.5 ± 0.5
PC-N	AC blue	4.19 ± 0.55	0.92 ± 0.02	51.4 ± 6.9
			0.08 ± 0.01	3.2 ± 2.6
	CC	0.28 ± 0.12	1	42.6 ± 6.4
	AC red	1.29 ± 0.16	0.96 ± 0.01	65.5 ± 5.4
			0.04 ± 0.01	0.9 ± 1.1
PC-A	AC blue	6.32 ± 0.85	0.88 ± 0.01	50.7 ± 6.1
			0.12 ± 0.01	1.7 ± 0.8
	CC	1.82 ± 0.79	1	69.1 ± 7.5

4.5.2. Materials and Synthesis

Materials

Sodium dodecyl sulfate (SDS, Alfa Aesar, 99%), cetyltrimethylammonium chloride (CTMA-Cl, Acros, 99%), toluene (Sigma Aldrich, 99.7%), tetrahydrofuran (THF, Sigma Aldrich, 99.9%), methanol (Fluka, 99.99%), dichloromethane (Fluka, 99.99%), chloroform (Acros, 99%), tetraethyl orthosilicate (TEOS, Alfa Aesar, 98%), V59 (Wako) and hexadecane (HD, Merck, 99%) were used as received. Styrene (Merck, 99%) was purified using a column packed with neutral aluminum oxide (Merck) before use. The initiator 2,2'-Azobis(2-methylpropionitrile) (AIBN, Fluka, 98%) was recrystallized from methanol prior to use. The synthesis of the dyes B504-MA and B612-MA (Figure 4.6) was based on syntheses reported in the literature.[1,197] Distilled water was used throughout the work.

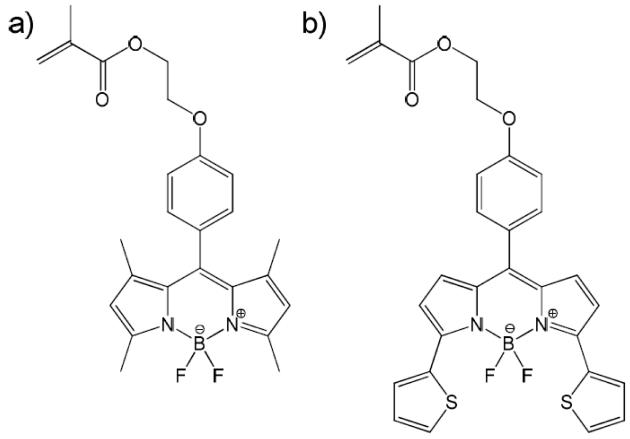

Figure 4.6: The polymerizable dyes B504-MA (a) and B612-MA (b) were used to label polystyrene chains for DC FCCS experiments.

Synthesis of labeled polymers

Copolymers of styrene and the dyes B504-MA or B612-MA were prepared by radical polymerization in solution. 12.5 mg AIBN, 7 mg of one dye and 2.5 g styrene were dissolved in 20 g THF. The solution was degassed 3 times by the freeze-thaw-technique and the polymerization was carried out at 80 ℃ in an oil bath for 40 h.

The copolymer was precipitated into 200 mL of a water: methanol mixture (20:80) and filtered. The solid copolymer was dissolved in 15 mL THF and reprecipitated 3 times to remove any unreacted dye and monomer. Afterwards, the copolymer was dried in vacuo. The copolymers of styrene and B504-MA or styrene and B612-MA were named PS-504 and PS-612, respectively. The apparent molecular weight of the copolymers PS-504 and PS-612 were measured to be 44,700 (PDI = 1.9) and 29,000 $g \cdot mol^{-1}$ (PDI = 2.2), respectively, as determined by GPC (Figure 4.9). Absorption and emission measurement of the dyes and of the polymers showed that there is no loss of fluorescence of the dyes after their copolymerization (Figure 4.10). The degree of labeling was 0.36 wt.% for PS-504 and 0.15 wt.% for PS-612 (Figure 4.11). No free dye was detectable in both polymers after the repeated reprecipitation (Figure 4.12) as verified by HPLC.

Preparation of the nanoparticles by solvent evaporation

100 mg of polymer (PS-504, PS-612) was dissolved in 2.5 g $CHCl_3$ and added to 20 g of an aqueous solution of SDS (1 $g \cdot L^{-1}$). A macroemulsion was obtained by stirring the mixture at 1250 rpm for 1 h. The macroemulsion was sonicated using a Branson W450-D sonifier with a 1/2"-tip at 70% amplitude in a pulsed regime (30 s sonication, 10 s pause) under ice-cooling. The obtained emulsions were then either directly treated (see preparation of samples for DC FCCS) or transferred in a 50 mL reaction flask and stirred at 500 rpm and 40 ℃ for 12 h. In the case of a further treatment, the emulsions were transferred to the reaction flask directly after the treatment. For the positive control sample, 50 mg of each polymer was used. A schematic of the preparation of the samples is shown in Figure 4.7. This figure is representative for all three kinds of nanoparticle/ nanocapsules preparation routines.

Preparation of the nanoparticles by miniemulsion polymerization

To synthesize nanoparticles by direct miniemulsion polymerization, 1.6 mg V59, 4 mg hexadecane and 995 mg styrene were added to 5 mg of PS-504 or PS612 to build the dispersed phase. A solution of 2 mg SDS in 20 g of water was subsequently added to the monomer solution. The mixture was emulsified for one hour

at 1250 rpm and submitted to ultrasonication for 2 min at 90% amplitude under ice-cooling. Afterwards, the polymerization was carried out in a closed 50 mL round bottom flask at 72 ℃ for 16 h under stirring. For the positive control sample, 2.5 mg of each polymer was used.

Preparation of the nanocapsules by polycondensation of alkoxysilanes

To synthesize nanoparticles by the interfacial reaction of TEOS, 5 mg of PS-504 or PS612 were dissolved in 1 g TEOS, 62.6 mg hexadecane and 500 mg toluene. Subsequently, a solution of 11.5 mg CTMA-Cl in 15 g water was added. The mixture was preemulsified for 5 min at 1000 rpm and subjected to ultrasonication for 2 min at 70% amplitude under ice-cooling in a pulse / pause regime of 30 s and 10 s. Afterwards, the polymerization was carried out at room temperature by stirring the miniemulsion at 1000 rpm in a closed vial for 48 h. For the positive control sample, 2.5 mg of each polymer was used.

4.5.3. Methods

Fluorescence correlation spectroscopy

DC FCCS measurements were conducted with a commercially available inverted microscope Olympus IX70 combined with a FluoView300 confocal laser scanning setup (Olympus), and a PicoQuant FCS upgrade comprising two separate single photon counting avalanche photodiodes τ-SPAD (PicoQuant). An Olympus UP-LSAPO 60XW 60x/1.2 water immersion objective was used. The utilized dyes were excited either with an argon-ion laser at $\lambda = 488$ nm or a heliumneon laser at $\lambda = 633$ nm. To separate the fluorescence of the different dyes into different channels a dichroic mirror combined with a 500-550 nm band pass and 635 nm long pass emission filters (Semrock) were used. To obtain the size and shape of the observation volumes, reference measurements were conducted using dyes which are appropriately excitable with the utilized lasers and with well-known diffusion coefficients, in our case Alexa Fluor 488® and Alexa Fluor 647® (Invitrogen), respectively.[198] Throughout all measurements, an eight-well, polystyrene chambered cover glass (Nalge Nunc International) was used as sample cell. In FCS, an auto-

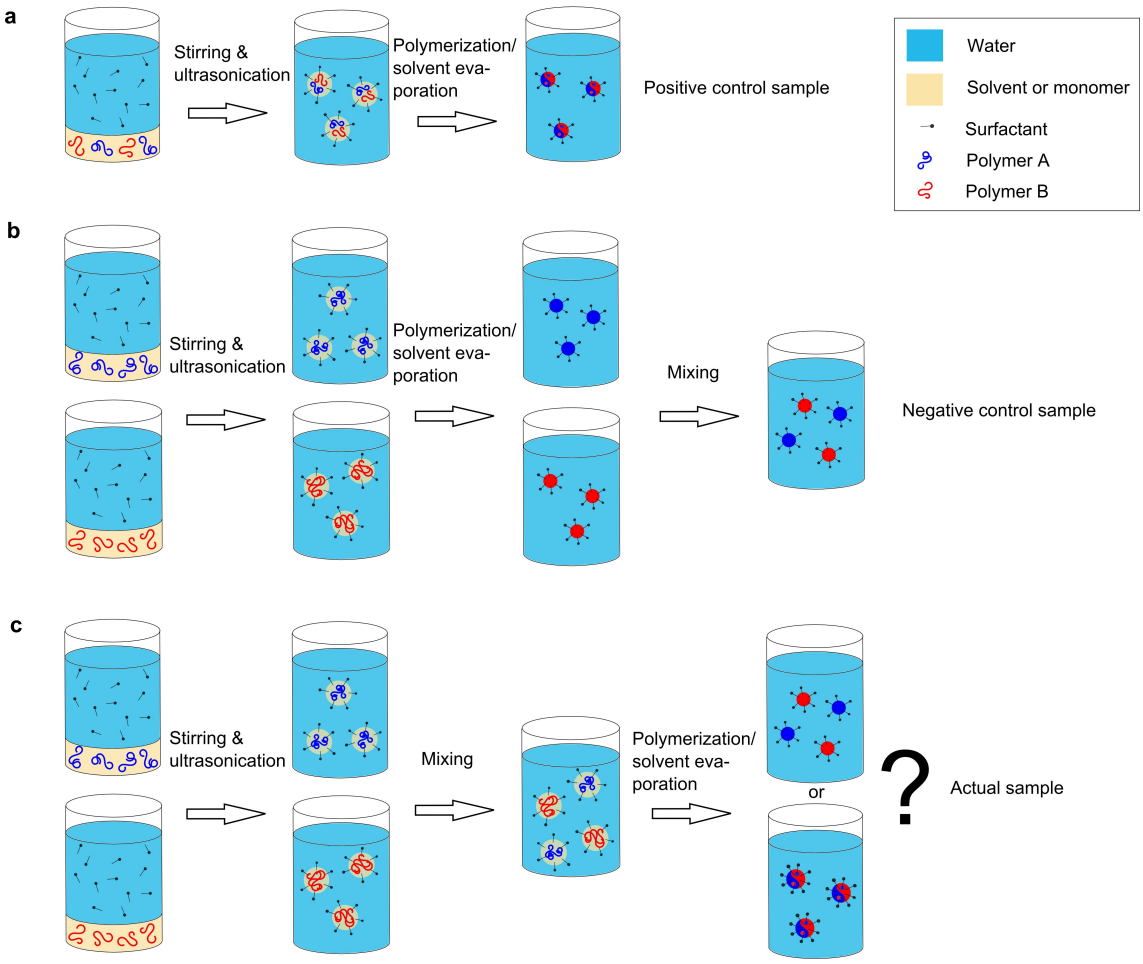

Figure 4.7: Sketch of the preparation of (a) positive, (b) negative and (c) actual sample representative for all three preparation routines.

correlation function can be derived from the measured temporal fluctuations of the fluorescence intensity $\delta F(t)$:

$$G(\tau) = \frac{\langle \delta F(t) \delta F(t+\tau) \rangle}{\langle F(t) \rangle^2} \tag{4.3}$$

For an ensemble of m types of freely diffusing species the autocorrelation function has following analytic form:

$$G(\tau) = \sum_{\mathrm{i}=1}^{\mathrm{m}} \frac{f_{\mathrm{i}}}{N \left(1 + \frac{\tau}{\tau_{\mathrm{Di}}}\right) \sqrt{1 + \frac{\tau}{S^2 \tau_{\mathrm{Di}}}}} \tag{4.4}$$

where N is the average number of chromophores in the observation volume V, τ_D its lateral diffusion time through V, f_i the fraction of species i ($0 \leq i \leq 1$) and S is the ratio of axial to lateral dimension of V ($S \approx 6$ in our experiments). By knowing the size of the observation volume from reference measurements with dyes with known diffusion coefficient (Alexa Fluor 488 and Alexa Fluor 647 in this work) the absolute concentration of chromophores C can be calculated by $C = N/V$. Furthermore the diffusion coefficient can be obtained from the relation $D = (r_0^2 + R_h^2)/4\tau_D$ where r_0 is the lateral dimension of V and the R_h the hydrodynamic radius which can be calculated from the Stokes-Einstein-relationship.[18]

For the dual color fluorescence cross-correlation spectroscopy studies additional reference measurements with a sample containing only the "blue" dye were conducted to obtain the amount of positive cross-talk. In our experimental conditions a bleed-through factor of 0.021 was found which means that 2.1% of the fluorescence of the "blue" dye is detected in the "red" cannel. All cross-correlation amplitudes where rectified therefrom as described in the literature.[104]

Gel permeation chromatography was used to estimate the average molecular weights of the polymers and their polydispersity index. The dried polymers were dissolved in THF at a concentration of 5 $mg \cdot mL^{-1}$ and filtered through a 0.45 μm Teflon filter. An elution rate of 1.0 $mL \cdot min^{-1}$ and both UV- (254 nm) and RI-detectors were used. The apparent molecular weights of the polymers were calculated using polystyrene standards.

HPLC measurements were conducted both on PS-504 and PS-612 before and after repeated precipitation in order to ascertain the purity of the polymer and the absence of free dye. HPLC measurements were performed with a gradient of THF + 0.1% TFA in water starting from a ratio of 60 to 40 up to 100 to 0 in 5 min. The flow was 1 $mL \cdot min^{-1}$ employing a reversed phase AB C_{18}-column (Macherey-Nagel) on a 1200 HPLC from Agilent Technologies. For detection, a DAD-Detector at a wavelength of 500 nm for PS-504 and at 600 nm for PS-612 was used. The measurements were performed with a gradient of THF and water starting from a ratio of 50 to 50 up to 100 to 0 in 10 min. The flow was 1 $mL \cdot min^{-1}$ employing a RP8e-column (Merck) on a 1200 HPLC from Agilent Technologies. Absorption and fluorescence emission spectroscopy on the dyes and the polymers was done on a Tecan Plate

Reader Infinite M1000 in THF solutions at concentrations of 0.1 $mg \cdot mL^{-1}$ and 1 $mg \cdot mL^{-1}$, respectively. For the quantification of labeling, the fluorescence emission of a concentration series of both dyes was run. Obtained intensities were corrected for background and solvent.

For electron microscopy, 10 μL of the dispersions of the nanoparticles or nanocapsules were diluted with 1 mL of distilled water. Droplets of 3.5 μL were then placed on small silica platelets for scanning electron microscopy (nanoparticles) and on copper-grids for TEM-measurements (nanocapsules). Both types of samples were sputtered with carbon on a BALZERS BAE250 for 5 s to prevent beam damage in the transmission and scanning electron microscopes. TEM observations were carried out on a JEOL 1400 at a voltage of 120 kV and images were taken with a GATAN Ultrascan 1000 CCD-camera. SEM-images were taken on a Zeiss 1530 Gemini Leo at varying voltages.

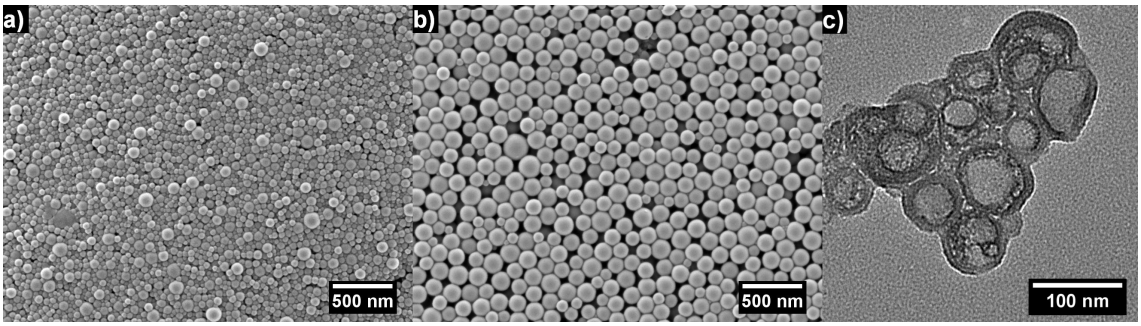

Figure 4.8: SEM micrographs of polystyrene nanoparticles prepared by: (a) the SEED process and (b) miniemulsion polymerization. (c): TEM-micrograph of silica nanocapsules.

4.5.4. Characterization data

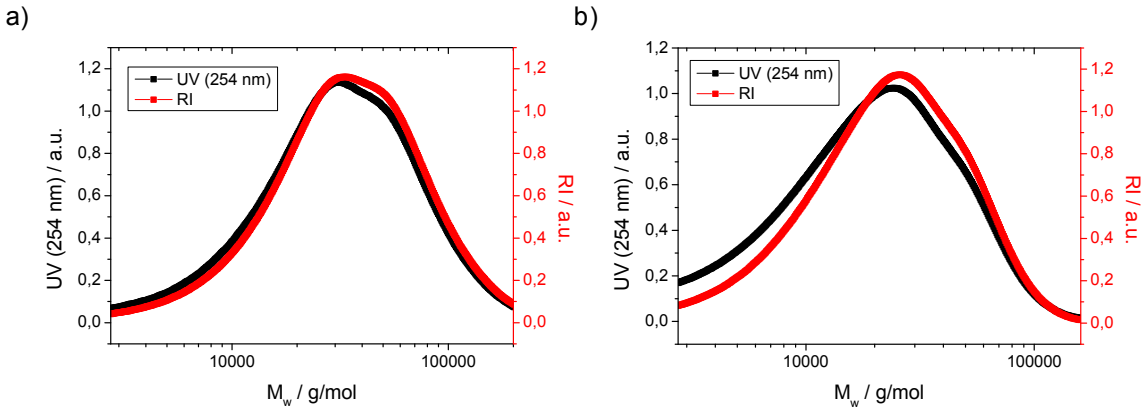

Figure 4.9: GPC traces of PS-504 (a) and PS-612 (b).

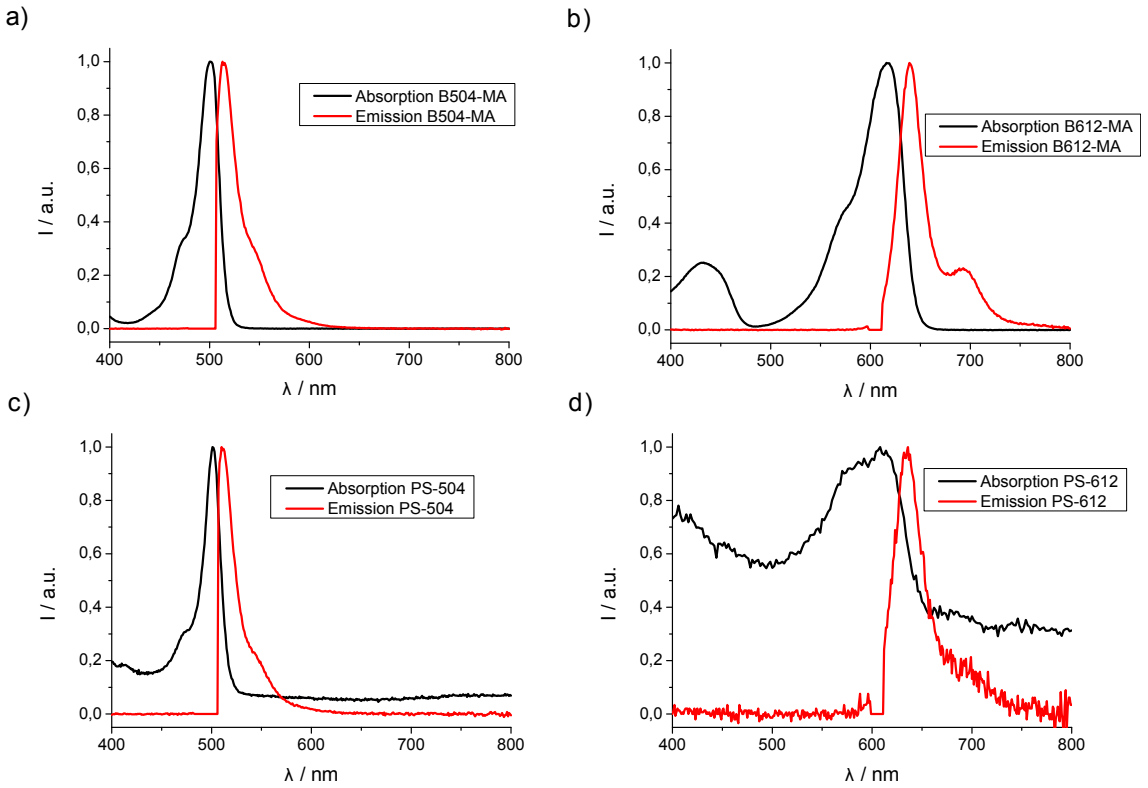

Figure 4.10: Absorption and emission spectra of B504-MA (a), B612-MA (b), PS-504 (c) and PS-612 (d). All spectra were corrected for background and solvent.

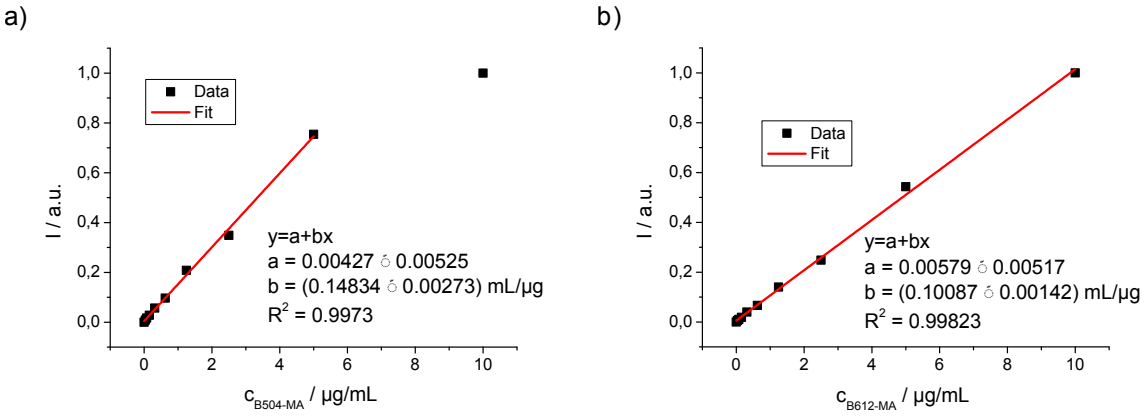

Figure 4.11: Plots for the quantification by fluorescence intensity measurements of the fluorescent labeling of the polymers PS-504 (a) and PS-612 (b). For a), the highest concentration of B504- MA was not included into the fit due to apparent self-quenching of the fluorescence. The intensities of PS-504 and PS-612 in a 1 mg · mL^{-1} solution in THF were 0.5371 and 0.1524, respectively, thereby being located in the linear region of both fits.

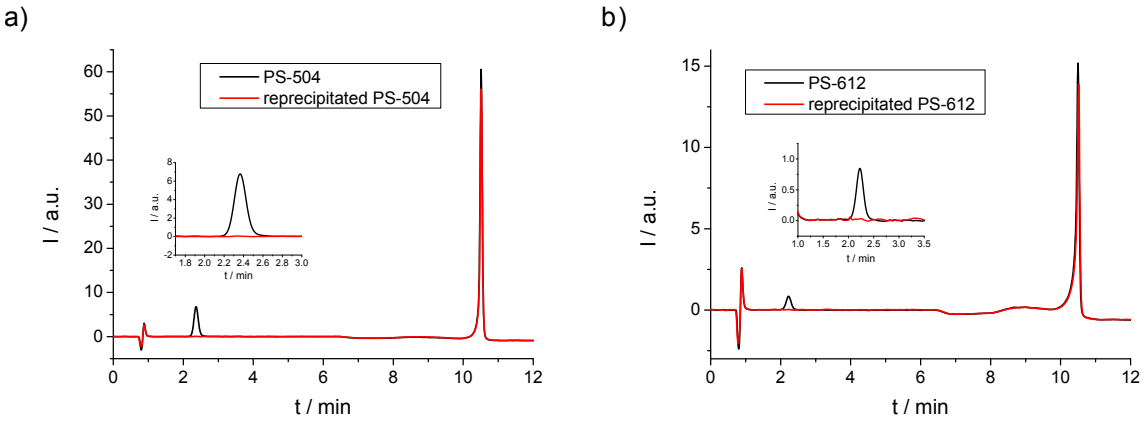

Figure 4.12: HPLC chromatograms for PS-504 (a) and PS-612 (b). Both inlays show that there is no free dye after repeated reprecipitation of the copolymers.

4.6. Acknowledgment

We would like to thank Niklas Kotmann for helping with the quantification of copolymerized dyes. Sandra Seywald and Beate Müller are acknowledged for the GPC characterization and the HPLC measurements, respectively. R.H.S. gratefully acknowledges financial support by the Fonds der Chemische Industrie (FCI).

5. Particle Formation in the Emulsion-Solvent Evaporation Process

The mechanism of particle formation from submicrometer emulsion droplets by solvent evaporation is revisited. A combination of dynamic light scattering, fluorescence resonance energy transfer, zeta potential measurements, and fluorescence cross-correlation spectroscopy is used to analyze the colloids during the evaporation process. It is shown that a combination of different methods yields reliable and quantitative data for describing the fate of the droplets during the process. The results indicate that coalescence plays a minor role during the process; the relatively large size distribution of the obtained polymer colloids can be explained by the droplet distribution after their formation.

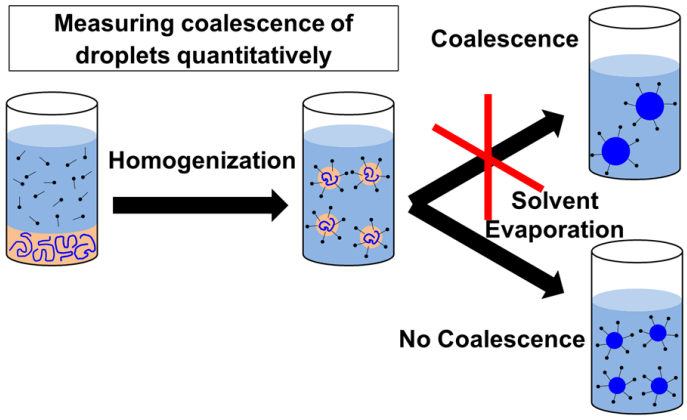

Reproduced with permission from:
R. H. Staff, D. Schaeffel, A. Turshatov, D. Donadio, H.-J. Butt, K. Landfester, K. Koynov, D. Crespy: Unraveling the Mechanism of Particle Formation in the Emulsion Solvent Evaporation Process, *Small*, **2013**, *9*(20), 3514-3522.

5.1. Introduction

Dispersions of nanoparticles are prepared either by heterophase polymerization, such as emulsion[168] or miniemulsion polymerization,[132,167] or by other processes that employ presynthesized polymers.[199] Among the latter processes, the preparation of nanoparticles by the so-called Ouzo effect and by solvent evaporation from emulsion droplets are probably the most studied techniques due to their versatility.[200] The Ouzo effect, also called nanoprecipitation or the solvent displacement technique, is based on the supersaturation and nucleation of oil droplets in water caused by the addition of water to a solution of oil.[201] The Ouzo effect is observed in the metastable region of the phase diagram between the spinodal and binodal curves. This method has been successfully applied to the preparation of nanoparticles of various polymers.[202,203] Generally, the formation of particles is spontaneous. For particular polymers with strong hydrogen bonding, such as polyamide 6, high shearing devices are required.[204]

In contrast to the Ouzo effect, in which droplets are created by liquid-liquid nucleation, the preparation of polymer nanoparticles by the so-called emulsion-solvent evaporation technique is based on liquid-solid nucleation in confined environments caused by the evaporation of a solvent. We abbreviate this process as SEED, for solvent evaporation from emulsion droplets. From a practical point of view, presynthesized polymers are dissolved in a good solvent and emulsified with a stabilizer,[22] thereby forming a polymeric emulsion. The solvent is then evaporated through the continuous aqueous phase and the polymer precipitates to yield the particles. The major advantage of the SEED process is the absence of impurities, such as toxic residual monomer, unreacted transfer agent, or catalyst, in the final colloids, which is important for applications in pharmacy or electronics. Therefore, the SEED process has been used extensively for the preparation of biodegradable microparticles,[205] for unconventional nanoparticles from semiconducting polymers[206] or from semicrystalline polymers,[26] and for redox-responsive nanocapsules.[27] The nanoparticles can be further compartmentalized[167] by introducing a nonsolvent for the polymer in the dispersed phase,[173,207] by employing block copolymers for microphase separation in the particles,[25,208–212] or both simultaneously.[25] However, the size distribution of the colloids obtained by the SEED process is large compared to the particles prepared by heterophase polymerization. Therefore, a deep

understanding of the mechanism of nanoparticle formation is needed to gain better control over the SEED process and the final particle properties. Indeed, the size and size distribution of the nanoparticles are dependent on many effects and parameters, for which each contribution cannot be easily isolated. For example, the temperature alone influences the evaporation speed of the solvent, the viscosity of the dispersed and continuous phases, the solubility of the different chemicals, the different interfacial tensions of the system, and the coefficient of diffusion of the droplets.

The coalescence between nanodroplets is another important effect that may strongly influence the polydispersity of the final nanoparticles. For example, the occurrence of coalescence during the formation of ethyl cellulose (EC) and poly(lactic acid) (PLA) nanoparticles by the SEED process was investigated by dynamic light scattering (DLS).[32] In this work, the aggregation ratio A was defined as the average number of droplets necessary to form one polymer nanoparticle. A was evaluated by measuring the average droplet and particle sizes by DLS with the following formula:

$$A = \frac{m_{\mathrm{P/NP}}}{m_{\mathrm{P/Drop}}} = \frac{\rho}{c\left(\frac{D_{\mathrm{Drop}}}{D_{\mathrm{NP}}}\right)^3} \tag{5.1}$$

Here, $m_{\mathrm{P/NP}}$ is the mass of the polymer in the particles, $m_{\mathrm{P/Drop}}$ the mass of the polymer in the droplets, ρ the density of the polymer in the nanoparticles, c the concentration of the polymer in the dispersed phase, D_{Drop} the average diameter of the nanodroplets, and D_{NP} the average diameter of the nanoparticles. Values of A between 9 and 32 were reported for EC nanoparticles depending on the viscosity of the dispersed phase, whereas an A value of 4 for PLA was found to be independent of the viscosity.[32] On this basis, together with zeta potential measurements, the authors proposed that coalescence was significant in the case of EC and negligible for PLA. Loxley and Vincent assumed that coalescence of droplets was responsible for the broad size distribution of poly(methyl methacrylate) microcapsules prepared by the SEED process.[213] Fryd and Mason studied the decrease of the average hydrodynamic diameters of emulsion droplets upon the SEED process with DLS.[33] They found a quadratic relationship between droplet shrinkage per time unit and the volume fraction of highmolecular- weight oil. Although in some of the previous studies coalescence was assumed to occur during the SEED process, it was never

evidenced by direct methods.

Herein, we aim to unravel the mechanism of formation of nanoparticles produced by the SEED process. This is of critical importance for optimizing the properties of the produced nanoparticles. We pay particular attention to possible droplet coalescence, because it may strongly affect the final size distribution. The occurrence of coalescence was studied with both direct and indirect methods. Indirect measurements were carried out by monitoring the droplet size by DLS or the droplet concentration by fluorescence correlation spectroscopy (FCS) during the SEED process. On the other hand, direct measurements relied on the concomitant presence of two differently labeled polymer chains in the same particles, which was verified by fluorescence resonance energy transfer (FRET) and dual-color fluorescence cross-correlation spectroscopy (DC FCCS).

5.2. Results and Discussion

5.2.1. Tentative Monitoring of the SEED Process by DLS and Zeta Potential Measurements

The average coefficients of diffusion of the droplets and their tentative conversion to hydrodynamic diameters were estimated by DLS directly after ultrasonication in 30 min steps. The measurements were used to calculate the aggregation ratio A proportional to the ratio of initial droplet diameter D Drop to the final particle diameter D_{NP}.[32] The calculation requires knowing the values of the concentration c of the polymer in the dispersed phase and the true density ρ of the polymer nanoparticles. The density of the polymer nanoparticles was assumed to be identical to the density of the polymer in bulk. This assumption is usually correct for particles without pores and was verified by other groups with gradient ultracentrifugation[214] and small-angle neutron scattering.[32] In our case, the same assumption was made given the fact that we could not detect porous particles by transmission electron microscopy or scanning electron microscopy (SEM) measurements. The measured hydrodynamic diameter in dependence on the evaporation time t is shown in Figure 5.1 a for a polystyrene (PS)/chloroform-in-water miniemulsion. The first measurement ($t = 0$) was performed directly after ultrasonication and was taken

as an estimation of the initial droplet diameter. As expected, a decrease of the diameter with time was observed until a plateau was reached after 3 h, similarly to results shown by others.[32] After several days, the nanoparticles still displayed the same diameter and therefore this value was taken as the final diameter of the nanoparticles. The A value [Eq. 5.1] for the measured system was calculated to be about 14, which indicated that on average 14 droplets merged to create one particle. This is to be compared with reported A values of 32 and 4 for EC nanoparticles and PLA nanoparticles, respectively.[32]

The concentration c is dependent on the amount of solvent left in the system after ultrasonication. We noticed that although the ultrasonication was performed under ice cooling, some chloroform was evaporated before $t = 0$ during the sonication step. The amount of chloroform in the emulsion after ultrasonication was determined by distillation. Only 1.4 g of chloroform was recovered out of the 2.5 g chloroform initially added. The corrected aggregation number was then refined to $A_{\text{corr}} \approx 8$ instead of $A \approx 14$ previously calculated.

One also needs to take into account that emulsions or suspensions measured by DLS are usually diluted prior to the measurements. It is hence important to ascertain that there is no influence of the diluent and the dilution on the measured diameters. Prepared polymeric emulsions of PS were diluted not only with water saturated with different solvents, such as chloroform (sample Dil-1), toluene (sample Dil-2), and dichloromethane (sample Dil-3), but also with aqueous solution of surfactant, and aqueous solution of surfactant saturated with the different solvents. The polymeric emulsions were diluted at different concentrations with the different diluents and the hydrodynamic diameter was measured (Figure 5.2). Three main trends can be recognized for each graph. Firstly, the samples diluted with solvent-saturated water displayed a significantly larger diameter than the samples diluted with pure water or aqueous solution of sodium dodecyl sulfate (SDS). Secondly, the hydrodynamic radii for the samples diluted with solvent-saturated water became smaller as the dilution was decreased, that is, high dilutions yielded larger particles than low dilutions with solvent-saturated water. Thirdly, the samples diluted with water or with an aqueous solution of SDS displayed a roughly constant diameter. The presence of species with lower coefficient of diffusion upon diluting with solvent-saturated water was attributed to the swelling of the polymeric droplets. The interpretation of the results is delicate as the dilution can involve contradictory

effects for which even a qualitative prediction is difficult to estimate. For instance, the dilution with water also dilutes the surfactant but allows a larger diffusion of the solvent in the continuous phase. A significant contribution of the dilution to the DLS results was also reported by Goddeeris *et al.*[215] They found that factors as diverse as droplet shape, droplet size distribution, angle of the incident laser beam, and the potential presence of surfactant micelles all influence the measurement.

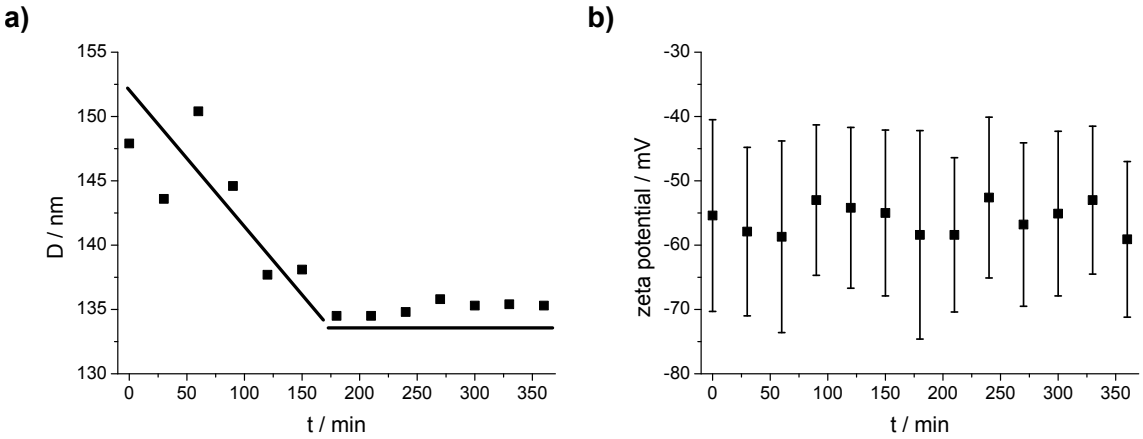

Figure 5.1: a) Hydrodynamic diameters of chloroform droplets containing PS versus time during the SEED process. The lines are meant to guide the eye. b) Zeta potential as a function of time of evaporation (sample Time-1) after ultrasonication.

In addition, the hydrodynamic boundary condition may introduce an uncertainty. The hydrodynamic radius of a droplet or a nanoparticle is calculated from the average coefficient of diffusion of the colloids by the Stokes-Einstein equation. The validity of this relationship for emulsions is assumed in most reports.[29,32,33] Hadamard[216] and Rybczynski[217] introduced a viscosity-dependent boundary condition for describing a droplet in another liquid. Under full slip conditions (gas bubble), a 50 % higher velocity is obtained compared to the velocity under no slip conditions (solid sphere). Although these studies are related to gravity-induced and friction-retarded velocities, they may be considered in polymeric emulsions. If partial slip appears, the droplet's size would be underestimated compared to the size of a hard sphere and would result in an overestimated A value. Furthermore, the surface of the droplet is covered with the surfactant, thus resulting in a retardation of the droplet's motion by introduction of a surface tension gradient.[218] This effect has been observed in several studies,[219–221] with all results pointing to the occurrence of no slip once

the surface of the droplet is covered by surfactant. However, a specific view on nanometer- sized droplets as well as the consideration of random Brownian motion is still missing. Additionally, the droplets in this study are not completely covered by surfactant due to the low surfactant concentration; thus, partial slip and therefore a higher diffusion coefficient and a resulting smaller diameter may be obtained by tacitly assuming the utter validity of the Stokes-Einstein equation. In conclusion, there are too many conflicting factors, mainly diluent and theoretical considerations, to build a model for particle formation with DLS results as the sole basis under the reported experimental conditions.

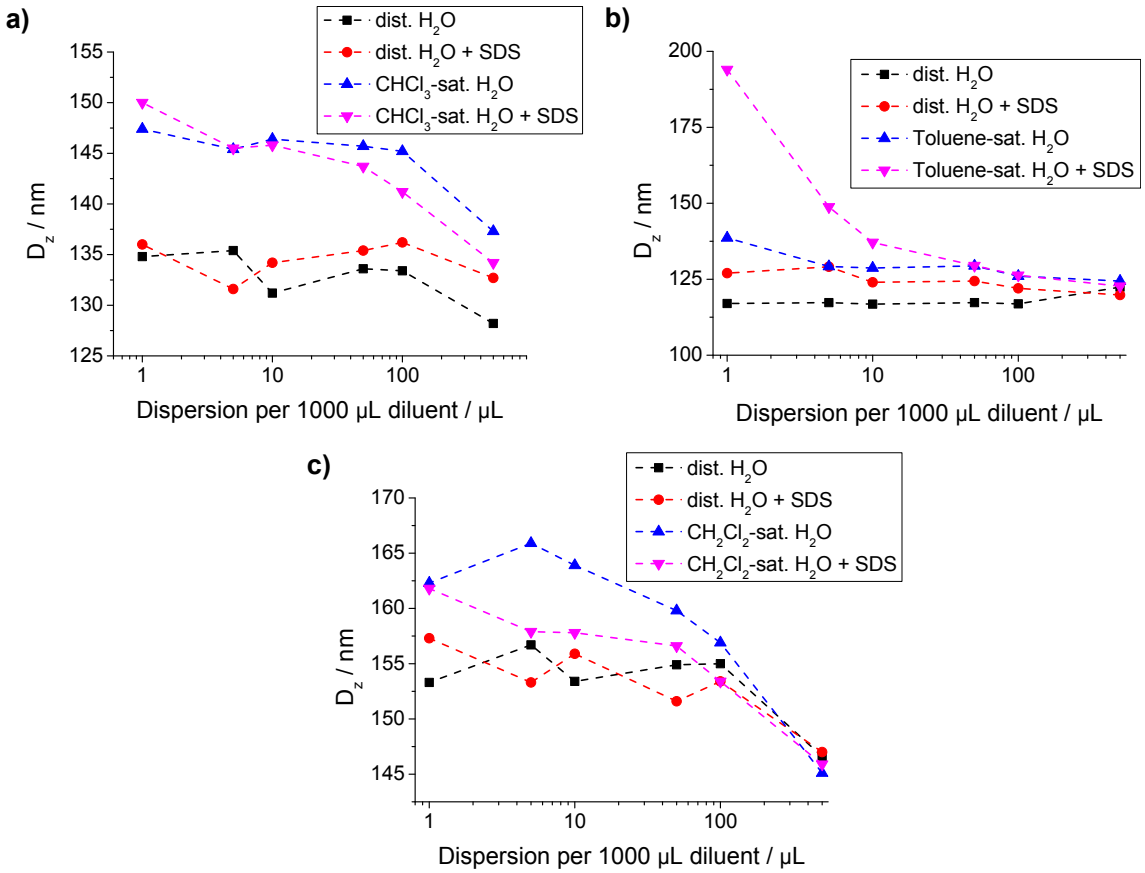

Figure 5.2: The hydrodynamic diameter of polymeric emulsions is highly dependent on dilution and diluents: a) $CHCl_3$, sample Dil-1; b) toluene, sample Dil-2; c) CH_2Cl_2, sample Dil-3).

The zeta potential of the PS polymeric emulsions was measured directly after sonication and in 30 min steps during the SEED process. As shown in Figure 5.1b, the zeta potential did not change significantly with respect to the experimental error.

Previous studies have demonstrated that the zeta potential could either decrease or increase/stagnate during the SEED process and the latter phenomenon was interpreted as a consequence of coalescence.[32] Indeed, the change of zeta potential was viewed as a temporary depletion of SDS at the droplets' surface induced by the coalescing droplets. However, as for DLS measurements, dilution was necessary to perform the zeta potential measurements and therefore the partition of the surfactant as adsorbed species on the particles' surface or molecularly dissolved species were not the same for undiluted and diluted samples. Therefore, we tend to view the zeta-potential measurements to be as biased as the DLS measurements under the reported experimental conditions, because the influence of dilution is too significant to draw conclusions from these results.

5.2.2. Estimation of Nanoparticle Concentration by FCS

FCS can deliver information about the number of fluorescent diffusing species in a specific volume and thereby about the concentration of fluorescently labeled species.[222–224] Almost no change of the concentration of fluorescent species was detected in the 240 min after sonication (Figure 5.3a), thus indicating that coalescence did not occur at a significant level. This observation was confirmed by measurements of the average particle brightness (SI), which should increase upon coalescence but did not vary significantly with time (Figure 5.3b). In principle, the hydrodynamic radii of

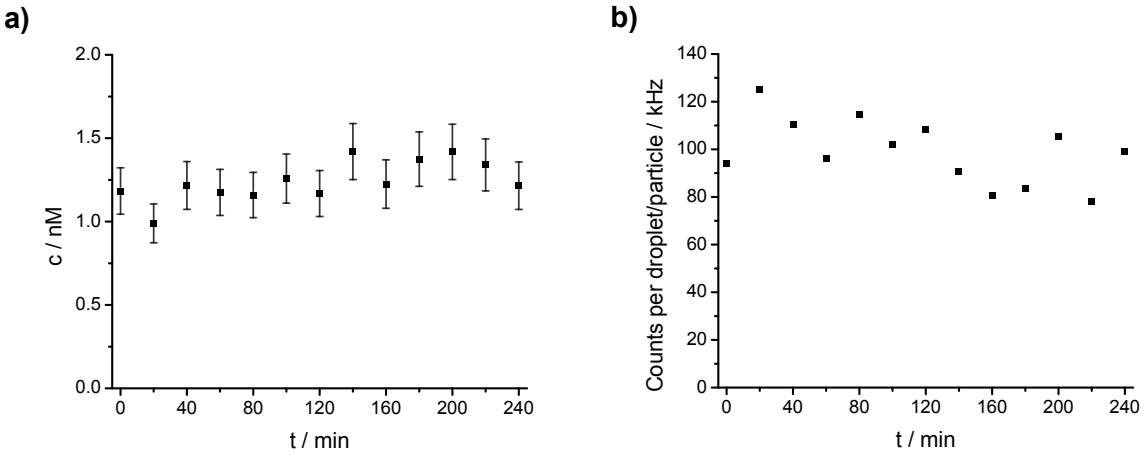

Figure 5.3: Temporal evolution of the concentration c of droplets or particles in the observation volume (a) and the photon counts per droplet/particle (b).

fluorescent species can also be extracted from the coefficient of diffusion measured by FCS. However, since diluting to a nanomolar concentration is required for a proper use of FCS,[174,225] the same problems as for DLS were observed while diluting the system (data not shown), that is, the results were dependent on dilution.

5.2.3. Direct Determination of Coalescence by FRET and DC FCCS

In principle, the occurrence of coalescence can be detected by the demonstration of the coexistence of two labeled species in the same particle when starting with separately labeled droplets. In the case of FRET measurements, the coexistence can be detected by a change of fluorescence decay of a donor fluorophore. Therefore, polystyrene chains were labeled separately with two dyes (FRET donor and FRET acceptor), which have already been used for FRET measurements.[226,227] Positive (FRET-P) and negative (FRET-N) samples were obtained (Figure 5.4) by preparing particles from emulsions with the two labeled polymers in the same droplets and by mixing separately labeled dispersions of polymer particles, respectively. As expected, the positive control sample shows a fast decay of donor fluorescence, that is, a short lifetime, whereas the decay for the negative control sample was much slower (Figure 5.5). The actual sample (FRET-A) shows a behavior very close to that of the negative control sample (Figure 5.5). To obtain more quantitative information we determined the donor fluorescence decay curves for several possible scenarios by measuring defined mixtures of the FRET-P and FRET-N. Decay 2 represents a possible situation when 80 % of all droplets coalesce but the process stops after coalescence of two droplets. If a larger number of droplets took part in the formation of a final "super droplet", the expected decay of FRET-A would become even shorter. Decay 4 (Figure 5.5) corresponds to a situation when approximately 20 % of all droplets coalesce in a binary manner. Thus, the real decay of FRET-A reveals that only a very small fraction of all droplets is involved in coalescence. In general, the energy transfer occurs over short distances only, because the Förster radius for the 9-vinylphenanthrene (VPA)-[1-(4-nitrophenyl)-2-pyrrolidinmethyl] acrylate (NPP) donor-acceptor pair is $R_0 = (2.47 \pm 0.03)$ nm.[226] Therefore, even if two droplets coalesce, it is possible that the two differently labeled polymers are not mixed intimately and therefore the FRET measurements only indicate that the two

fluorescently labeled species are not spatially close to each other.

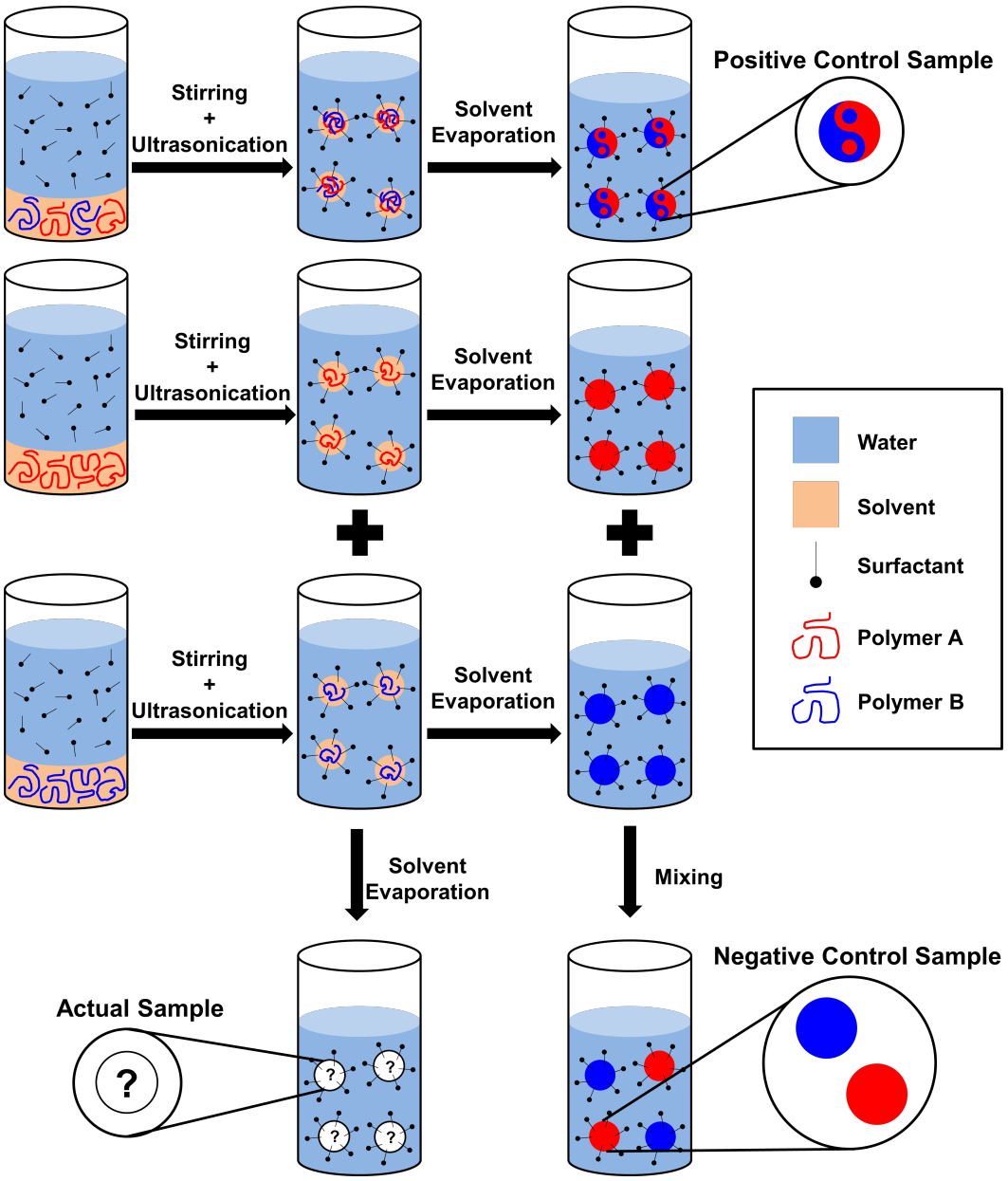

Figure 5.4: Scheme of the preparation of the samples for both DC-FCCS and FRET investigations. The colors represent two different polymers or two differently labeled polymers.

On the other hand, DC FCCS retrieves information on the possible coexistence of two differently labeled polymers in the same nanoparticle or droplet even if they are spatially separated.[34] That is why we used DC FCCS to investigate further the

process of droplet coalescence by studying a positive control, a negative control, and an actual sample prepared in a way similar to that used in the FRET experiments. The experimentally measured correlation curves and their fits with Equation 5.6 are shown in Figure 5.6 . The results of the fits are listed in Table 5.2 (SI). The positive control sample FCCS-1-P showed the expected strong cross-correlation, that is, a large value of $G_{12}(0)$ (see Figure 5.6a). The almost identical values (Table 5.2) for the concentration of the blue-, red-, and double-labeled nanoparticles obtained from the fits of the two autocorrelation and the cross-correlation curves indicate that all nanoparticles in this sample contain both blue- and red-labeled polymers. This finding is further supported by the values of the corresponding hydrodynamic radii (Table 5.2), which were also found to be the same in the range of the computational errors. The negative control sample FCCS-1-N revealed a very low amplitude of crosscorrelation (Figure 5.6b). Furthermore, when the cross-correlation function was corrected by taking cross-talk into account, its amplitude turned almost to one. The computed concentration of double-labeled particles C_{12} in Table 5.2 was negligible. The sample FCCS-1-A displayed a non negligible magnitude of cross-correlation even after the correction from cross-talk (Figure 5.6c). The computed concentration C_{12} also indicates that some coalescence occurred during the solvent evaporation process. The fraction of the blue-red particles $f_{\text{blue-red}}$ can be estimated as $f_{\text{blue-red}} = c_{\text{cc}}/\left(c_{\text{red}} + c_{\text{blue}} - c_{\text{blue-red}}\right) \cdot 100\% = 8.0 \pm 6.3\%$, with $c_{\text{blue-red}}$ the concentration of double-labeled species detected by cross-correlation; 8% is a small fraction.

To better quantify the extent of coalescence, we derived a simple model based on the following assumptions:

a) Initially, the concentration of double-labeled species is zero.

b) The probability of coalescence between the same and/or different colored droplets is equal.

c) In each step $i+1$ of coalescence, all the droplets created in the previous step i coalesce in a binary manner to form new droplets.

d) The number of droplets approaches infinity. Taking these assumptions into consideration, it is possible to calculate the relative fraction of double-labeled droplets/particles $f_{\text{blue-red}}$ after a particular coalescence "step" i from:

$$f_{\text{blue-red}}(i) = \frac{\left[\left(c_{\text{red}} + c_{\text{blue}}\right)^{2i} - c_{\text{red}}^{2i} - c_{\text{blue}}^{2i}\right]}{\left(c_{\text{red}} + c_{\text{blue}}\right)^{2i}} \cdot 100\% \tag{5.2}$$

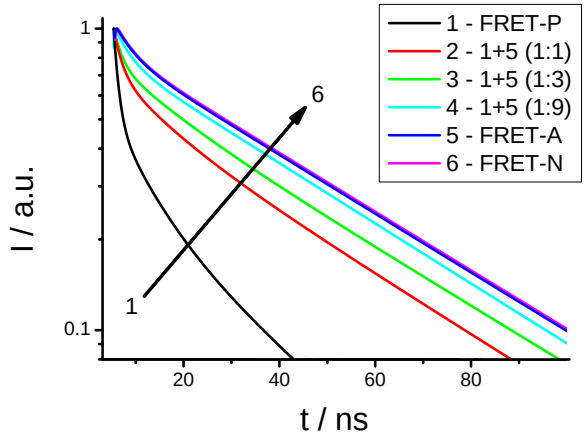

Figure 5.5: Fluorescence decay of the positive (FRET-P), negative (FRETN), and actual (FRET-A) samples, and different mixtures of FRET-P and FRET-A with different ratios.

Here, c_k (k = blue or red) is the concentration of the differently labeled particles. This model shows that already after a few steps almost all droplets should be dually labeled. The expected relative amount of double-labeled particles N can be calculated by $N = f_{\text{blue-red}}/f_{\text{blue-red}}(i = 1)$. Therefore, since (8.0 ± 6.3) % of all droplets were found to be dually labeled, this means that (17.4 ± 13.7) % of the initial droplets have coalesced assuming that only one "step" ($i = 1$) has occurred. Please note that this number decreases even further when one considers further steps ($i > 1$). We conclude that on average much fewer than two initial emulsion droplets form one final nanoparticle during the entire solvent evaporation process. In more detail, from the number of coalesced droplets N one can then calculate the A value defined before by:

$$A = \frac{100\%}{100\% - \frac{N}{2}} \tag{5.3}$$

assuming that $i = 1$ coalescence steps occurred. The (17.4 ± 13.7) % of initially present droplets undergoing coalescence mentioned before amounts to an A value of only (1.10 ± 0.08); for example, 1.10 droplets form one final particle, which is much less than found previously.[32] The FCS measurements were repeated with a different set of samples prepared by using the same procedure but with toluene instead of chloroform as solvent (FCCS-2). The results of the FCCS experiments are listed in

Table 5.3 and shown in Figure 5.7a. The amount of double labeling was (14.2 ± 5.9) %, meaning that (28.9 ± 12.1) % of the original droplets have coalesced, which yields an A value of (1.17 ± 0.08). This is slightly larger than in the case of chloroform and is probably caused by the longer time needed to evaporate the less volatile toluene.

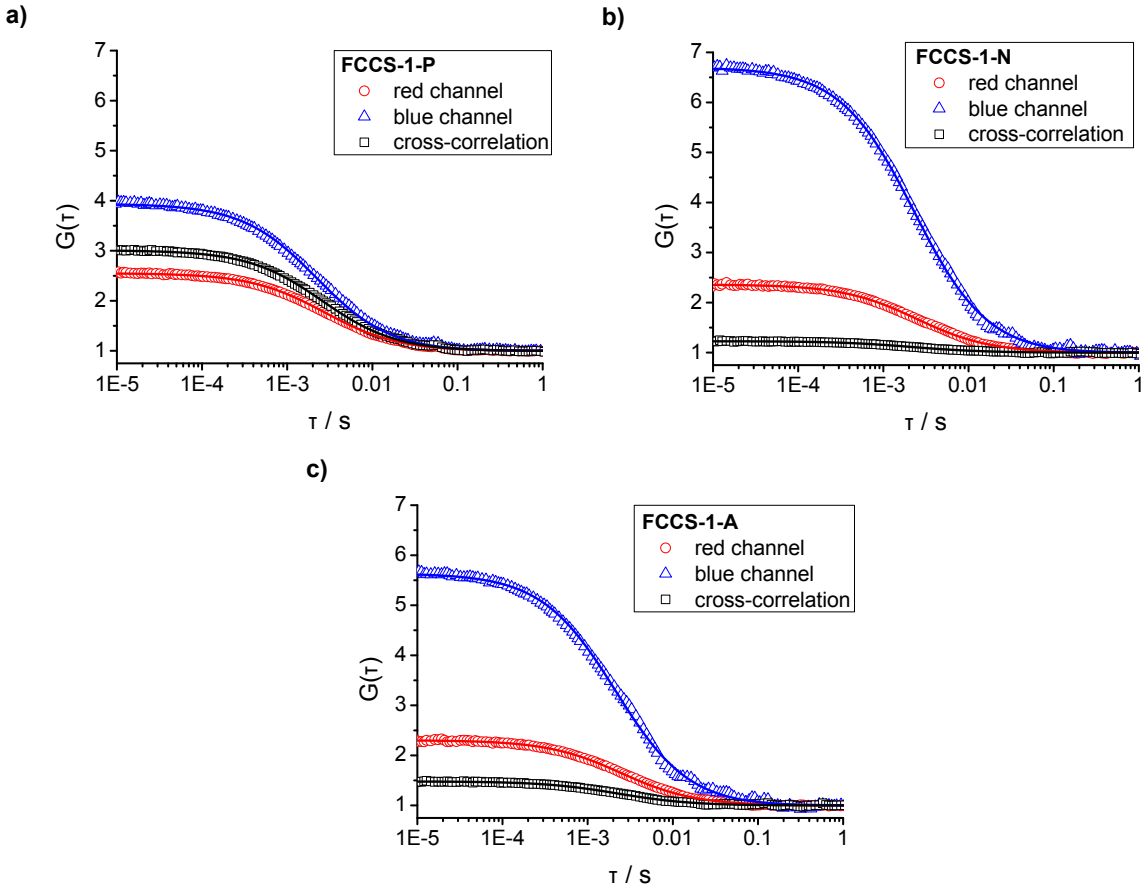

Figure 5.6: Correlation curves (scattered symbols) and corresponding fits (lines) of the DC-FCCS samples FCCS-1-P (a), FCCS-1-N (b), and FCCS-1-A (c).

In another set of experiments, the amount of polymer in the chloroform was reduced by a factor of ten (FCCS-3). As expected, the obtained nanoparticles displayed smaller size than the nanoparticles formed from more concentrated polymer solutions (Table 5.1). In this case, the amount of double labeling was (11.4 ± 6.5) % (Table 5.4, Figure 5.7b). This corresponds to (24.4 ± 13.9) % of the original droplets having coalesced during the solvent evaporation, which yields an A value of (1.14 ± 0.09). The higher measured value for the magnitude of coalescence is the

result of the larger initial content of solvent in the droplets. Indeed, the probability of coalescence between droplets is increased by the lowering of the viscosity of the dispersed phase and by the longer evaporation time.

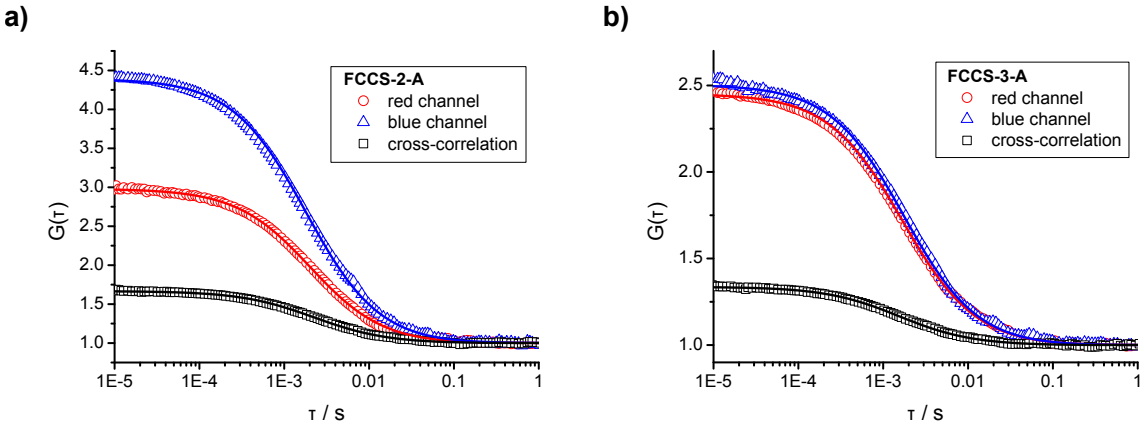

Figure 5.7: Correlation curves (scattered symbols) and corresponding fits (lines) of the DC-FCCS samples FCCS-2-A (a) and FCCS-3-A (b), which were prepared with toluene (a) or with chloroform with a low concentration of polymer in the droplets (b).

To assess the importance of coalescence in the broadness of the size distribution, simulations were carried out to determine if coalescence alone could be responsible for the observed large distribution in size of the nanoparticles. As it is difficult to measure the size distribution of the droplets for the aforementioned reasons, we modeled the original emulsion by reverse Monte Carlo simulations, based on the measured size distribution of the samples FCCS-1-A, FCCS-2-A, and FCCS-3-A. We tested the effect of a broad range of different probabilities of coalescence, from 5 to 50%, to check the influence of coalescence on the particle size distribution (Figure 5.8). The emulsions show an almost identical size distribution compared to the final nanoparticle dispersion at low degrees of coalescence, including the measured one. The peak position is shifted slightly to smaller diameters, but the overall shape remains, especially for larger droplet/particle sizes. This shows clearly that coalescence is not significantly responsible for the observed relatively broad size distribution. Although hexadecane is usually employed as a hydrophobic agent to prevent Ostwald ripening of the droplets in miniemulsion polymerization,[121] the polymer itself can act as a hydrophobe for particles produced by the emulsion solvent evaporation technique.[228] Indeed, it stabilizes the droplets kinetically, but not ther-

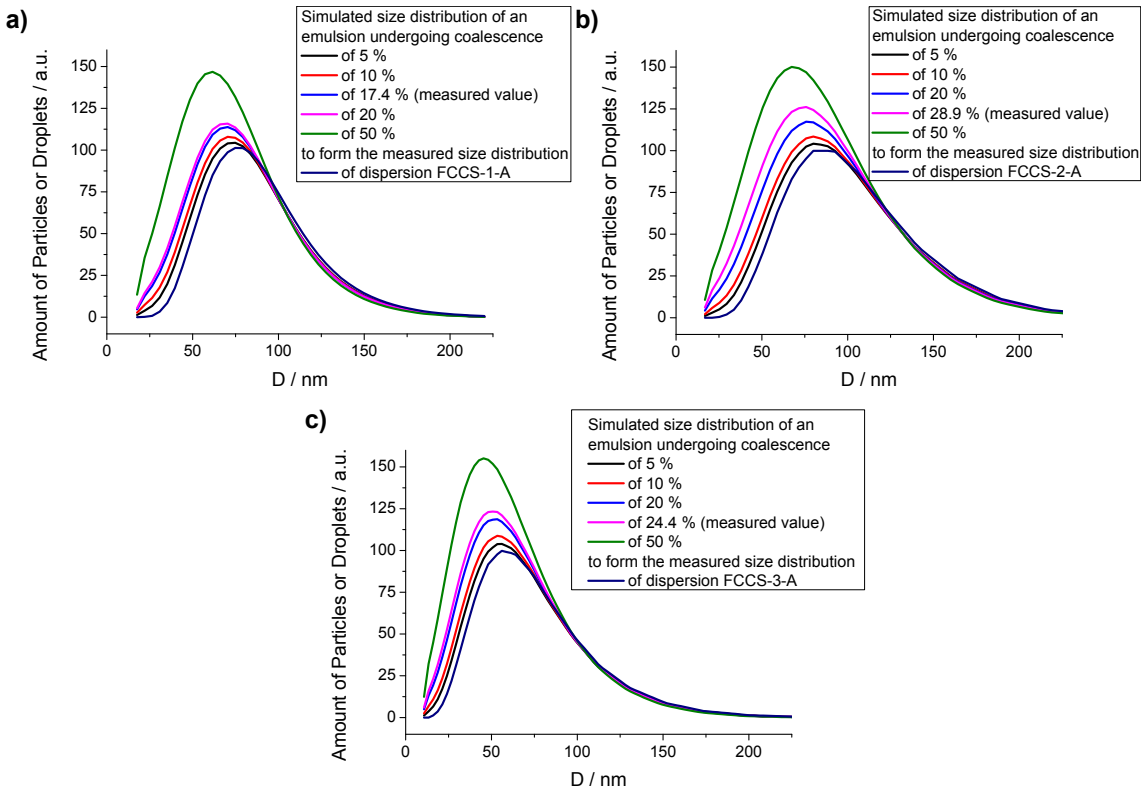

Figure 5.8: The distributions of hydrodynamic diameters of the nanoparticles measured by DLS were used to calculate the size distribution of the droplets in an emulsion by assuming different probabilities of coalescence below and above the measured value.

modynamically because the molar amount of polymer compared to solvent (1:62825) is not enough to completely counterbalance the Laplace pressure.[121] To exclude the influence of Ostwald ripening on the size distribution of the obtained nanoparticles, we prepared samples without (sample O-1) and with different amounts of hexadecane, thereby keeping constant either the total dispersed mass (sample O-2) or the total dispersed volume (sample O-3). After solvent evaporation, the hydrodynamic diameter and the particle size distribution were measured by DLS. In all cases, the size distribution was almost identical, slightly larger than 30 % (see Table 5.1), although the molar ratio of hexadecane/solvent was above the recommended ratio of 1:250,[121] that is, 1:162 and 1:119 for O-2 and O-3, respectively. This shows that there is no influence of Ostwald ripening on the particle size distribution during solvent evaporation or that the polymer is a very efficient hydrophobe. As coalescence was found not to be the cause of the observed particle size distribution, the

observed large polydispersity most likely originates from the emulsification process itself, which has to be improved.

5.3. Conclusion

DLS was found not to be suitable to study coalescence in our systems because the estimated diameters of the nanodroplets were influenced by the diluent and the dilution. Zeta potential and FCS measurements, respectively, showed that there is neither a change in the surface coverage of the nanodroplets nor a change in their concentration and fluorescence brightness during the solvent evaporation process. This points to an absence of coalescence. We used DC FCCS on a mixture of two polymeric emulsions, each of them containing polymer labeled with a different dye. This allowed quantification of the magnitude of coalescence, which was found to be insignificant. It cannot account for the observed particle size distribution. The DC FCCS measurements are supported by FRET measurements on labeled particles, which also show nearly no coalescence. The combination of techniques used in this study shows that the typical large size distribution of nanoparticles prepared by emulsion-solvent evaporation is very likely due to the process itself producing droplets with large size distribution. Thus, further efforts towards the fabrication of monodisperse nanoparticles by the emulsion-solvent evaporation method have to be continued in this direction.

5.4. Experimental Section

5.4.1. Materials

Polystyrene (PS, $M_w \approx 300000$ gmol^{-1}), polydispersity index ($PDI = 2.38$, Acros), sodium dodecyl sulfate (SDS, Alfa Aesar, 99%), N -(2,6-diisopropylphenyl)-perylene-3,4-dicarbonacidimide (PMI, BASF), toluene (Sigma-Aldrich, 99.7%), tetrahydrofuran (THF, Sigma-Aldrich, 99.9 %), methanol (Fluka, 99.99 %), dichloro-methane (Fluka, 99.99 %), chloroform (Acros, 99 %), and hexadecane (Merck, 99 %) were used as received. Styrene (Merck, 99 %) was purified on a column packed with neutral aluminum oxide (Merck) before use. The initiator 2,2'-azobis(2-methylpropionitrile) (AIBN, Fluka, 98%) was recrystallized from methanol prior to use. The synthesis

of the fluorescent dyes B504-MA and B612-MA (Figure 5.9a,b, SI) was based on syntheses reported in the literature.[1,197] Both dyes have already been employed for the synthesis of fluorescent nanoparticles[229–231] and nanogels.[232] The synthesis of the copolymers named PS-504 and PS-612 from B504-MA and B612-MA has been described before as well as their characterization by gel permeation chromatography (GPC) and high-performance liquid chromatography (HPLC)[34]. Most importantly, the absence of free dye in both copolymers was proven by HPLC.[34] The monomers 9-vinylphenanthrene (VPA, Toronto Research Chemicals) and [1-(4-nitrophenyl)-2-pyrrolidinmethyl] acrylate (NPP, Sigma-Aldrich) were selected (Figure 5.9c-d) because they have been used for FRET measurements before.[226,226] Distilled water was used throughout the work.

5.4.2. Synthesis of Labeled Polymers for FRET Measurements

Copolymers of styrene and VPA or NPP were prepared by free-radical polymerization in miniemulsion. To this end, AIBN (100 mg), hexadecane (250 mg), and styrene (6 g) were added to VPA (30 mg, PS-VPA) or NPP (60 mg, PS-NPP) to build the dispersed phase and were added subsequently to a solution of SDS (72 mg) in water (24 g). The mixture was emulsified for 1 h at 1250 rpm and submitted to ultrasonication for 2 min at 90 % amplitude under ice cooling. Afterwards, the polymerization was carried out in a closed 50 mL round-bottom flask at 72 °C for 12 h. The obtained dispersion was freeze-dried, dissolved in THF, and reprecipitated three times into methanol. The apparent molecular weights of the copolymers PS-VPA and PS-NPP were measured to be 650550 (PDI = 3.2) and 369600 gmol^{-1} (PDI = 3.3), respectively, as determined by GPC (Figure 5.10). The purity of the polymers was verified with HPLC by employing the free dye as reference. No free dye was detected in either copolymer after their purification (Figure 5.11). Absorption and emission measurements on the dyes and on the polymers showed that there were no significant changes in absorption or fluorescence of the dyes upon their copolymerization (Figure 5.12).

5.4.3. Preparation of the Nanoparticles

A certain amount of polymer (PS, PS-504, PS-612, PS-VPA, PS-NPP) was dissolved in solvent (2.5 g; Table 5.1, SI) and added to an aqueous solution of SDS (20 g, 1 gL^{-1}). A macroemulsion was obtained by stirring at 1250 rpm for 1 h. The macroemulsion was sonicated using a Branson W450-D sonifier with a 1/2-inch tip at 70 % amplitude in a pulsed regime (30 s sonication, 10 s pause) under ice cooling. The obtained emulsions were then either treated directly (see preparation of samples for DC FCCS, FRET, and DLS experiments below) or transferred into a 50 mL reaction flask and stirred at 500 rpm and 40 ℃ for 12 h. In the case of further treatment, the emulsions were transferred to the reaction flask directly after the treatment. Spherical nanoparticles were obtained as shown by the SEM images (Figures 5.13 and 5.14).

5.4.4. Preparation of Samples for DC-FCCS and FRET Experiments

Positive and negative control samples were prepared for comparison with the actual samples. For positive control samples (denoted "P"), the two labeled polymers were miniemulsified together (Table 5.1). Negative control samples (denoted "N") were prepared by mixing equal volumes of the differently labeled dispersions obtained after solvent evaporation. For the actual samples (denoted "A"), equal volumes of the differently labeled emulsions were combined directly after ultrasonication and before solvent evaporation. The description of the preparation of the three different kinds of samples is summarized and explained in Figure 5.4.

5.4.5. Analytical Tools

The synthesized polymers and particles were characterized with GPC, HPLC, electron microscopy, FCS, and absorption and fluorescence measurements (SI)). The hydrodynamic diameters of the nanoparticles were measured with a Nicomp 380 Submicron Particle Sizer (PSS-Nicomp) at an angle of 90 ° (DLS) for 300 s. The latexes (10 μL) were diluted in 1000 μL of either distilled water, an aqueous solution of SDS (1 gL^{-1}), distilled water saturated with a solvent (toluene, chloroform, dichloromethane), or distilled water saturated with a solvent (toluene, chloroform,

dichloromethane) and containing SDS (1 gL^{-1}). The averages of two independent measurements as well as their standard deviations were reported. The zeta potential of the emulsion droplets was measured at 25 ℃ in potassium chloride solution (10^{-3} $molL^{-1}$, 50 μL sample per 1000 μL diluent) with a Zetasizer ZEN2600 (Malvern Instruments). The average of at least ten runs is reported herein.

Decays of fluorescence were recorded with the time-correlated single photon counting technique (FluoTime 200, PicoQuant GmbH). A cuvette (thickness 10 mm) with a diluted dispersion was excited by light emitting source PLS 280 (spectral width < 20 nm, repetition rate 2 MHz, power 1 μW, and pulse duration ≈ 900 ps; PicoQuant GmbH). Right-angle geometry of detection was chosen for fluorescence collection. Glanâ€“Thompson polarizers (for excitation and detection) were arranged under magic angle conditions. An additional long-pass filter (Brightline 300/LP, Semrock Inc.) was placed in front of a Sciencetech Model 9030 monochromator for better separation of scattered light and fluorescence signal. A counting photomultiplier PMA 165 (PicoQuant GmbH) was used as detector.

FCS and DC FCCS experiments were performed on an inverted microscope Olympus IX70 combined with the FluoView300 confocal laser scanning unit (Olympus) fiber coupled to a PicoQuant FCS unit that included two separate avalanche photodiodes τ - SPAD (PicoQuant GmbH) and the respective emission filters. In the FCS experiments, the labeled nanoparticles were excited with an argon-ion laser at 488 nm, whereas emission was collected after filtering with an LP488R RazorEdge filter. In the DC FCCS experiments, argon-ion (488 nm) and helium-neon (633 nm) lasers were used simultaneously to excite the B504-MA and B612-MA dye-labeled polymers, respectively. The collected fluorescence was divided into two channels by a dichroic mirror and filtered further with an LP635 long-pass filter in channel 1 and BP525/50 band-pass filter in channel 2. Calibration of the confocal detection volumes was achieved by performing reference measurements with Alexa Fluor 488 and Alexa Fluor 647 dyes (both Invitrogen) using the reported values of their diffusion coefficients.[198] A more detailed description of the FCS setup and its working principle can be found in the literature[34] and in the SI.

To evaluate the effect of coalescence during evaporation on the size distribution of the precipitated nanoparticles, we set up a model to reconstruct the size distribution of the droplets in the emulsion. To this aim we implemented a reverse Monte Carlo procedure, which takes as input parameters the probability of coalescence

in solution. The process is assumed to occur in a single step and the number of coalescence events per particle is at most one. A minimum size of the particles in the emulsion, equivalent to the smallest particles detected in the precipitate, is set as a boundary condition, and particle diameters are rescaled according to the different density between nanodroplets in emulsions and precipitated nanoparticles. The reverse Monte Carlo loop is iterated a sufficient number of times to achieve a statistical uncertainty two decades smaller than the scale of the distributions.

5.5. Supporting Information

5.5.1. Materials and Amounts used

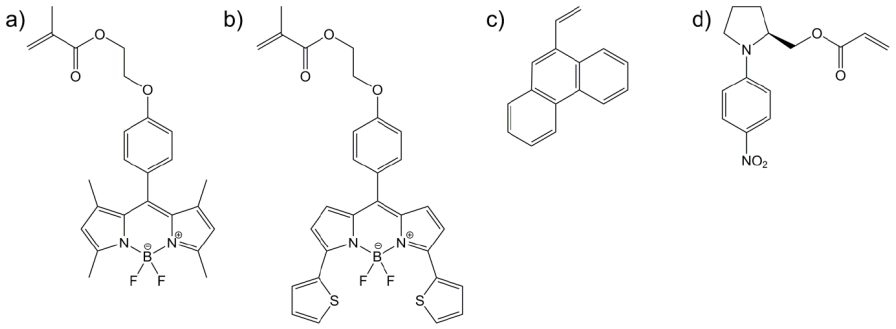

Figure 5.9: The polymerizable dyes B504-MA (a), B612-MA (b), 9-vinylphenanthrene (c) and [1-(4-nitrophenyl)-2-pyrrolidinmethyl] acrylate (d) were used to label polystyrene chains for DC-FCCS (a, b) and for FRET-experiments (c, d).

Table 5.1: Entry names, polymers and solvents used in the experiments. Starred entries are depending on diluent and dilution, see main document.

Entry	m(PS) [mg]	m(PS-504) [mg]	m(PS-612) [mg]	m(PS-VPA) [mg]	m(PS-NPP) [mg]	m(PMI) [mg]	m(HD) [mg]	Solvent	D [m]	σ [%]
Time	100	–	–	–	–	–	–	$CHCL_3$	*	*
Dil-1	100	–	–	–	–	–	–	$CHCL_3$	*	*
Dil-2	100	–	–	–	–	–	–	Toluene	*	*
Dil-3	100	–	–	–	–	–	–	CH_2CL_2	*	*
O-1	100	–	–	–	–	–	0	$CHCL_3$	141	31
O-2	60	–	–	–	–	–	40	$CHCL_3$	101	35
O-3	60	–	–	–	–	–	29.3	$CHCL_3$	97	32
FCS-1	100	–	–	–	–	0.01	–	$CHCL_3$	*	*
FCCS-1-PS-504**	–	100	–	–	–	–	–	$CHCL_3$	98	33
FCCS-1-PS-612**	–	–	100	–	–	–	–	$CHCL_3$	91	35
FCCS-1-P**	–	–	50	50	–	–	–	$CHCL_3$	96	34
FCCS-1-N**	–	–	–	–	–	–	–	–	95	31
FCCS-1-A**	–	–	–	–	–	–	–	–	92	35
FCCS-2-PS-504	–	100	–	–	–	–	–	Toluene	85	39
FCCS-2-PS-612	–	–	100	–	–	–	–	Toluene	83	37
FCCS-2-P	–	–	50	50	–	–	–	Toluene	87	33
FCCS-2-N	–	–	–	–	–	–	–	–	83	32
FCCS-2-A	–	–	–	–	–	–	–	–	83	38
FCCS-3-PS-504	–	10	–	–	–	–	–	$CHCL_3$	70	43
FCCS-3-PS-612	–	–	10	–	–	–	–	$CHCL_3$	68	44
FCCS-3-P	–	–	5	5	–	–	–	$CHCL_3$	69	31
FCCS-3-N	–	–	–	–	–	–	–	–	71	46
FCCS-3-A	–	–	–	–	–	–	–	–	72	44
FRET-PS-VPA	–	–	–	100	–	–	–	$CHCL_3$	124	35
FRET-PS-NPP	–	–	–	–	100	–	–	$CHCL_3$	114	28
FRET-PS-P	–	–	–	50	50	–	–	$CHCL_3$	123	27
FRET-PS-N	–	–	–	–	–	–	–	–	121	29
FRET-PS-A	–	–	–	–	–	–	–	–	120	25

*see text, depending on diluent and dilution

also see D. Schaeffel, R. H. Staff, H.-J. Butt, K. Landfester, D. Crespy, K. Koynov, *Nano Lett.* **2012, 12, 6012

5.5.2. Characterization methods

Gel permeation chromatography (GPC) was used to estimate the average molecular weights of the polymers and their polydispersity index (PDI). The dried polymers were dissolved in THF at a concentration of 5 mg·mL^{-1} and filtered through a 0.45 μm Teflon filter. An elution rate of 1.0 mL·min^{-1} and both UV- (254 nm) and RI-detectors were used. The apparent molecular weights of the polymers were calculated using polystyrene standards.

For PS-VPA and PS-NPP, HPLC measurements were conducted on the polymer and the free dye to check the absence of free dye in the polymer. The measurements were performed with a gradient of THF and water starting from a ratio of 50 to 50 up to 100 to 0 in 10 min. The flow was 1 mL·min^{-1} employing a RP8e-column (Merck)) on a 1200 HPLC from Agilent Technologies. For detection, a DAD-Detector at a wavelength of 310 nm for PS-VPA and at 380 nm for PS-NPP was used.

Absorption and fluorescence emission spectroscopy on the dyes and the polymers was done in $CHCl_3$ solutions at concentrations of 0.1 mg·mL^{-1} respectively 1 mg·mL^{-1} on a Tecan Plate Reader Infinite M1000. For the quantification of labeling, the fluorescence emission of a concentration series of both dyes was run. Obtained intensities were corrected for background and solvent.

For electron microscopy, 10 μL of the dispersions of the nanoparticles were diluted with 1 mL of distilled water. SEM-images were taken on a Zeiss 1530 Gemini Leo at varying voltages.

In the FCS experiments, the measured temporal fluctuations of the fluorescence intensity $\delta F(t)$, were evaluated through an autocorrelation function defined as:

$$G(\tau) = 1 + \frac{\langle \delta F(t) \delta F(t+\tau) \rangle}{\langle F(t) \rangle^2} \tag{5.4}$$

As theoretically shown in the case of an ensemble of identical, freely diffusing fluorescent species, this autocorrelation function has the following analytical form[18]:

$$G(\tau) = 1 + \frac{1}{N} \left(1 + \frac{\tau}{\tau_D}\right)^{-1} \left(1 + \frac{\tau}{S^2 \tau_D}\right)^{-\frac{1}{2}} \tag{5.5}$$

Here, N represents the average number of the fluorescent species in the confocal observation volume V, τ_D is their average lateral diffusion time through V, and $S =$

z_0/r_0 is the ratio of the axial to lateral dimension of V ($S \approx 6$ in our experiments). The experimental correlation curves (eq. 5.4) were fitted with eq. 5.5, yielding N and τ_D. Consequently, the concentration $C = N/V$ of the diffusing species and their fluorescent brightness $\langle \delta F(t) \rangle / N$ were evaluated. In the case of fluorescently labeled nanodroplets considered here, the latter parameter is proportional to the number of labeled polymer chains per droplet and should increase upon coalescence. Furthermore, the diffusion coefficient D and the hydrodynamic radius R_h of the species were evaluated from the relation $D = (r_0^2 + R_h^2)/4\tau_D$, and the Stokes-Einstein-relationship.[18]

In DC FCCS experiments, the beams of two lasers emitting at wavelengths of 488 nm and 633 nm respectively, were made collinear and focused to diffraction limited spots in the sample by a high numerical aperture, achromatic microscope objective. The fluorescent light was collected by the same objective and directed into two separate detection channels by a dichroic mirror. Each channel contained an emission filter, confocal pinhole and single photon counting avalanche photodiode detector. These arrangements resulted in the formation of two perfectly overlapping confocal observation volumes V_1 and V_2 that superimpose to a common observation volume V_{12}.[64] The temporal fluorescence fluctuations monitored in channel 1, $\delta F_1(t)$, and 2, $\delta F_2(t)$, were independently recorded and the cross-correlation function

$$G_{12}(\tau) = \frac{\langle \delta F_1(t) \delta F_2(t+\tau) \rangle}{\langle F_1(t) \rangle \langle F_2(t) \rangle} \tag{5.6}$$

was evaluated.[21] In addition, the autocorrelation functions from both channels were obtained. Therefrom, the average concentration of the double labeled species C_{12} was computed through $C_{12} = (C_{12}(0) - 1) N_1 N_2 V_{12} / V_1 V_2$. Furthermore, the sample FCCS-1-PS-504 was used to quantify the cross-talk. A bleed through factor of 0.021 was obtained, which means that 2.1 % of the fluorescence emitted by the dye B504-MA was detected also in channel 2, which was intended to detect the fluorescence of the B612-MA dye. All cross-correlation amplitudes were corrected accordingly for this cross-talk as described previously in other reports for other dyes.

5.5.3. Characterization data

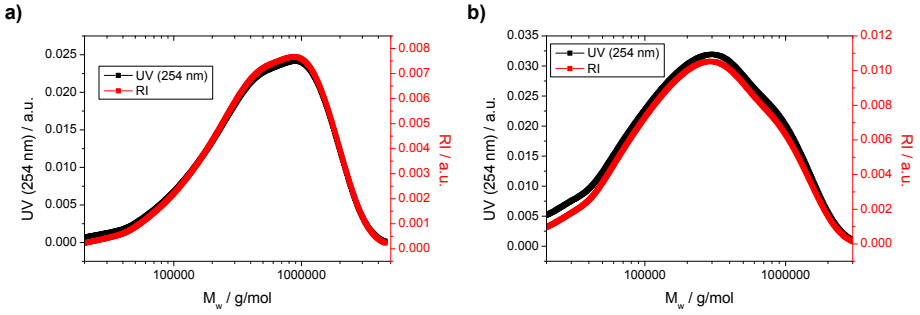

Figure 5.10: GPC traces of PS-VPA (a) and PS-NPP (b).

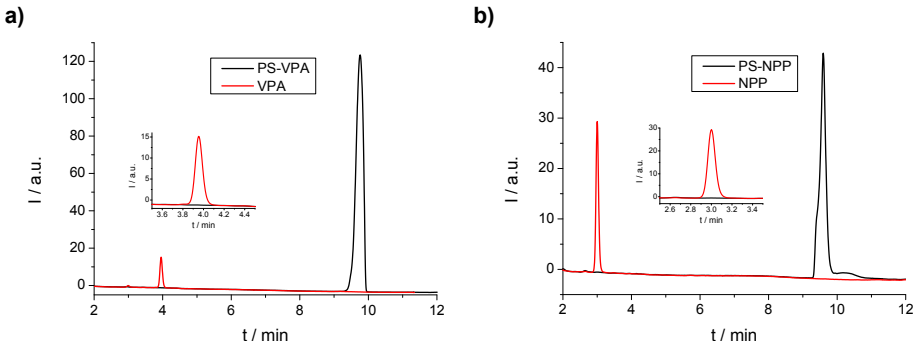

Figure 5.11: HPLC-plots for PS-VPA (a) and PS-NPP (b). Both inlays show that there is no free dye.

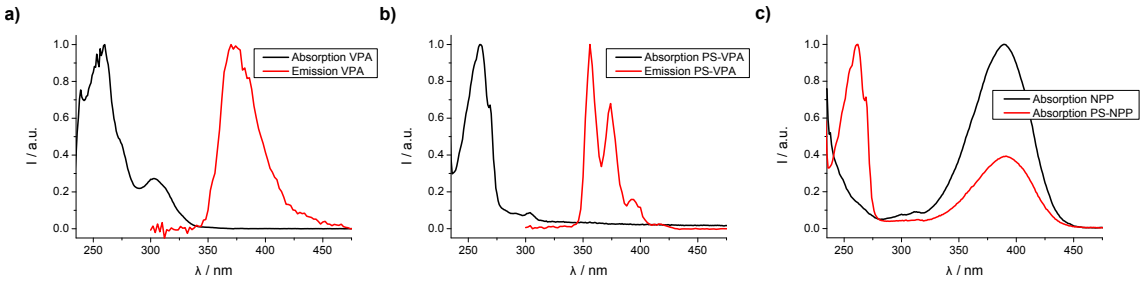

Figure 5.12: Absorption and emission spectra of VPA (a), PS-VPA (b) and the absorption spectra of NPP and PS-NPP (c). All spectra were corrected for background and solvent. NPP does not fluoresce.

5.5.4. SEM micrographs of the nanoparticles

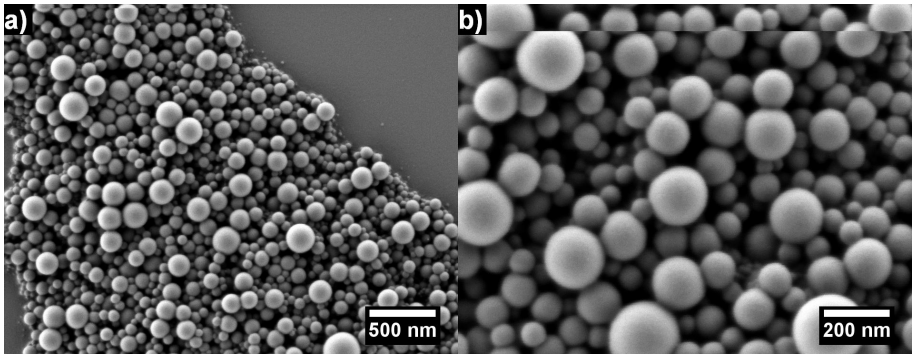

Figure 5.13: SEM micrographs of the sample "Time" at two different magnifications. Dense, spherical nanoparticles are obtained.

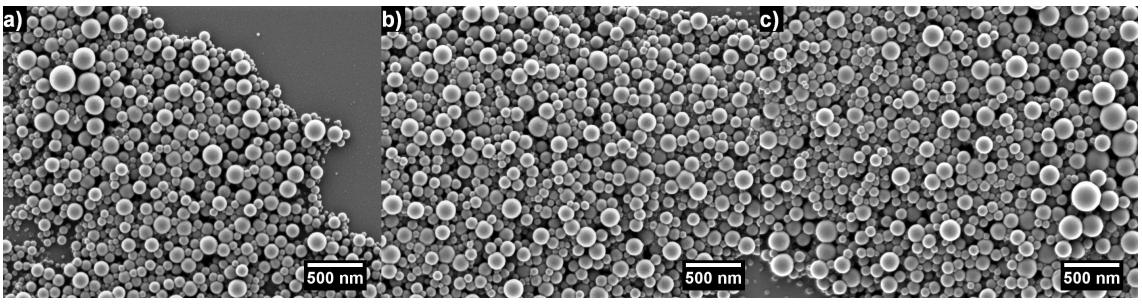

Figure 5.14: SEM micrographs of the samples Dil-1 (a), Dil-2 (b) and Dil-3(c).

5.5.5. DC FCCS data

Table 5.2: The channel numbers, concentrations (c) and hydrodynamic radii (r_H) for the dual color FCCS experiments performed with samples FCCS-1-P, FCCS-1-N and FCCS-1-A are shown.

Sample	Channel	$c \pm \Delta c$ [nM]	$r_H \pm \Delta r_H$ [nm]
FCCS-1-P	Ch.1/AC1 "red"	1.70 ± 0.52	51.3 ± 4.0
	Ch.2/AC2 "blue"	1.75 ± 0.21	49.6 ± 5.8
	CC	1.71 ± 1.19	52.5 ± 5.2
FCCS-1-A	Ch.1/AC1 "red"	2.02 ± 0.62	46.8 ± 3.8
	Ch.2/AC2 "blue"	1.11 ± 0.13	47.6 ± 5.8
	CC	0.23 ± 0.16	46.5 ± 6.9
FCCS-1-N	Ch.1/AC1 "red"	1.94 ± 0.60	46.3 ± 3.7
	Ch.2/AC2 "blue"	0.91 ± 0.11	51.1 ± 5.7
	CC	0.03 ± 0.02	44.4 ± 9.0

Table 5.3: The channel numbers, concentrations (c) and hydrodynamic radii (r_H) for the dual color FCCS experiments performed with samples FCCS-2-P, FCCS-2-N and FCCS-2-A are shown.

Sample	Channel	$c \pm \Delta c$ [nM]	$r_H \pm \Delta r_H$ [nm]
FCCS-2-P	Ch.1/AC1 "red"	2.11 ± 0.16	36.9 ± 2.3
	Ch.2/AC2 "blue"	2.55 ± 0.36	33.9 ± 2.4
	CC	2.15 ± 0.77	37.9 ± 2.5
FCCS-2-A	Ch.1/AC1 "red"	1.95 ± 0.15	32.9 ± 2.0
	Ch.2/AC2 "blue"	1.48 ± 0.21	39.3 ± 2.8
	CC	0.43 ± 0.15	41.5 ± 3.2
FCCS-2-N	Ch.1/AC1 "red"	1.32 ± 0.10	39.3 ± 2.7
	Ch.2/AC2 "blue"	1.61 ± 0.22	39.3 ± 2.8
	CC	0.09 ± 0.03	48.8 ± 8.8

Table 5.4: The channel numbers, concentrations (c) and hydrodynamic radii (r_H) for the dual color FCCS experiments performed with samples FCCS-3-P, FCCS-3-N and FCCS-3-A are shown.

Sample	Channel	$c \pm \Delta c$ [nM]	$r_H \pm \Delta r_H$ [nm]
FCCS-3-P	Ch.1/AC1 "red"	4.51 ± 0.95	26.0 ± 2.4
	Ch.2/AC2 "blue"	3.78 ± 0.48	27.5 ± 3.0
	CC	2.23 ± 1.17	31.3 ± 2.5
FCCS-3-A	Ch.1/AC1 "red"	2.02 ± 0.42	29.2 ± 2.0
	Ch.2/AC2 "blue"	3.39 ± 0.35	38.9 ± 2.8
	CC	0.55 ± 0.28	30.2 ± 2.6
FCCS-3-N	Ch.1/AC1 "red"	1.32 ± 0.27	24.1 ± 1.7
	Ch.2/AC2 "blue"	1.62 ± 0.17	33.4 ± 2.7
	CC	0.30 ± 0.15	26.7 ± 2.4

5.6. Acknowledgment

We would like to thank Sandra Seywald for the GPC characterization, Beate Müller for the HPLC measurements, Niklas Kotmann for helping with the quantification of the polymer labeling, and Robert Heinze for helping with the DLS measurements. R.H.S. gratefully acknowledges financial support by the Fonds der Chemische Industrie (FCI). The financial support from DFG (Grant No. KO3747/3-1) is also gratefully acknowledged.

6. Molecular Exchange Kinetics of Diblock Copolymer Micelles monitored by FCS

We investigated the equilibrium chain-exchange kinetics of amphiphilic diblock copolymer micelles, using a new method based on fluorescence correlation spectroscopy. The micelles were formed from polystyrene-*block*-poly[oligo(ethylene glycol) methyl ether methacrylate] (PS-POEGMA) in different solvents and studied at various temperatures. This linear-brush copolymer was chosen as a model system forming micelles with short and bulky corona. Depending on the applied solvent, fast exchange could be observed even at temperatures well below the nominal glass transition of the core forming PS block. The effect is caused by swelling of the core and allows extensive tuning of the chain-exchange rate by adding to the system minor amounts of good or bad solvent for the core block.

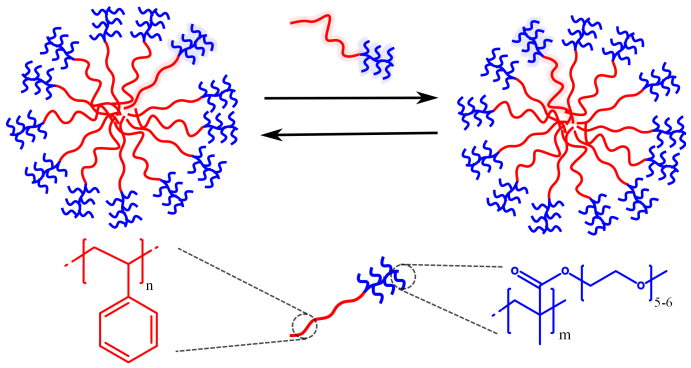

Reproduced with permission from:
D. Schaeffel, A. Kreyes, Y. Zhao, K. Landfester, H.-J. Butt, D. Crespy, K. Koynov: Molecular Exchange Kinetics of Diblock Copolymer Micelles monitored by Fluorescence Correlation Spectroscopy, *ACS Macro Lett.*, **2014**, *3*, 428-432.

6.1. Introduction

Amphiphilic block copolymers tend to self-assemble in aqueous solutions and form supramolecular structures like micelles or vesicles. In addition to numerous further applications, such self-assemblies are considered among the most promising candidates for drug carrier systems. In particular, block copolymer micelles with functional, non-immunogenic hydrophilic corona and hydrophobic core that can accommodate hydrophobic drugs have attracted growing interest.[39,40] Recently, the first polymeric micelles based drug carrier systems have entered clinical trials.[41] In order to further develop, tune and optimize such carriers with respect to drug loading capacity, stability, long circulation times and controlled release it is of paramount importance to have a good knowledge on the physical processes governing the formation, the structure and the kinetic stability of block copolymer micelles. However, while the static properties of block copolymer micelles have been extensively studied and are relatively well understood,[233–235] much less is known for their dynamic behavior, in particular for the process of chains exchange between micelles in equilibrium. Yet, such an exchange may have important effects on the micelles drug carrier properties e.g. on their loading capacity, stability, and controlled release.

The chain exchange between block copolymer micelles at equilibrium was studied theoretically by Halperin and Alexander.[37] They derived an analytical model predicting that the exchange of individual chains through expulsion-insertion is the dominating mechanism and eventual fission and fusion of polymer aggregates (micelles or "submicelles") plays only a secondary role. This result was further confirmed by dissipative particle dynamics simulations performed by Li and Dormidontova.[236] On the other hand, experimental studies are relatively rare and the number of investigated block copolymer micelle systems remains extremely limited. The main reason is the lack of appropriate, easily accessible experimental techniques. Indeed, while methods based on fluorescence quenching,[42] sedimentation,[237] or cryo-TEM[43] have been used to study the exchange kinetics, to date the most important, quantitative results that could be compared with the theoretical predictions were obtained by time-resolved small-angle neutron scattering (TR-SANS) experiments performed by Richter and coworkers,[44,161,238–240] and Bates, Lodge and coworkers[45,241–243]. Clearly, the availability of new methods based on broadly accessible tabletop equipment shall boost the related studies and help to improve our

understanding in this important field.

Fluorescence correlation spectroscopy (FCS) is a sensitive and selective method for investigating the mobility of fluorescent species, such as small molecules, macromolecules, or nanoparticles in various environments.[64] In a typical FCS experiment, the temporal fluorescence intensity fluctuations caused by e.g. the diffusion of the studied fluorescent species through a small observation volume are monitored and used to evaluate their diffusion coefficient, size, and concentration.[64] While initially developed and still predominantly used in molecular and cell biology,[8,9] FCS was also established as a powerful tool in polymer, colloid, and interface science.[10,11] Furthermore, it was already successfully used to study amphiphilic block copolymer based supramolecular structures. For example Papadakis and coworkers applied FCS to study the formation of block copolymer micelles and investigate the effect of polymer architecture on the size and critical micelle concentration (CMC) of the micelles.[15,17] The formation of block copolymer vesicles, their loading with drugs, and the process of nanoparticles uptake by such vesicles were also studied by FCS.[13,147,244]

In this letter, we present a new method for studying the dynamic equilibrium chain-exchange between polymer micelles. The method is based on a variation of the classical FCS technique, called dual color fluorescence cross-correlation spectroscopy (DC FCCS).[73] Compared to TR-SANS, DC FCCS uses tabletop equipment and fluorescent labeling that makes it more easily accessible and applicable to broad range of supramolecular structures. We apply this method to monitor the chain-exchange between polystyrene-*block*-poly[oligo(ethylene glycol) methyl ether methacrylate] (PS-POEGMA) micelles and to investigate the effect of temperature and solvent quality on its rate.

The linear-brush block copolymer PS-POEGMA was chosen for two reasons. First, it represents a model system for a micelle forming copolymer with short and bulky corona block. The chain exchange between such types of micelles was never studied before. Second, PS-POEGMA is also a model functional polymer because of the very interesting properties displayed by the POEGMA block. Indeed, polymers of OEGMA are thermoresponsive in water, were found to display an anti-fouling behavior below their lower critical solution temperature, and to have no specific interactions with biomolecules, which make them ideal for biomedical applications *e.g.* drug delivery.[245]

6.2. Experimental section

6.2.1. Synthesis and characterization

The PS-POEGMA copolymers were synthesized by atom transfer radical polymerization (Supporting Information (SI)). The degree of polymerizations of the hydrophobic PS and the hydrophilic POEGMA blocks were $N_{PS} \approx 47$ and $N_{POEGMA} \approx 10$, respectively. The polydispersity index of the PS block was PDI $= M_w/M_n = 1.18$ as measured by gel permeation chromatography (GPC). Thus, we expect that the micelles formed by the PS-POEGMA copolymer in polar media should have a rather dense and relatively thin corona. To enable DC FCCS studies part of the copolymers were labeled either "blue" or "red" by covalent attachment of "blue" or "red" fluorescent BODIPY dyes with a Diels-Alder reaction at the PS block (see SI). The labeled copolymers were mixed with unlabeled ones in a weight ratio of 5:95. The mixture was dissolved in THF that is a good solvent for both blocks. Dispersions of "blue" or "red" micelles were obtained by stirring the copolymer THF solutions while dropping a selective solvent (water or methanol) for 40 min. This process was followed by an immediate quenching with an excess of the selective solvent. The micelle solutions were dialyzed for three days in order to remove the THF.

The formation of micellar structures was confirmed by measuring the hydrodynamic radius of the diffusing fluorescent species in the selective solvent solutions at different copolymer concentrations ranging from 0.01 to 4 μM using classical FCS as described in the SI.[15,17] In methanol, at very low concentrations only single chains with $R_H \approx 2$ nm were observed. However at higher concentrations significantly larger species representing the formed micelles were recognized (Figure 6.5). This allowed determination of the CMC of 0.04 μM in methanol. In water the CMC was below 0.01 μM. Thus all further experiments were conducted at 4 μM polymer concentration, *i.e.* well above the CMC. The hydrodynamic radii of the micelles were determined to be $R_H = (13 \pm 2)$ nm in methanol and $R_H = (21 \pm 2)$ nm in water. Neither R_H, nor the CMC of the micelles were affected by the type of the label i.e. "blue" or "red", confirming that the labeling has minor or no effect on the properties of the formed micelles. This is not surprising in view of the small size of the fluorescent labels and the fact that only 5 % of the block copolymers were labeled.

6.2.2. Dual color Fluorescence Cross Correlation Spectroscopy

In order to investigate the chain exchange kinetics, independently prepared dispersions of "blue" and "red" labeled PS-POEGMA micelles were mixed at 1:1 ratio. The relative concentration of the double colored micelles that appeared as a result of chain exchange was measured as a function of time using DC FCCS. Detailed descriptions of the DC FCCS method and our experimental setup, which is based on a commercial FCS apparatus (Olympus and Pico Quant) is given elsewhere.[34] Briefly,

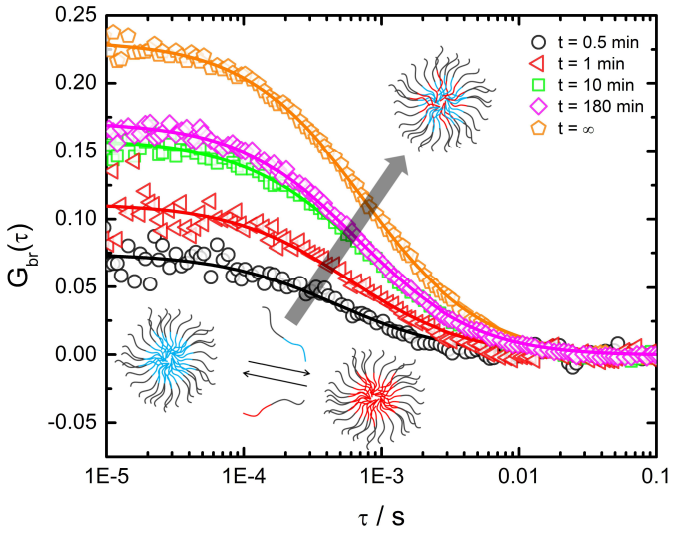

Figure 6.1: Cross correlation curves measured at 23 °C in methanol at different times. The figure delineates that with progressing time the cross correlation amplitude rises revealing an increase in the fraction of dual-colored micelles.

two collinear laser beams with different wavelengths ("blue" and "red" for simplicity) are coupled to a confocal microscope and used to create sub-femtoliter probing volumes V_b and V_r into the studied micellar solution. Ideally, these volumes are perfectly overlapping to create an efficient observation volume V_{br}.[34] The temporal fluctuations of the "red" and "blue" fluorescence signals $\delta F_b(t)$ and $\delta F_r(t)$ caused by the diffusion of fluorescent species through V_{br} were independently measured and analyzed by a cross-correlation function[73]:

$$G_{br}(\tau) = \frac{\langle \delta F_b(t) \delta F_r(t+\tau) \rangle}{\langle F_b(t) \rangle \langle F_r(t) \rangle} \tag{6.1}$$

The amplitude of this function, $G_{\mathrm{br}}(0)$, is directly proportional to the concentration of dual-colored species in the studied solution. Thus, if the fraction of dual-colored micelles increases with time $G_{\mathrm{br}}(0)$ should also rise. This is illustrated in figure 6.1 which shows experimental cross-correlation curves measured for a mixture of "red" and "blue" labeled PS-PEOGMA in methanol at T = 23 ℃ at different times after mixing. Furthermore, in addition to the cross-correlation function $G_{\mathrm{br}}(\tau)$, two autocorrelation functions $G_{\mathrm{bb}}(\tau)$ and $G_{\mathrm{rr}}(\tau)$ can be defined using equations analogous to Eq. 6.1. By fitting experimental auto- and cross-correlation functions with an analytical model for freely diffusing species[64] the hydrodynamic radii and the concentrations of single and dual-colored micelles can be evaluated.[34,64] In particular the concentration of dual-colored micelles is given by $C_{\mathrm{br}} = \frac{(G_{\mathrm{br}}(0)-1)V_{\mathrm{br}}}{(G_{\mathrm{bb}}(0)-1)V_{\mathrm{b}}G_{\mathrm{rr}}(0)-1)V_{\mathrm{r}})}$ and their relative fraction is $f_{\mathrm{br}} = \frac{C_{\mathrm{br}}}{C_{\mathrm{b}}+C_{\mathrm{r}}-C_{\mathrm{br}}}$. Finally, with the purpose of describing the exchange of polymers between the micelles and thus the transition of single-colored micelles to dual-colored ones in terms of a relaxation process similar to that used in TR-SANS experiments,[44,45] we define the experimental relaxation function as:

$$R_{\mathrm{exp.}}(t) = \frac{f_{\mathrm{br}}(\infty) - f_{\mathrm{br}}(t)}{f_{\mathrm{br}}(\infty) - f_{\mathrm{br}}(0)}. \tag{6.2}$$

6.3. Results and Discussion

6.3.1. Modeling the molecular exchange

Figure 6.2 (upper inset) shows typical relaxation functions $R_{\mathrm{exp.}}(t)$ measured for PS-POEGMA micelles in methanol at temperatures of 9 ℃, 12 ℃, 17 ℃ and 23 ℃. An almost logarithmic time dependence of $R_{\mathrm{exp.}}(t)$ was observed, a result that agrees with earlier TR-SANS findings for star shaped micelles.[44,45] This similarity is significant given the fact that the block copolymers studied here have a short and bulky corona blocks and thus are expected to form thin corona micelles. The relaxation curves (Figure 2) display a trend to faster decay, *i.e.* faster exchange kinetics, at higher temperatures. As shown by Choi *et al.*[45] this effect is related to the temperature dependence of the chain relaxations of the PS blocks forming the micelles cores. The time temperature superposition principle often used *e.g.* for rheological data can be applied in order to create a "master curve". Such a master curve was constructed by horizontally shifting the relaxation curves measured at

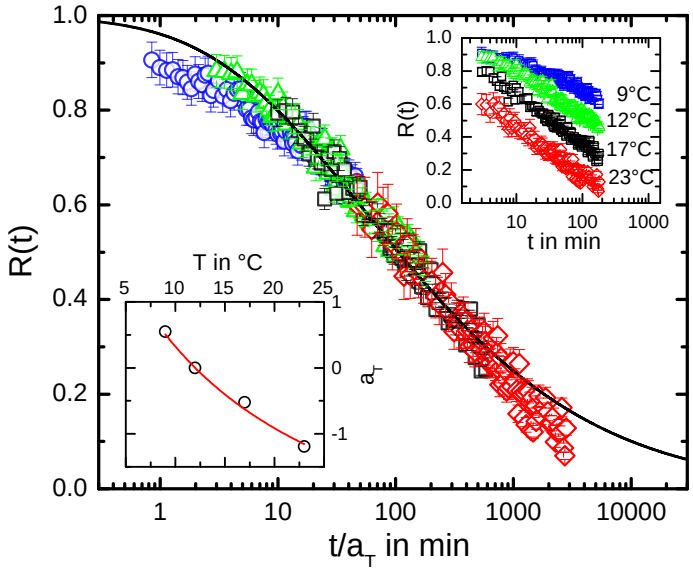

Figure 6.2: Relaxation functions of the chain exchange kinetics of PS-POEGMA micelles in methanol as measured with DC FCCS. A master curve is constructed by horizontal shifting of the individual relaxation functions measured at different temperatures (upper inset) to the reference temperature $T_{\mathbf{ref}}$ = 12 °C. The lower inset demonstrates that the temperature dependence of the shift factors follows the WLF equation. The solid line in the main figure represents a fit with eqs.(6.3)-(6.5)(see text for details).

9 °C, 17 °C and 23 °C with respect to the curve measured at 12 °C (Figure 6.2). The results could be nicely superimposed and the temperature dependence of the corresponding shift factors (lower inset in Figure 6.2) followed the classical Williams-Landel-Ferry (WLF) equation.[20]

Next, we compared our results with existing theoretical models in order to confirm their validity with respect to FCS based experiments and obtain quantitative information on the relevant parameters for the studied PS-POEGMA micelles. As discussed above, there is an agreement[37,38,44,45,161,238–243] that the exchange of individual copolymer chains between micelles is the major relaxation mechanism. Fusion or fission processes have only little influence. Under this assumption, the chain exchange kinetics is almost solely governed by the expulsion of the block forming the core (PS in our case) from the micellar core through the corona into the solvent.[37,38]

A time correlation function for the copolymer exchange can be defined as:[44,45]

$$K(t, N_{\mathrm{Core}}) = \exp\left[-\frac{t}{\tau}\exp\left(\frac{-A\gamma V_{\mathrm{m}}^{2/3} N_{\mathrm{Core}}^{\beta}}{kT}\right)\right] \tag{6.3}$$

here k is the Boltzmann constant, T is the temperature, τ - the characteristic relaxation time, γ the interfacial tension between core forming polymer and solvent, and N_{Core} and V_{m} degree of polymerization and monomeric volume of the core forming polymer, respectively. A and β are parameters, which describe the conformation of the core polymer during the expulsion process as discussed below. The polydispersity of the core forming block plays an important role[45] and was taken into account by convolving Eq. 6.3 with a Schulz-Zimm distribution:

$$P(N_{\mathrm{Core}}) = \frac{\xi^{\xi+1}}{\Gamma(\xi+1)} \frac{N_{\mathrm{Core}}^{\xi-1}}{\langle N_{\mathrm{Core}}\rangle^{\xi}} \exp\left(\frac{-\xi N_{\mathrm{Core}}}{\langle N_{\mathrm{Core}}\rangle}\right) \tag{6.4}$$

where $\xi = 1/(\mathrm{PDI} - 1)$, to finally obtain a relaxation function that has the form:

$$R(t, N_{\mathrm{Core}}) = \int_1^{\infty} K(t, N_{\mathrm{Core}}) P(N_{\mathrm{Core}}) dN_{\mathrm{Core}}. \tag{6.5}$$

We used equations (6.3)-(6.5) to fit the experimental results (Figure 6.2). Not all parameters need to be varied and many of them may be estimated from independent measurements or by using simple considerations. For example, the polydispersity of the core block and hence the parameter ξ were determined with GPC (SI). The second exponent in Eq. 6.3, $A\gamma V_{\mathrm{m}}^{2/3} N_{\mathrm{Core}}^{\beta}$, represents the activation energy in terms of creation of new interfacial area between core polymer and solvent after expulsion. We estimated the interfacial tension between PS and methanol from the extended Fowkes equation[246,247] to be $\gamma \approx 7.5$ mN/m. The parameters A and β describe the conformation of the core's blocks. For a totally collapsed, solvent free, globular conformation, A should be $(36\pi)^{1/3}$ and $\beta = 2/3$. For completely stretched chains, $A = (8\pi)^{1/3}$ with $\beta = 1$.[44,161] Since the number of repeat units of the core's block of our micelles is relatively low ($N_{\mathrm{PS}} \approx 47$) and a dense corona is formed by the short bulky POEGMA blocks, a stretched polymer conformation of the PS during the expulsion process and thus $\beta = 1$ can be expected.[45,241,242] Furthermore, leaving β free to vary between 2/3 and 1, when fitting our experimental data, always resulted

in $\beta \approx 1$. Therefore, to reduce the number of fit-parameters we fixed $\beta = 1$ and used only A as a fit parameter describing the conformation of the core forming chains. In addition, any further change of the activation energy, e.g. due to the penetration of solvent into the micelle core can also be accounted via the parameter A.

The last unknown parameter describing the relaxation function (Eq. 6.3) is the characteristic time τ. Since the PS blocks of our micelles are short, the micelle core can be considered as an unentangled and partially swollen polymer melt. We followed Choi *et al.*[45] and chose the Rouse time τ_R as the characteristic time of the process. Thus $\tau = \tau_R = N_{Core}^2 b^2 \zeta/(6\pi^2 kT)$ with b and ζ the monomer segment length and monomeric friction, respectively.

The value of $b = 0.67$ nm is known from literature reports[45,248] and was used as a fixed parameter. However, there are no available data for the monomeric friction coefficient ζ, e.g. from rheological measurements, because the PS was probably swollen to an unknown extent by methanol. Therefore, we used the monomeric friction coefficient ζ as a second fit parameter. Moreover, in order to account for the temperature dependence of ζ, we used equations (6.3)-(6.5) to fit directly the "master curve" of experimental data (Figure 6.2). Therefore, our fit results correspond to the reference temperature $T_{ref} = 12$ °C. This approach fitted the experimental data reasonably well (Figure 6.2, solid line) and yielded $A = 1.25 \pm 0.01$ and $\zeta = (105 \pm 5) \cdot 10^{-5}$ Ns/m. This value of ζ is similar to that obtained by rheology for bulk non-entangled PS slightly above its glass transition.[248] As the master curve is constructed for a reference temperature of 12 °C, we estimated that the glass transition of the micelle's core should be around 5-8 °C. Although the low molecular weight of the PS chains implies a T_g of about 75 °C for this polymer,[248] only an additional swelling of the PS core with the surrounding methanol can explain the strong reduction of T_g. Here the possibility that a small amount of remaining THF is causing the core swelling can be ruled out since no chain exchange was observed for micelles formed in water as discussed below (inset Figure 6.3). The fact that the fit produced a value of $A = 1.25$, which is lower than $A = (8\pi)^{1/3} \approx 2.93$ expected for stretched PS chains, further indicates that the methanol has penetrated into the micelle's core and lowered the energy required for the polymer expulsion. As the exact extent of the core's swelling cannot be determined accurately, we roughly estimated it by applying the Fox-equation.[20] Using the value of ≈ -98 °C for the glass transition of methanol and ≈ 75 °C for PS we calculated that the cores of our

PS-POEGMA micelles are swollen with roughly 25 wt% methanol.

6.3.2. Solvent dependency on the exchange kinetics

To examine further the effect of solvent on the chain-exchange kinetics, we studied micelles formed in methanol mixed with either 5 vol% of water that is a bad solvent for the PS core, or 3 vol% of THF as a good solvent for the PS core (Figure 6.3). For the methanol-THF mixture the relaxation accelerates, indicating that the chain dynamics inside the PS micelle's core becomes faster and the energy required for chain expulsion decreases. The opposite is observed for the methanol-water mixture.

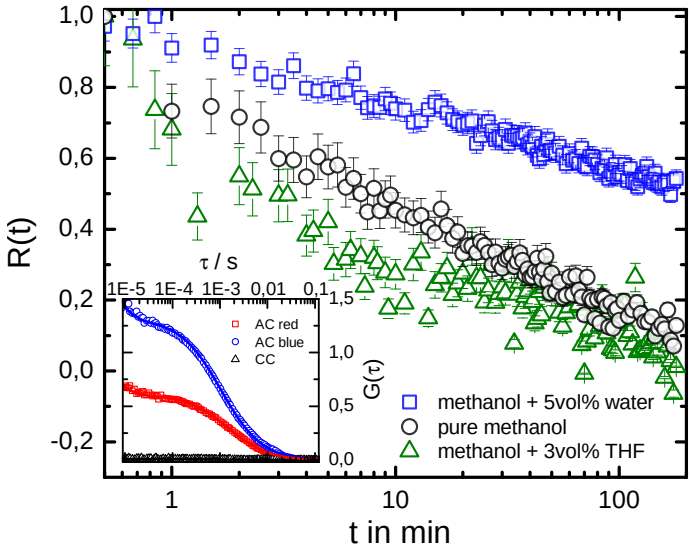

Figure 6.3: Relaxation curves of the exchange kinetics in methanol, methanol-water and methanol-THF mixtures at 23 °C. The inset shows the auto- and cross-correlation curves of the micelles in water after several weeks. The amplitude of te cross correlation is practically zero, showing that there is no exchange between micelles in pure water at this temperature.

The relaxation process slows down, suggesting an increased expulsion energy and slower dynamics inside the PS micelle's core. These findings demonstrate the major role that the solvent quality and the eventual core swelling have on the exchange dynamics. The later process is especially important as it allows chain exchange at temperatures below the glass transition of the core block. In the absence of core swelling the chain exchange dynamics of the studied PS-PEOGMA copolymer

micelles is basically frozen at such temperatures. This is illustrated in the inset in Figure 6.3 that shows the auto- and cross-correlation curves measured a month after mixing "blue" and "red" labeled micelles formed in pure water and kept at 23 ℃. The amplitude of the cross-correlation is practically zero, showing that there was no chain exchange between the micelles even after this extended period of time.

6.4. Conclusion

In summary, we have presented a new method for studying the chain exchange kinetics in diblock copolymer micelles by using dual color fluorescence cross-correlation spectroscopy (DC FCCS). This technique employs tabletop equipment and fluorescent labeling that makes it accessible to large research community and applicable to broad range of copolymer systems. We applied the new method to measure the exchange kinetics of micelles formed by a linear-brush copolymer PS-POEGMA, as a model system with short and bulky corona block. By varying the temperature and comparing the results with a scaling theory reported earlier,[37,38,45] we were able to quantify the extent of swelling of the PS micelle's core and explain the fast exchange that takes place at temperatures well below the nominal glass transition of PS. Furthermore, we showed that the addition of small amounts of either good or bad solvent for the PS core had a tremendous effect on the exchange kinetics.

6.5. Supporting Information

6.5.1. Fluorescence Correlation Spectroscopy

An inverted microscope, Olympus IX70 combined with a confocal laser scanning unit FluoView300 (Olympus), and a PicoQuant FCS upgrade comprising two single photon counting avalanche photodiodes (τ-SPAD) were used for the FCS and DC FCCS measurements. Dyes were excited with an argon-ion laser at $\lambda = 488$ nm or a helium-neon laser at $\lambda = 633$ nm. The fluorescence of the dyes where filtered with either a 500-550 nm band pass or an 690-710 nm band pass for DC FCCS measurements whereas for FCS measurements 488 nm long pass and 635 nm long pass emission filters were used respectively (all Semrock). Throughout all measurements an Olympus UPLSAPO 60XW 60x/1.2 water immersion objective was used.

As sample cell an eight-well, polystyrene-chambered cover glass (Nalge Nunc International) was used. Temperature control during experiments was achieved using a remotely controlled heating stage (Linkam Scientific Instruments). Reference measurements to obtain size and shape of the FCS observation volumes were conducted using dyes with well-known diffusion coefficients, in our case Alexa Fluor 488® and Alexa Fluor 647® (Invitrogen).[198] Occasional occurrence of aggregates was encountered by discarding concerned curves. Thus, all the curves used for analysis can be considered of being aggregate free. For DC FCCS for the here used fluorescent dyes the positive detector cross-talk was found to be negligible.

The autocorrelation in FCS is derived by the temporal fluorescence intensity fluctuations $\delta F(t)$:

$$G(\tau) = 1 + \frac{\langle \delta F(t) \delta F(t+\tau) \rangle}{\langle F(t) \rangle^2}. \tag{6.6}$$

It has been shown theoretically that for an ensemble of types of freely diffusing species the autocorrelation function follows the analytical form:[18]

$$G(\tau) = 1 + \frac{1}{\langle N \rangle} \sum_{\mathrm{i}=1}^{\mathrm{m}} \frac{f_{\mathrm{i}}}{\left(1 + \frac{\tau}{\tau_{\mathrm{Di}}}\right) \sqrt{1 + \frac{\tau}{S^2 \tau_{\mathrm{Di}}}}}. \tag{6.7}$$

Here $\langle N \rangle$ is the mean number of fluorescent tracers inside the observation volume V, τ_{Di} is the average diffusion time of species i ($1 \leq i \leq m$) through V and f_{i} the respective fraction of species i. S is named structural parameter and is the ratio of axial to lateral dimension z_0/r_0 of V. Since V and its dimensions are known from reference measurements using dyes with known diffusion coefficient the concentration $C = \langle N \rangle / V$ of the fluorescent species can also be evaluated. Moreover, the diffusion coefficient of species i can be obtained by $D_{\mathrm{i}} = r_0^2 / 4\tau_{\mathrm{Di}}$ and with the Stokes-Einstein relationship the corresponding hydrodynamic radius R_{H} can be determined.[18]

Figure 6.4 shows two normalized example autocorrelation curves measured at different polymer concentrations in methanol. At 11 nM the fit (eq. 6.7, $m = 1$) yields $R_{\mathrm{H}} \sim 2$ nm which corresponds to the diffusion of single polymer chains, whereas at 4600 nM the fit results in $R_{\mathrm{H}} \sim 10$ nm showing the presence of micelles.

Measurements in polymer solutions with different concentrations were conducted and the respective R_{H}'s determined. Figure 6.5 shows the concentration series of

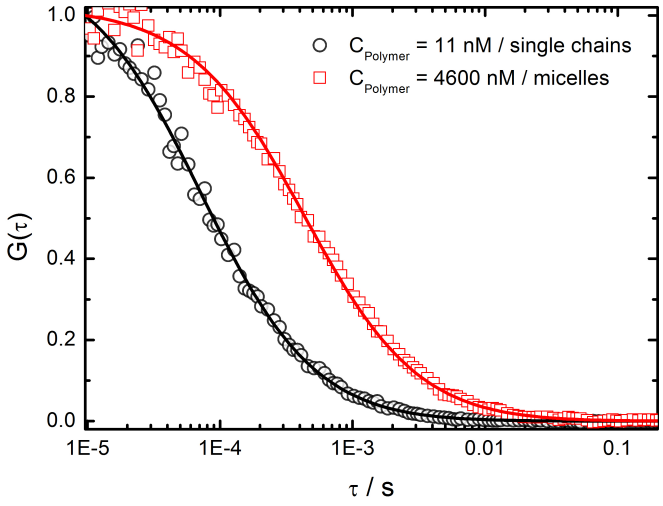

Figure 6.4: Normalized autocorrelation curves (symbols) and the corresponding fits with eq. 6.7 (solid lines) at different polymer concentrations in methanol.

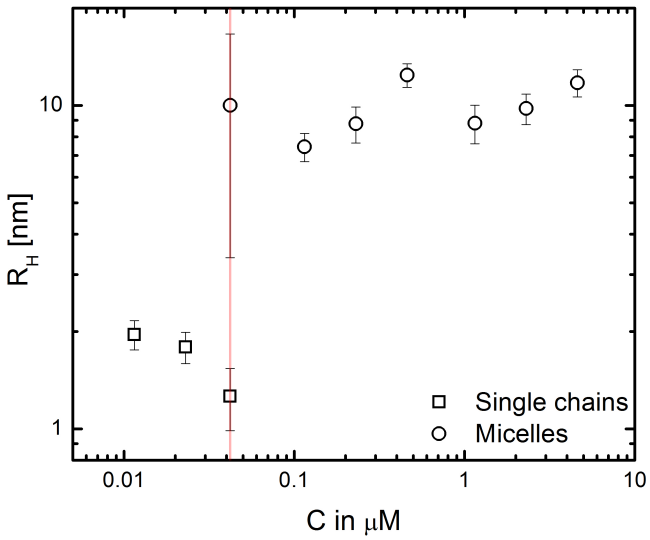

Figure 6.5: The determined hydrodynamic radii at different polymer concentrations of the micelles in methanol. The red vertical line highlights the critical micelle concentration.

the bodipy labeled polymer (8-An-PS-POEGMA, see synthesis chapter below) in methanol as an example. The analysis reveals that the lowest concentration where micelles occur lies at . A similar behavior was observed for the other bodipy labeled polymer (6-An-PS-POEGMA, see synthesis section below). Thus, $c \sim 0.04$ μM can be considered as the critical micelle concentration of the copolymer in methanol.

6.5.2. Synthesis and characterization of dyes and polymers

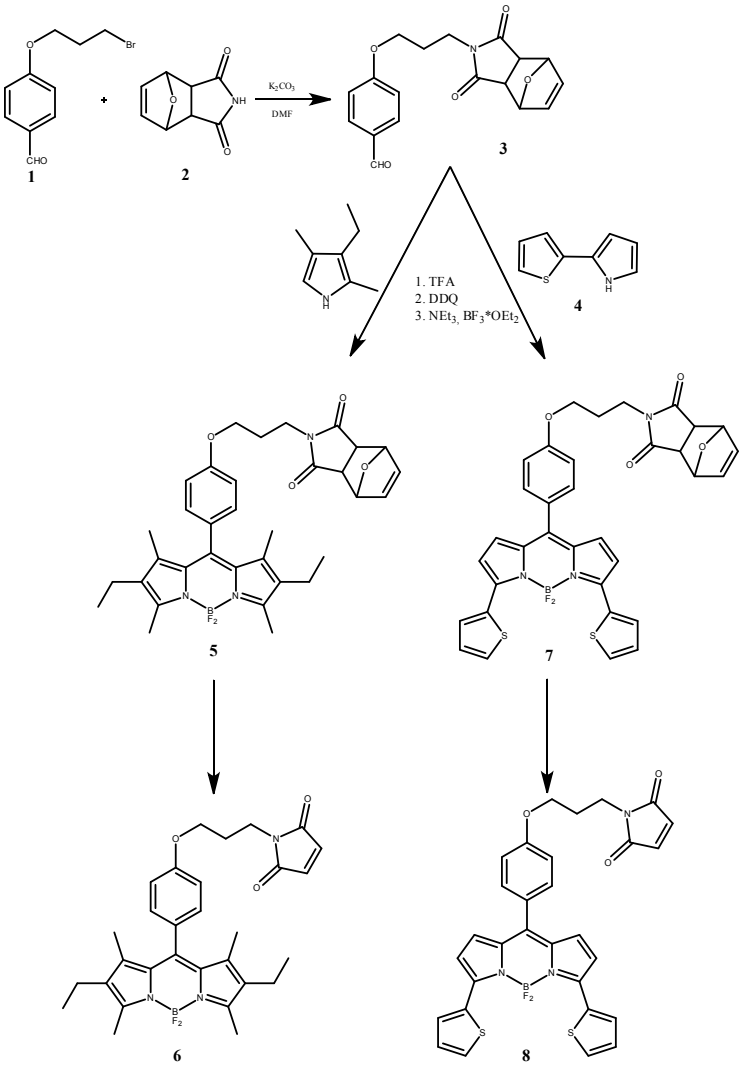

Figure 6.6: Synthesis of maleimide substituted BODIPY dyes.

K_2CO_3 (8.4 g, 61 mmol) was added to a solution of 4-(3-bromopropoxy) benzalde-

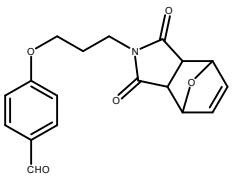

hyde[249] (**1**) (3.0 g 12.3 mmol) in dry DMF (60 mL) and the mixture was stirred for 30 min. Then a solution of furane protected maleimide[250] **2** (2.0 g, 12.3 mmol) in dry DMF (10 mL) was added. After stirring at 60 ℃ overnight, the reaction was poured into water and extracted with EtOAc (3 x 30 mL). The combined organic phases were dried over $NaSO_4$, the solvent was evaporated, and the residue was purified by column chromatography (EtOAc : n-hexane = 5:3). **3** was obtained as a white solid. ^{1}H NMR (300 MHz, $CDCl_3$), δ [ppm]: 9.85 (s, 1H, aldehyde-H), 7.79 (d, J = 8.8 Hz, 2 H, phenyl-H), 6.96 (d, J = 8.8 Hz, 2 H, phenyl-H), 6.49 (s, 2 H, protection group C<u>H</u>=C<u>H</u>), 5.21 (s, 2 H, protection group C<u>H</u>-O-C<u>H</u>), 4.00 (t, J = 6.1 Hz, 2 H, O-C<u>H</u>$_2$), 3.69 (t, J = 6.8 Hz, 2 H, N-CH_2), 2.82 (s, 2H, maleimide-H), 2.09 (m, 2 H, CH_2-CH_2-CH_2). ^{13}C NMR (75 MHz, $CDCl_3$), δ [ppm]: 190.8, 176.2, 163.8, 136.5, 132.0, 130.0, 114.7, 81.0, 65.5, 47.4, 35.9, 27.1. MS (MALDI TOF): m/z: 328.1 $[M+H]^+$. Elemental analysis: Calculated for $C_{18}H_{17}NO_5$ (327.33): C 66.05, H 5.23, N 4.28; found: C 65.68, H 5.41, N 4.23.

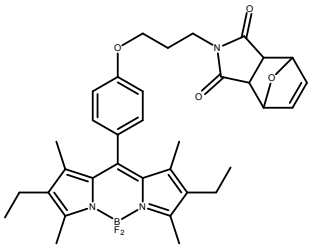

To a solution of 3-ethyl-2,4-dimethylpyrrole (0.39 g, 3.16 mmol) and **3** (0.42 g, 1.43 mmol) in dry THF (75 mL), 5 drops of trifluoroacetic acid were added and the solution was stirred overnight at room temperature. Then a solution of 2,3-dichloro-5,6-dicyano-p-benzoquinone (0.32 g, 1.43 mmol) in dry THF (25 mL) was added. After 5 h, the reaction was cooled to 0 ℃, NEt_3 (4.9 mL, 35 mmol) and borontrifluoride diethyl ether complex (5 mL, 40 mmol) were added, and the reaction was stirred for additional 15 h at room temperature. The solvent was evaporated and the crude product was purified by column chromatography (1. EtOAc : nhexane = 55:45; 2. DCM : methanol = 97:3) to obtain **5** as an orange solid (0.41 g, 48 %). ^{1}H

NMR (300 MHz, CD_2Cl_2), δ [ppm]: 7.17-7.12 (m, 2 H, phenyl-H), 7.00-6.95 (m, 2 H, phenyl-H), 6.49 (s, 2 H, protection group C<u>H</u>=C<u>H</u>), 5.19 (s, 2 H, protection group C<u>H</u>-O-C<u>H</u>), 3.99 (t, J = 6.2 Hz, 2 H, O-CH_2), 3.67 (t, J = 7.0 Hz, 2 H, N-CH_2), 2.82 (s, 2H, maleimide-H), 2.46 (s, 6 H, pyrrole-CH_3), 2.30 (q, J = 7.5 Hz, 4 H, pyrrole-C<u>H</u>$_2$-CH_3), 2.10-2.02 (m, 2 H, CH_2-C<u>H</u>$_2$-CH_2), 1.33 (s, 6 H, pyrrole-CH_3), 0.97 (t, J = 7.5 Hz, 6 H, pyrrole-CH_2-CH_3). ^{13}C NMR (75 MHz, $CDCl_3$), δ [ppm]: 176.2, 159.2, 153.5, 140.3, 138.5, 136.5, 132.6, 131.2, 129.4, 128.0, 115.0, 81.0, 65.3, 47.4, 36.2, 27.3, 17.1, 14.6, 12.5, 11.9. MS (MALDI TOF): m/z: 601.2 [M]+ 582.24 $[M\text{-}F]^+$, 533.3 [M-furane]$^+$, 514.26 [M-furane-F]$^+$. Elemental analysis: Calculated for $C_{34}H_{38}BF_2N_3O_4$ (601.49): C 67.89, H 6.37, N 6.99; found: C 67.53, H 6.53, N 7.20.

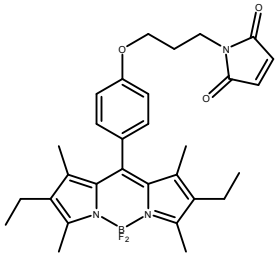

Protected BODIPY **5** (0.26 g, 0.43 mmol) was dissolved in toluene (10 mL). The reaction was stirred under reflux overnight. The solvent was then evaporated and the crude product was purified by column chromatography (DCM). **6** was obtained as an orange solid (0.19 g, 81 %). ^{1}H NMR (300 MHz, CD_2Cl_2), δ [ppm]: 7.16-7.12 (m, 2 H, phenyl-H), 6.97-6.94 (m, 2 H, phenyl-H), 6.68 (s, 2 H, maleimide-H), 4.02 (t, J = 6.1 Hz, 2 H, O-CH_2), 3.72 (t, J = 6.9 Hz, 2 H, N-CH_2), 2.45(s, 6 H, pyrrole-CH_3), 2.30 (q, J = 7.5 Hz, 4 H, pyrrole-C<u>H</u>$_2$-CH_3), 2.13-2.04 (m, 2 H, CH_2-C<u>H</u>$_2$-CH_2), 1.33 (s, 6 H, pyrrole-CH_3), 0.96 (t, J = 7.5 Hz, 6 H, pyrrole-CH_2-C<u>H</u>$_3$). ^{13}C NMR (75 MHz, CD_2Cl_2), δ [ppm]: 171.2, 159.7, 153.8, 140.9, 139.1, 134.6, 133.2, 131.5, 129.9, 128.2, 115.4, 66.2, 35.6, 28.6, 17.4, 14.8, 12.6, 12.0. MS (MALDI TOF): m/z: 533.29 $[M]^+$, 514.28 $[M\text{-}F]^+$. Elemental analysis: Calculated for $C_{30}H_{34}BF_2N_3O_3$(533.42): C 67.55, H 6.42, N 7.88; found: C 66.57, H 6.50, N 7.73.

10 drops of trifluoroacetic acid were added to a solution of 2-(thiophen-2-yl)-1H-pyrrole[1] (0.54 g, 3.62 mmol) and **3** (0.54 g, 1.65 mmol) in dry DCM (75 mL) and the solution was stirred overnight at room temperature. Then a solution of 2,3-dichloro-5,6-dicyano-*p*-benzoquinone (0.38 g, 1.65 mmol) in dry DCM (50 mL)

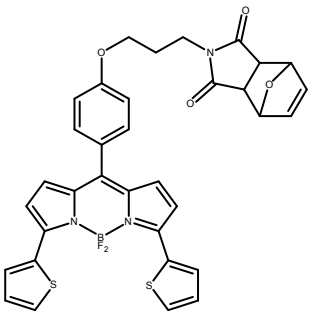

was added. After 3 h, the reaction was cooled to 0 ℃, NEt_3 (7 mL, 50 mmol), and borontrifluoride diethyl ether complex (7 mL, 55 mmol) were added, and the reaction was stirred overnight at room temperature. The solvent was evaporated and the crude product was purified by column chromatography (1. EtOAc : n-hexane = 7:3; 2. DCM : acetone = 9:1) to obtain **7** as a purple solid (0.22 g, 20 %). ^{1}H NMR (300 MHz, CD_2Cl_2), δ [ppm]: 8.12 (dd, ^{3}J = 3.8 Hz, ^{4}J = 1.0 Hz, 2 H, thiophene-H), 7.52 (dd, ^{3}J = 5.1 Hz, 4J = 1.0 Hz, 2 H, thiophene-H), 7.50-7.47 (m, 2 H, phenyl-H), 7.19 (dd, ^{3}J = 5.1 Hz, 3J = 3.9 Hz, 2 H, thiophene-H), 7.03-6.99 (m, 2 H, phenyl-H), 6.88 (d, ^{3}J = 4.3 Hz, 2 H, pyrrole-H), 6.83 (d, ^{3}J = 4.5 Hz, 2 H, pyrrole-H), 6.50 (s, 2 H, protection group C<u>H</u>=C<u>H</u>), 5.20 (s, 2 H, protection group C<u>H</u>-O-C<u>H</u>), 4.02 (t, J = 6.1 Hz, 2 H, O-CH_2), 3.68 (t, J = 6.1 Hz, 2 H, N-CH_2), 2.84 (s, 2H, maleimide-H), 2.13-2.04 (m, 2 H, CH_2-C<u>H</u>$_2$-CH_2). MS (MALDI TOF): m/z: 653.01 $[M]^+$, 634.00 $[M\text{-}F]^+$, 585.03 [M-furane]$^+$.

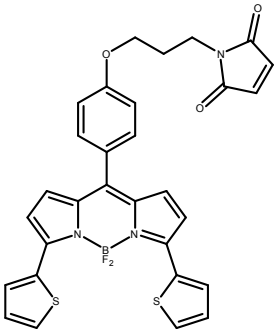

The protected BODIPY **7** (0.21 g, 0.32 mmol) was dissolved in toluene (15 mL). The reaction was stirred under reflux overnight. The solvent was then evaporated and the crude product was purified by column chromatography (DCM). **8** was obtained as a purple solid (0.16 g, 85 %). ^{1}H NMR (300 MHz, CD_2Cl_2), δ [ppm]: ^{1}H NMR (300 MHz, CD_2Cl_2), δ [ppm]: 8.12 (dd, ^{3}J = 3.9 Hz, ^{4}J = 1.0 Hz, 2 H, thiophen-H),

7.52 (dd, ^{3}J = 5.1 Hz, ^{4}J = 1.0 Hz, 2 H, thiophen-H), 7.50-7.47 (m, 2 H, phenyl-H), 7.19 (dd, ^{3}J = 5.0 Hz, ^{3}J = 3.9 Hz, 2 H, thiophene-H), 7.03-6.99 (m, 2 H, phenyl-H), 6.88 (d, ^{3}J = 4.4 Hz, 2 H, pyrrole-H), 6.83 (d, ^{3}J = 4.4 Hz, 2 H, pyrrole-H), 6.70 (s, 2 H, maleimide-H), 4.06 (t, J = 5.9 Hz, 2 H, O-CH_2), 3.74 (t, J = 6.8 Hz, 2 H, N-CH_2), 2.15-2.07 (m, 2 H, CH_2-C$\underline{H}_2$-CH_2). MS (MALDI TOF): m/z: 585.26 $[M]^+$, 566.24 $[M\text{-}F]^+$. Elemental analysis: Calculated for $C_{30}H_{22}BF_2N_3O_3S_2$ (585.45): C 61.55, H 3.79, N 7.18, S 10.95; found: C 61.26, H 3.55, N 7.08, S 11.15.

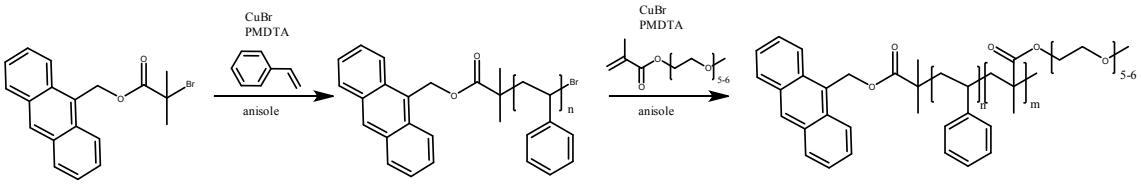

Figure 6.7: Synthesis of anthracene substituted diblock copolymer An-PS-POEGMA.

Anthracene-9-ylmethyl-2-bromo-2-methylpropanoate[251] (35.6 mg, 0.1 mmol), CuBr (28.7 mg, 0.2 mmol, PMDTA(42 μL, 0.2 mmol) and styrene (1.5 g, 15 mmol) were dissolved in anisole (2.5 mL). After three freeze-pump-thaw circles, the solution was stirred at 110 ℃ for 2 h. The solution was then diluted by THF (5 mL), passed through a column of neutral aluminium oxide, and concentrated in vacuo followed by precipitation from methanol to obtain the polymer An-PS as a white solid. $M_{n,GPC}$ = 4800 g·mol^{-1}; M_w/M_n = 1.18 (Figure 6.8). An-PS (200 mg), CuBr (14.4 mg, 0.1 mmol), PMDTA (21 μL, 0.1 mmol) and OEGMA (1.5 g) were dissolved in anisole (2.5 mL). After three freeze-pump-thaw circles, the solution was stirred at 60 ℃ for 1 h. The solution was then diluted by THF (5 mL), passed through a column of neutral aluminium oxide, concentrated in vacuo, and precipitated from n-hexane to obtain the copolymer An-PS-POEGMA. Mn,GPC = 8100 g·mol^{-1}; M_w/M_n = 1.21 (Figure 6.8).

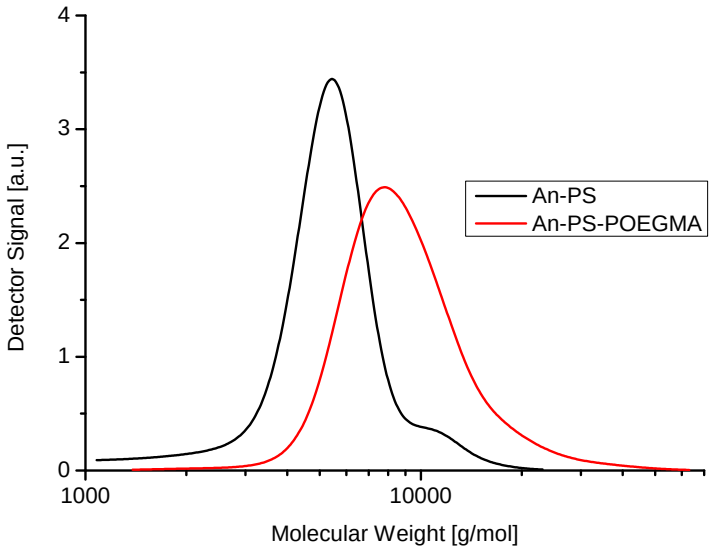

Figure 6.8: GPC traces (UV/Vis detector, 254 nm) of An-PS (black) and An-PS-POEGMA (red).

General synthesis of BODIPY labelled copolymers: **An-PS-POEGMA** (90 mg) and BODIPY dyes **6** or **8** (2 equivalents) were dissolved in DMF (1.5 mL). The reaction was stirred at 80 ℃ for 16 h. The solution was then diluted with DCM (5 mL) and the polymer was precipitated from *n*-hexane. The crude product was purified by column chromatography (DCM : THF = 1:1 → THF → THF : MeOH: 10:1) to obtain **6-An-PS-POEGMA** and **8-An-PS-POEGMA** as solids. GPC analysis revealed no remaining unreacted BODIPY dyes.

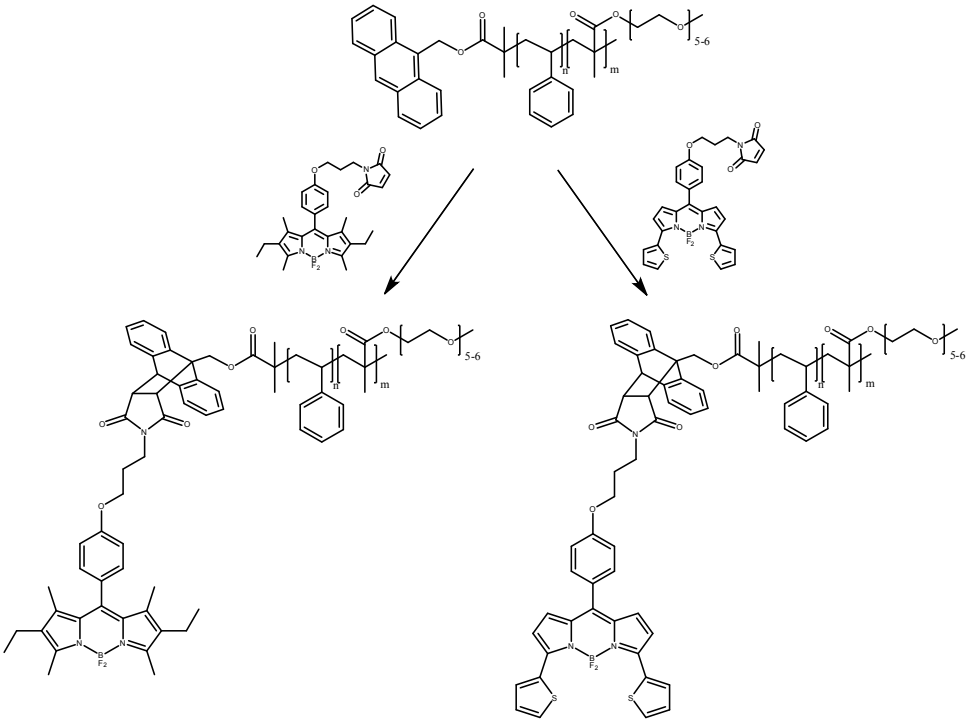

Figure 6.9: Labelling of the copolymer An-PS-POEGMA with BODIPY dyes 6 and 8 by a Diels-Alder reaction.

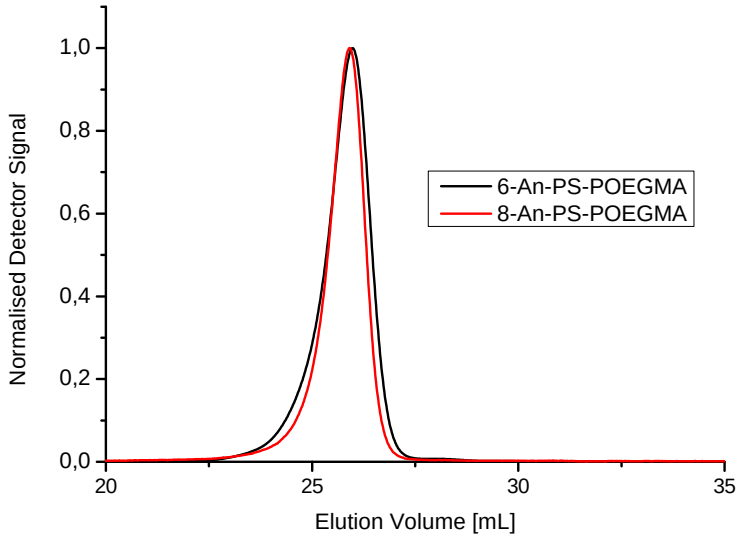

Figure 6.10: GPC traces (UV/Vis detector) of 6-An-PS-POEGMA (black, 525 nm) and 8-An-PS-POEGMA (red, 600 nm).

6.6. Acknowledgment

The financial support from DFG (SFB 1066, Q2) is gratefully acknowledged.

7. FCS in dilute polymer solutions: accounting for the molar mass dispersity

Fluorescence correlation spectroscopy (FCS) has become an important tool in polymer science. Among various other applications the method is often applied to measure the hydrodynamic radius and the degree of fluorescent labeling of polymers in dilute solutions. Here we show that such measurements can be strongly affected by the molar mass dispersity of the studied polymers and the way of labeling. As model systems we used polystyrene and poly (methyl methacrylate) synthesized by atom transfer radical polymerization or free-radical polymerization. Thus, the polymers were either end-labeled bearing one fluorophore per chain or side-labeled with the number of fluorophores per chain proportional to the degree of polymerization. The experimentally measured autocorrelation curves were fitted with a newly de-

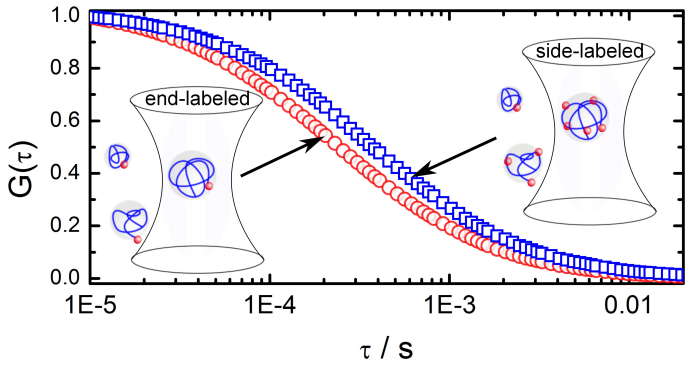

rived theoretical model that uses the Schulz-Zimm distribution function to describe the dispersity in the degree of polymerization. For end-labeled polymers having a molecular weight distribution close to Schulz-Zimm, the fits yield values of the number average degree of polymerization and the polydispersity index similar to those obtained by reference gel permeation chromatography. However, for the side-labeled polymers such fitting becomes unstable, especially for highly polydisperse systems. Brownian dynamic simulations showed that the effect is due to a mutual

dependence between the fit parameters, namely the polydispersity index and the number average molecular weight. As a consequence, an increase of the polydispersity index can be easily misinterpreted as an increase of the molecular weight when the FCS autocorrelation curves are fitted with a standard single component model, as commonly done in the community.

Reproduced with permission from:
D. Schaeffel, S. Yordanov R.H. Staff, A. Kreyes, Y. Zhao, M. Schmidt, K. Landfester, J. Hofkens, H.-J. Butt, D. Crespy, K. Koynov: Fluorescence correlation spectroscopy in dilute polymer solutions: effects of molar mass dispersity and the type of fluorescent labeling, *ACS Macro Lett.*, **2015**, *4*, 171-176.

7.1. Introduction

Fluorescence correlation spectroscopy (FCS) is a sensitive and selective technique for studying the mobility of fluorescent species, such as, small molecules, macromolecules or nanoparticles, in various environments.[64] Commonly, the diffusion coefficient, fluorescent brightness, and concentration of the fluorescent species are measured and used to assess their size, aggregation behavior, interactions with other species or to obtain information about the surrounding environment.[64] While initially developed[53] and still predominantly used as a tool in molecular and cell biology[8,9] or to investigate colloidal systems[10], during the last decade FCS has also become an established technique in polymer science.[11] For example, diffusion of molecular and macromolecular tracers in polymer solutions,[183,186,187,252] cross-linked polymer networks,[189,192,253] and bulk polymers[254] has been studied. FCS was also applied to investigate the interfacial diffusion of homo- and co-polymers,[180,255] their self-assembly in micelles[15,17] or vesicles[147,244] and even the process of polymerization itself.[92] One of the most characteristic properties of polymers is their molar mass dispersity. However, it is a common perception that compared to some classical techniques such as gel permeation chromatography (GPC) or photon correlation spectroscopy (PCS), FCS is not sensitive to moderate variations in the size of the studied polymers and thus to their molar mass dispersity. The reduced sensitivity

is related to the rather slow, hyperbolic decay of the FCS autocorrelation function compared to the exponential decay in PCS. Thus, in many FCS studies of polymers the effect of polydispersity is neglected. Moreover, the method was never applied to explicitly measure the polydispersity index of flexible chain polymers in solutions. In this letter we show that in many practical cases, polydispersity may strongly affect the experimentally measured FCS autocorrelation curves. If not properly accounted for, this leads to errors in the estimated average molecular weight. Here a key parameter is the kind of fluorescent labeling, e.g. end chain labeling with one fluorophore per polymer chain vs. side chain labeling, with a number of fluorophores proportional to the degree of polymerization. We explore these effects by deriving a new theoretical model for the FCS autocorrelation function in the case of polydisperse polymers and comparing it to experimentally measured data and Brownian dynamic simulations.

7.2. Theoretical section

7.2.1. Fluorescence Correlation Spectroscopy

In a typical FCS experiment, a laser beam is tightly focused into a solution of the fluorescent species via a high numerical aperture microscope objective. The emitted fluorescence is collected by the same objective and after passing through a dichroic mirror, an emission filter and a confocal pinhole, delivered to a fast and sensitive detector, usually an avalanche photo diode. These arrangements lead to the formation of a sub-femtoliter observation volume V_{obs} with a Gaussian ellipsoid shape. Only fluorescence emitted from species inside V_{obs} is detected. The Brownian diffusion of the fluorescent species in and out of the observation volume V_{obs} creates temporal fluctuations in the detected fluorescence intensity $\delta F(t)$ that are recorded and evaluated in terms of an autocorrelation function:

$$G(\tau) = 1 + \frac{\langle \delta F(t) \delta F(t+\tau) \rangle}{\langle F(t) \rangle^2} \tag{7.1}$$

For an ensemble of identical, freely diffusing fluorescent species, not affected by photo-physical processes such as transition to a triplet state, $G(\tau)$ has the following

analytical form:[64]

$$G(\tau;\tau_{\mathrm{D}}) = 1 + \frac{1}{\langle N\rangle} M(\tau;\tau_{\mathrm{D}}) \tag{7.2}$$

with

$$M(\tau;\tau_{\mathrm{D}}) = \frac{1}{\left(1+\frac{\tau}{\tau_{\mathrm{D}}}\right)\sqrt{1+\frac{\tau}{S^2\tau_{\mathrm{D}}}}} \tag{7.3}$$

Here, $\langle N\rangle$ is the average number of fluorescent species in the observation volume, $S = z_0/r_0$ is the ratio of the axial to the radial dimension of V_{obs} and τ_{D} is the species' diffusion time that is directly related to their diffusion coefficient

$$D = \frac{r_0^2}{4\tau_{\mathrm{D}}} \tag{7.4}$$

and by the Stokes-Einstein relation to their hydrodynamic radius.

7.2.2. Multi-component FCS

For a more complex system, in which the studied fluorescent species are not identical, the autocorrelation function can be expressed as:

$$G(\tau;\tau_{\mathrm{D}}) = 1 + \frac{1}{\langle N\rangle} \frac{\int_0^\infty P(\tau_{\mathrm{D}}) M(\tau;\tau_{\mathrm{D}}) \varepsilon(\tau_{\mathrm{D}})^2 d\tau_{\mathrm{D}}}{\left(\int_0^\infty P(\tau_{\mathrm{D}})\varepsilon(\tau_{\mathrm{D}}) d\tau_{\mathrm{D}}\right)^2}. \tag{7.5}$$

Here $P(\tau_{\mathrm{D}})$ is a size distribution function describing the number fraction of species with certain size, and therefore certain diffusion coefficient and diffusion time τ_{D}. The fluorescent brightness distribution function $\varepsilon(\tau_{\mathrm{D}})$ accounts the fact that the studied species may have also different fluorescent brightness *e.g.* due to a different number of fluorophores attached to them.

Eq. 7.5 was previously considered by Starchev et al.[47] who had approximated it by a sum of large number (~ 30) of terms with discrete diffusion times using the method of histograms. While representing an experimental autocorrelation curve in this way is an ill-posed problem, by imposing additional regularization and constraint conditions the authors were able to estimate the polydispersity of dispersed colloidal particles. Following a similar approach, Sengupta et al.[49] have used a Maximum Entropy Method based fitting routine (MEMFCS) to analyze FCS data for polydisperse systems in terms of a quasi-continuous distribution of diffusing com-

ponents. Here we use a different approach and instead of discretizing eq. 7.5, we derive analytical expressions for $P(\tau_D)$ and $\varepsilon(\tau_D)$. In the case of fluorescently labeled synthetic polymers dissolved in a good solvent this can be done by correlating the diffusion time of an individual polymer chain to its degree of polymerization and then applying a common continuous distribution function to describe the dispersity in the degree of polymerization.

In dilute solutions the dynamics of a polymer chain with a high degree of polymerization is described by the Zimm model.[20] In the framework of this model, a scaling dependence of the chain diffusion coefficient D on the degree of polymerization X can be established. However, this relation is only an approximation and cannot be applied to flexible chains in good solvents due to the subtle influence of excluded volume effects. Thus, we used the empirical relation

$$D = KX^{-\nu} \tag{7.6}$$

which was shown to describe very well experimental data obtained by PCS.[256,257] K and ν are constants, which depend on the polymer and the solvent and can be obtained by fitting published data[256,257] on $D(X)$ with eq. 7.6 as discussed below and in the SI. Substituting eq. 7.6 in eq. 7.4 results in:

$$\tau_D = \frac{r_0^2}{4K} X^{\nu} \tag{7.7}$$

Next, we consider the fluorescent brightness distribution function $\varepsilon(\tau_D)$ that is related to the number of fluorophores attached to a polymer chain with certain degree of polymerization X and thus certain diffusion time τ_D. Two common cases should be considered here:

(i) End chain labeling with one fluorophore per polymer chain and therefore $\varepsilon(X) = const.$

(ii) Side chain labeling, with a number of fluorophores proportional to the degree of polymerization and $\varepsilon(X) = F(X)$, where $F(X)$ is a proportionality function, depending on further specifies of the labeling procedure as discussed below.

With these considerations in mind and by inserting eq. 7.7 in eq. 7.3 to obtain an

analytical expression for $M(\tau; X)$, eq. 7.7 can be rewritten in the form:

$$G(\tau; X) = 1 + \frac{1}{\langle N \rangle} \frac{\int_0^\infty P(X) M(\tau; X) \varepsilon(X)^2 dX}{\left(\int_0^\infty P(X) \varepsilon(X) dX \right)^2}. \tag{7.8}$$

Here $P(X)$ is a continuous distribution function describing the dispersity in the degree of polymerization of the studied polymer system. For example, for polymers synthesized by atom transfer radical polymerization (ATRP) it was theoretically predicted that $P(X)$ should be a Poisson function. However, this prediction is based on the assumption of 100 % monomer conversion and no side reactions[161] and thus is often not applicable to real systems. A more realistic distribution function describing the dispersity in the degree of polymerization is the Schulz-Zimm distribution:[20]

$$P(X) = \frac{\xi^{\xi+1}}{\Gamma(\xi+1)} \frac{X^{\xi-1}}{\langle X \rangle^\xi} \exp\left(-\xi \frac{X}{\langle X \rangle} \right) \tag{7.9}$$

with $\langle X \rangle$ being the number average degree of polymerization and $\xi = 1/(PDI - 1)$ the chain coupling coefficient that is related to the polydispersity index $PDI = M_w/M_n$. Here M_w is the weight average molecular weight and M_n the number average molecular weight.

7.3. Results and Discussion

We used eq. 7.8 to fit experimental autocorrelation curves measured for dilute toluene solutions of fluorescently labeled PS and PMMA and compared the obtained values of $\langle X \rangle$ and PDI with the results of a GPC characterization. A detailed description of the polymers synthesis and their characterization is given in SI. The FCS experiments were performed on a commercial setup (Zeiss, Germany) consisting of the module ConfoCor2 and an inverted microscope model Axiovert 200, following a procedure reported earlier[254] and described in details in SI.

7.3.1. End-labeled polymers

First, several polymers (Table 7.1) prepared by atom transfer radical polymerization (ATRP) were studied. The fluorophore was present in the initiator (SI) and thus one fluorophore was attached per polymer chain. Typical experimental autocorrelation

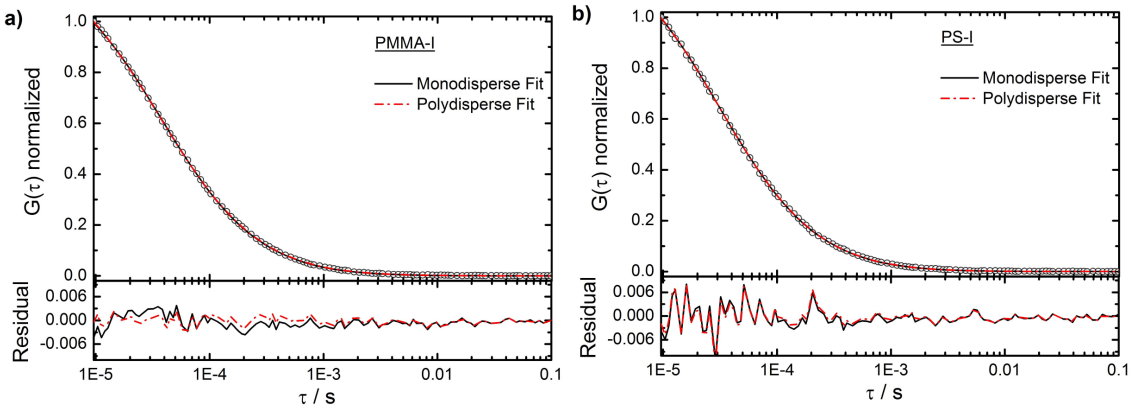

Figure 7.1: Experimental autocorrelation curves (symbols) measured in dilute ($\sim$ 10 nM) toluene solutions of the polymers PMMA-I (a) and PS-I (b). The lines in the upper panels represent the corresponding fits with the polydisperse, (eq. 7.8, dash dotted line) and the monodisperse (eq. 7.2, straight line) models. The low panels show the corresponding residuals

curves and their corresponding fits using eq. 7.8 are shown in Figure 7.1. The fitting was done using a standard least-squares nonlinear fitting procedure and numerically evaluating the integrals in eq. 7.8 at each iteration step. Due to the one fluorophore per chain labeling the chain fluorescent brightness does not depend on the degree of polymerization, $\varepsilon(X) = const$. This simplifies eq. 7.8 and leaves only the average number of fluorescent species in the observation volume $\langle N \rangle$, the number average degree of polymerization $\langle X \rangle$ and the polydispersity index PDI as fit parameters. For comparison the experimental data was also fitted with a single component, "monodisperse" model (eq. 7.2) as commonly done in previous studies. In this case the fit parameters were only $\langle N \rangle$ and X. For both type of fits the values of $K_{\mathrm{PS}} = 1.598 \cdot 10^{-9}$ and $\xi_{\mathrm{PS}} = 0.512$ for PS and $K_{\mathrm{PMMA}} = 1.885 \cdot 10^{-9}$ and $\xi_{\mathrm{PMMA}} = 0.526$ for PMMA were used to calculate the chain diffusion coefficient from its degree of polymerization. These values were obtained by fitting experimental data[256,257] on $D(X)$ with eq. 7.6. Only data in relatively narrow X range covering the values of X of the polymers listed in Table 7.1 were used (SI).

As can be seen in Figure 7.1a for a sample with moderate molar mass dispersity, PMMA-I ($PDI_{\mathrm{GPC}} = 1.33$, Table 7.1) the polydisperse model provides distinctly better fit (lower and uniform residuals) than the monodisperse model. On the other hand as shown in Figure 7.1b, for polymers with lower molar mass dispersity

Table 7.1: Degree of polymerization and polydispersity index of end-labeled PMMA and PS polymers as evaluated by GPC and FCS. The parameter (χ^2) represents the goodness of the fit.

Sample	GPC		FCS: Poly. Fit (eq. 7.8)			FCS: Mono. Fit (eq. 7.2)	
	$\langle X \rangle$	PDI	$\langle X \rangle$	PDI	$\chi^2 \cdot 10^{-5}$	$X_{\text{Mono.}}$	$\chi^2 \cdot 10^{-5}$
PMMA-I	149	1.33	111 ± 2	1.34 ± 0.07	1.5	102 ± 5	3.3
PMMA-II	188	1.17	145 ± 4	1.32 ± 0.1	3.2	133 ± 7	4.6
PS-I	76	1.21	62 ± 3	1.17 ± 0.13	11.6	60 ± 3	12.1
PS-II	87	1.24	81 ± 3	1.49 ± 0.12	3.8	72 ± 4	6.9

e.g. PS-I ($PDI_{\text{GPC}} = 1.21$, Table 7.1) the difference between the fits with the two models is barely visible. Nevertheless, even in this case the residuals (lower panel in Figure 7.1b) highlight a slight improvement in fitting when applying the polydisperse model. Moreover as shown in Table 7.1 for all studied polymers the polydisperse model yielded lower χ^2 values[258] and therefore better fits than the monodisperse model. These results indicate that FCS is sensitive even on small polydispersities of polymers. In the same time, our findings also demonstrate the existence of a lower border of $PDI \leq 1.2$ below which no significant difference between the standard monodisperse model (eq. 7.2) and the polydisperse model (eq. 7.8) can be detected.

The results from both types of fits for all studied samples are summarized in Table 7.1) and compared to the respective GPC data (SI). Fitting experimental FCS data of PS-I and PMMA-I with the polydisperse model (Figure 7.1) yielded PDI values that within the error bars (nonlinear regression parameter confidence intervals of 95 %) were identical to the corresponding GPC values. We emphasize here that the derived polydisperse FCS model (eq. 7.8) relies on the similarity of the molar mass dispersity of the polymers to an ideal Schulz-Zimm distribution. PMMA-II and PS-II are examples where the size distribution deviated significantly from the Schulz-Zimm distribution (Figure S3 c & d). Correspondingly, the FCS yielded PDI values only in mediocre agreement with those from GPC. On the other hand, the good agreement between the GPC and FCS data for the sample PMMA-I shows that FCS can be used for measuring the molar mass dispersity of polymers even when the molar mass distribution moderately deviates from an ideal Schulz-Zimm distribution (Figure S3 a).

With respect to the values of the average degree of polymerization $\langle X \rangle$ obtained

with the polydisperse FCS model (Table 7.1) for PS the agreement with the corresponding GPC values is much better than for PMMA. This is probably caused by more accurate data for D vs. X for PS than for PMMA (Figure S2). At this point, it is also instructive to consider the results obtained by fitting the experimental FCS autocorrelation curves with the simple monodisperse model (eq. 7.2) as it commonly done in most existing studies. The results summarized in Table 7.1 indicate that such fit yields a degree of polymerization value that is relatively close to the number average value obtained by polydisperse FCS model fit or by GPC. Thus, the application of this simple FCS model to single fluorophore labeled polymers is relatively safe and provides reasonable results.

7.3.2. Statistically-labeled polymers

The situation changes qualitatively for side chain labeling. Here the number of fluorophores per chain is proportional to the degree of polymerization. In such case the dependence of the individual chain brightness on the degree of polymerization $\varepsilon(X) = F(X)$ has to be considered, which complicates eq. 7.8 significantly. The physical picture is that the longer chains carry more fluorophores than the shorter ones and thus contribute stronger to the FCS autocorrelation curve, much as it happens in PCS. In order to study such situation experimentally, we copolymerized styrene and methacrylate functionalized BODIPY dye in a free radical solution polymerization process yielding the polymer PS-III (SI). GPC revealed a number average degree of polymerization $\langle X_{\mathrm{GPC}} \rangle = 1863$ and a $PDI_{\mathrm{GPC}} = 2.49$. Next, we recorded experimental FCS autocorrelation curves for dilute toluene solutions of PS-III and fitted them with eq. 7.8. We used values of $K_{\mathrm{PS}} = 2.304 \cdot 10^{-9}$ and $\nu_{\mathrm{PS}} = 0.581$ to describe the relation between diffusion coefficient and degree of polymerization (eq. 7.6) for this high molecular weight sample (SI). Furthermore the fits were done assuming linear dependence between the chain fluorescent brightness (number of fluorophores per chain) and the degree of polymerization, *i.e.* $\varepsilon(X) = A \cdot X$, with $A = const$. Such fitting, however, was not stable with respect to the starting values of the fitting parameters and thus, failed to produce values of the degree of polymerization $\langle X_{\mathrm{FCS}} \rangle$ and polydispersity index PDI_{FCS} consistent with the GPC results.

Thus, in order to prove the general validity of our approach and identify possible

Table 7.2: The degree of polymerization and the polydispersity index obtained with FCS by fitting simulated autocorrelation curves for statistically labeled polymers with degree of polymerization $\langle X_{\text{Sim.}} \rangle = 1000$ and $PDI_{\text{Sim.}}$ ranging from 1.0 to 2.5.

	Polydisperse Fit (eq. 7.8)		Monodisperse Fit (eq. 7.2)
$PDI_{\text{Sim.}}$	PDI_{FCS}	$\langle X_{\text{FCS}} \rangle$	$X_{\text{Mono.}}$
1.0	1.02 ± 0.02	979 ± 23	1031 ± 2
1.1	1.12 ± 0.04	983 ± 50	1201 ± 4
1.5	1.39 ± 0.15	1109 ± 162	1798 ± 13
2.0	1.79 ± 0.38	1150 ± 312	2607 ± 24
2.5	3.2 ± 2.22	762 ± 603	3458 ± 45

experimental pitfalls, we simulated "ideal experimental FCS autocorrelation curves" for a system with perfect Schulz-Zimm distribution and chain fluorescent brightness $\varepsilon X = A \cdot X$ and fitted them with eq. 7.8. The simulation was done by adapting a previously proposed fast simulation algorithm,[259] that produces autocorrelation curves for freely diffusing point like particles with given diffusion coefficient and fluorescent brightness (SI). Briefly, Schulz-Zimm distribution (eq. 7.9) was used as a probability function for the generation of a chain with degree of polymerization X. To model the statistical labeling every 100th repeat unit was set as carrying a fluorophore, thus allowing only integer numbers of fluorophores per chain. This chain was then considered as a point like particle with diffusion coefficient given by eq. 7.6 and fluorescent brightness essentially linearly proportional to X. By generating a high number ($\sim 2{\cdot}10^5$) of such chains/particles and propagating them with Brownian dynamics procedure trough the FCS probing volume[259] a highly accurate autocorrelation curve was produced. Using this procedure we simulated experimental autocorrelation curves for PS with number average degree of polymerization $\langle X_{\text{Sim.}} \rangle = 1000$ and different values of $PDI_{\text{Sim.}}$ ranging from 1.0 to 2.5. Typical curves and their fits with eq. 7.8 assuming $\varepsilon(X) = A \cdot X$ are shown in Figure 7.2 and the corresponding fit parameters are summarized in Table 7.2. The data show that in all cases the fitting yielded $\langle X \rangle$ and PDI values that within the fit errors are identical to the predefined values used in the simulations.

However, another important result from the fitting of the simulated autocorrelation curves (Table 7.2) is that when increasing the molar dispersity of the simulated

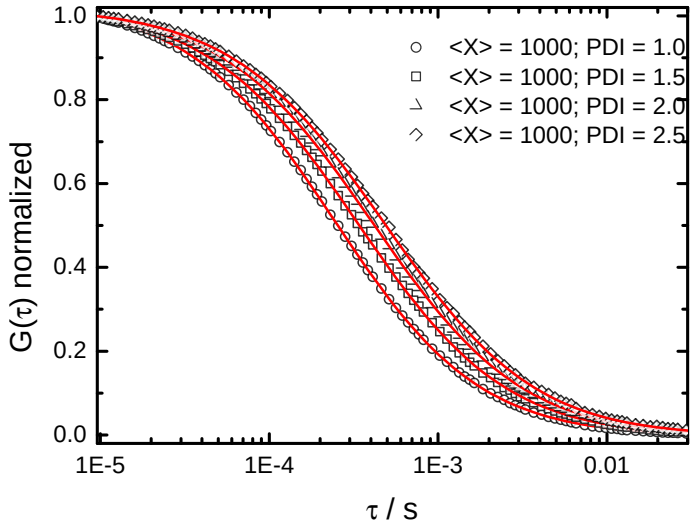

Figure 7.2: Simulated "experimental" FCS autocorrelation curves for statistically labeled polymers with different polydispersities (symbols) and their fits (lines) with eq. 7.8. Also see Figure S5 for more details.

polymer system, $PDI_{\text{Sim.}}$ from 1.0 to 2.5 the errors of the obtained fit parameters $\langle X_{\text{FCS}} \rangle$ and PDI_{FCS} (for a nonlinear regression parameter confidence intervals of 95 %) increase from roughly 2 % to more than 80 % (Table 7.2). This suggests an increasing mutual dependence between those two fit parameters. This mutual dependence is also evident when considering the autocorrelation curves shown in Figure 7.2. While all curves represent polymers with the same number average degree of polymerization $\langle X \rangle = 1000$, the increase of PDI has the same effect as an increase of $\langle X_{\text{FCS}} \rangle$, namely shifts the decay of the correlation curves to higher lag-times. The reason for this effect is the squaring of the fluorescent brightness $\varepsilon(X)$ in eq. 7.8 which results in a stronger weighting of the longer, higher labeled polymer chains. This result clearly demonstrates the danger of using the simple monodisperse fit model (eq. 7.2) with respect to such FCS data as it misinterprets the increase of PDI as an increase in the degree of polymerization (Table 7.2). Furthermore, our data suggest that for such ideally statistically labeled polymer systems a simple monodisperse fit will yield X value that is even larger than the weight average degree of polymerization.

We now return to the real polymer sample PS-III and note that is polydispersity as measured by GPC is $PDI_{\text{FCS}} = 2.49$. A comparison with the simulated ideal

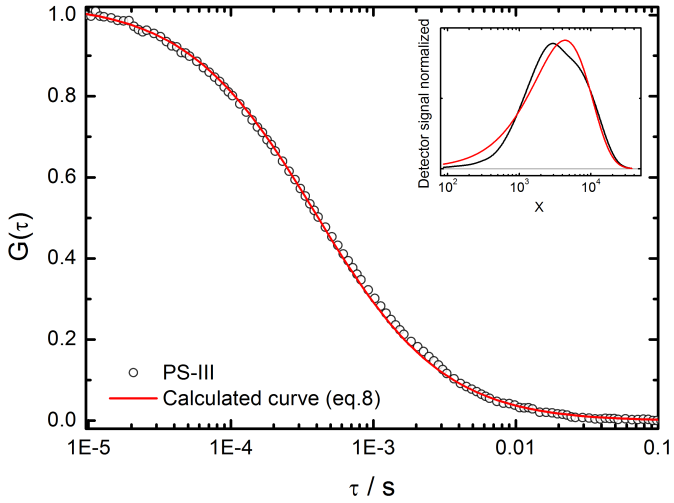

Figure 7.3: Experimental FCS autocorrelation curve measured in dilute toluene solutions of the polymer PS-III (symbols) and calculated FCS curve (solid line) using the polydisperse FCS model for a statistically labeled polymer (eq. 7.8). The values of $\langle X \rangle$ and PDI in eq. 7.8 were fixed to the corresponding GPC values. The inset shows the GPC trace of PS-III (black line) and the fit with a Schulz-Zimm distribution (red line).

samples (Table 7.2) shows that for $PDI_{\text{Sim.}}$ of 2.5 the FCS fit errors reach 80 %. On the other hand, a real sample does not have an ideal Schulz-Zimm molar mass distribution (Figure 7.3) and the dependence between the number of fluorophores per chain and the degree of polymerization may not be perfectly linear. Thus, it is not surprising that the measured autocorrelation curve cannot be appropriately fitted with the model of eq. 7.8. Thus, our results indicate that for highly polydisperse systems, with a PDI above 2.0, the model (eq. 7.8) may not always provide a stable fit to experimental FCS data of statistically labeled polymers. Nevertheless, in order to further explore the limits of the model we applied it to fit the experimental data for sample PS-III, by fixing one of the parameters, either $\langle X \rangle$ or PDI during the fitting procedure to its GPC value (SI). This yielded $\langle X_{\text{FCS}} \rangle = 1960 \pm 47$ and $PDI_{\text{FCS}} = 2.60 \pm 0.05$, values that are basically identical to the GPC values showing the successful representation of the experimental data with eq. 7.8. This is further illustrated in Figure 7.3 that compares the experimental autocorrelation curve of sample PS-III with a calculated curve using eq. 7.8 with $\langle X \rangle$ or PDI fixed to their GPC values.

7.3.3. Conclusion

In conclusion, we have shown that when FCS is used to characterize fluorescently labeled polymers, their polydispersity and type of fluorescent labeling play an important role. This can make the determination of the polymer hydrodynamic radius and thus estimation of the molecular weight nontrivial, particularly when experimental autocorrelation curves for polydisperse polymers are fitted with simple monodisperse model as commonly carried out in existing studies. For polydisperse polymers bearing one (or a constant number) of fluorophores per chain such fitting will provide the number average value of the hydrodynamic radius. In contrast if the number of fluorophores per chain is proportional to the degree of polymerization the fit will yield a significantly larger value. To address this issue we have derived a new model for the FCS autocorrelation function that uses the Schulz-Zimm distribution function to describe the dispersity in the degree of polymerization and an explicit relation to connect the chain diffusion coefficient to its molecular weight. The validity of the model and its limits were explored by comparing it to experimentally measured data and Brownian dynamic simulations.

7.4. Supporting Information

7.4.1. Fluorescence Correlation Spectroscopy (FCS)

FCS experiments were conducted on a commercial setup (Zeiss) comprising an inverted microscope Axiovert 200M and the FCS module ConfoCor 2. A 25 mW argon-ion laser at a wavelength of $\lambda = 488$ nm was used for excitation. Throughout all measurements a Zeiss alpha-Plan-Fluar 100x / 1.46 oil immersion objective was utilized and fluorescence was filtered with a LP505 nm long pass emission filter (Zeiss). As sample cell an Attofluor® cell chamber (Molecular Probes) with mounted microscope coverslip was used. All studied polymers were dissolved in toluene (Aldrich) at concentrations of approximately 10^{-8} M. The size of the FCS observation volume was determined by calibration with PMI as a dye with known

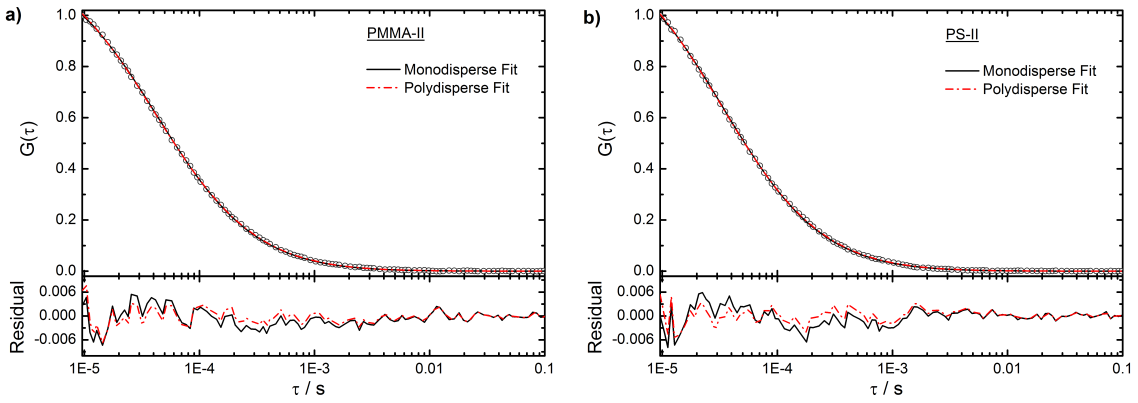

Figure 7.4: Experimental autocorrelation curves (symbols) and corresponding fits using the monodisperse model, eq. 7.2 (straight line) and the polydisperse model, eq. 7.8 (dash dotted line) on the samples PMMA-II (a) and PS-II (b) measured in dilute toluene solutions. The low panels show the respective residuals.

diffusion coefficient.[254] Figure 7.4 shows the FCS fits of the samples PMMA-II, and PS-II using the monodisperse FCS model (eq. 7.2) and the polydisperse FCS model (eq. 7.8).

7.4.2. Determining parameters describing the relation between diffusion coefficient and the degree of polymerization of polystyrene and poly (methyl methacrylate)

The relation between degree of polymerization and diffusion coefficient is given by eq. 7.6 in the main paper as $D = KX^{-\nu}$. We use data published by Wunderlich et al.[257] and Burchard et al.[256] to find K and ν (table 7.3). Figure 7.5 shows the respective data and the corresponding fits. Only data in relatively narrow X range covering the values of X of the polymers considered in this work were used in each case.

Table 7.3: Values of K and ν for PMMA and PS obtained by fitting data published by Wunderlich et al.[257] and Burchard et al.[256]

Sample	K	ν
PMMA	$(1.885 \pm 0.420) \cdot 10^{-9}$	0.526 ± 0.040
PS ($< 50kM_w$)	$(1.598 \pm 0.093) \cdot 10^{-9}$	0.512 ± 0.010
PS ($> 50kM_w$)	$(2.304 \pm 0.198) \cdot 10^{-9}$	0.581 ± 0.014

7.4.3. Synthesis of fluorescently labeled polymers by atom transfer radical polymerization[1]

Materials

2,3-Dichloro-5,6-dicyanobenzoquinone (DDQ) (Alfa Aesar), 4-hydroxybenzaldehyde (Acros), 2-bromoethanol (Acros), 3-ethyl-2,4-dimethylpyrrole (Aldrich), methacryloyl chloride (Aldrich), boron trifluoride diethyl etherate (Merck), triethylamine (Merck), trifluoroacetic acid (TFA) (VWR), 2-bromo-2-methylpropanoate bromide (Merck), and dry THF (Acros) were used as received.

Characterization

^{1}H NMR and ^{13}C NMR spectra were recorded on a Bruker AMX300 at room temperature. All NMR measurements were performed in $CDCl_3$ or CD_2Cl_2 with the solvent residual peak as an internal reference [CHCl3: $\delta = 7.24$ ppm (^{1}H) and 77.0 ppm (^{13}C), CD_2Cl_2: $\delta = 5.30$ ppm (1H) and 53.0 ppm (^{13}C)].

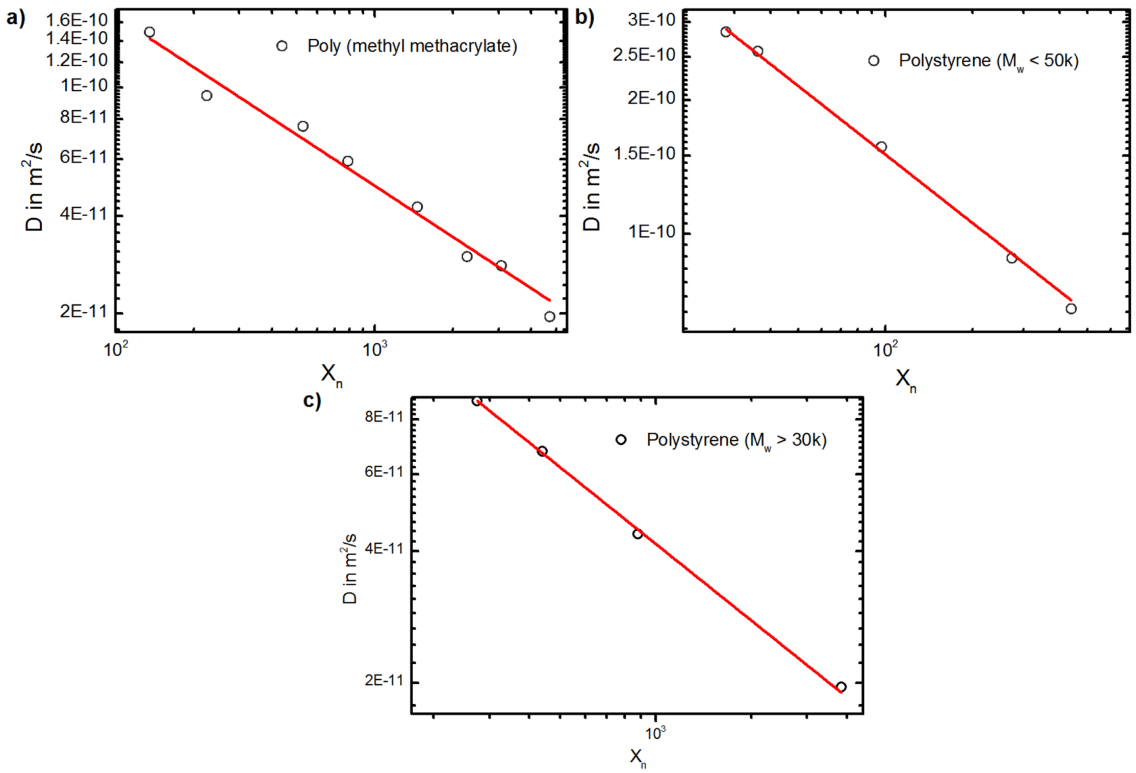

Figure 7.5: Diffusion coefficient of PMMA and PS vs. the degree of polymerization (symbols) and the corresponding fits with eq. 7.6 in the main text(solid line). The experimental data are taken from references. [256,257]

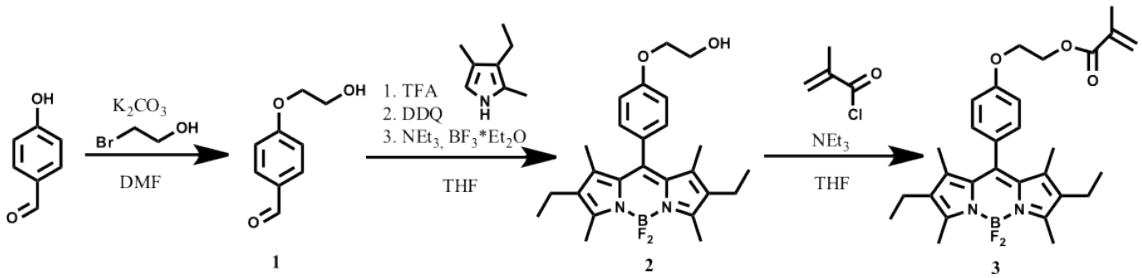

Figure 7.6: Scheme for the synthesis of the polymerizable MMA-BODIPY 3.

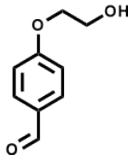

4-(2-Hydroxyethoxy)benzaldehyde (1). 4-Hydroxybenzaldehyde (5.0 g, 41 mmol) and 2-bromoethanol (6.7 g, 54 mmol) were dissolved in dry DMF (60 mL). K_2CO_3 was then added and the mixture was stirred at 80 ℃ overnight. After filtration, the solvent was evaporated and the crude product was purified by column chromatography (hexane:ethyl acetate = 2:3). **1** was obtained as a colorless oil (2.4 g, 35 %). ^{1}H NMR ($CDCl_3$, 300 MHz), δ [ppm]: 9.92 (s, 1 H, aldehyde-H), 7.89-7.85 (m, 2 H, phenyl-H), 7.07-7.03 (m, 2 H, phenyl-H), 4.21-4.18 (m, 2 H, O-CH_2), 4.05-4.02 (m, 2 H, C$\underline{H}_2$-OH). ^{13}C NMR (75 MHz, CD_2Cl_2), δ [ppm]: 191.5, 164.4, 132.3, 130.4, 115.2, 70.3, 61.3. MS (FD): m/z: 165.7 $[M]^+$.

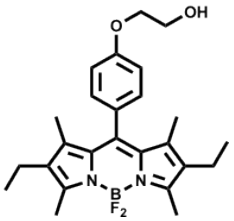

Hydroxyethoxy-BODIPY (2). **1** (1.0 g, 6.0 mmol) and 3-ethyl-2,4- dimethylpyrrole (1.7 g, 13.8 mmol) were dissolved in dry THF (70 mL). Ten drops of trifluoroacetic acid were added and the solution was stirred overnight at room temperature. A solution of DDQ (1.36 g, 6.0 mmol) in dry THF (30 mL) was added dropwise and the reaction was stirred for an additional 5 h. NEt3 (21 mL, 150 mmol) was then added and the reaction was cooled to 0 ℃. BF_2*Et_2O (20 mL, 160 mmol) was added and the reaction was stirred overnight. The solvent was evaporated and the crude product was purified by column chromatography (hexane:ethyl acetate = 1:1). **2** was obtained as red solid (1.1 g, 41 %). ^{1}H NMR (CD_2Cl_2, 300 MHz), δ [ppm]: 7.20-7.15 (m, 2 H, phenyl-H), 7.05-7.00 (m, 2 H, phenyl-H), 4.13-4.10 (m, 2 H, phenyl-O-CH_2), 3.97-3.94 (m, 2 H, C$\underline{H}_2$-OH), 2.46 (s, 6 H, pyrrole-CH_3), 2.30 (q, J = 7.5 Hz, 4 H, pyrrole-CH_2-C$\underline{H}_3$), 1.33 (s, 6 H, pyrrole-CH_3), 0.96 (t, J = 7.5 Hz, pyrrole-CH_2-C$\underline{H}_3$). ^{13}C NMR (75 MHz, $CDCl_3$), δ [ppm]: 158.5, 153.0, 139.5, 137.9, 132.2, 130.6, 129.0, 127.8, 114.5, 68.7,60.9, 16.5, 14.1, 12.0, 11.3. MS (MALDI-TOF): m/z: 440.10 $[M]^+$, 421.07 $[M\text{-}F]^+$. Elemental analysis: Calcd. for $C_{25}H_{31}BF_2N_2O_2$ (440.33): C 68.19, H 7.10, N 6.36; found: C 67.89, H 6.89, N 6.32.

Methacrylate-BODIPY (3). **2** (0.25g, 0.57 mmol) was dissolved in dry THF (25 mL). NEt_3 (0.4 mL, 3 mmol) was added and the reaction was cooled to 0 ℃. Methacryloyl chloride (0.1 mL, 1 mmol) was then added and the reaction was

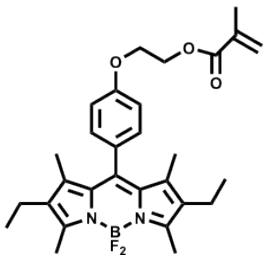

stirred overnight at room temperature. Diluted hydrochloric acid (40 mL) was added and the mixture was extracted with DCM (3 x 30 mL). After drying over Na_2SO_4 and evaporation of the solvent, the crude product was purified by column chromatography (hexane:ethyl acetate = 2:1). **3** was obtained as a red solid (0.13 g, 45 %). ^{1}H NMR ($CDCl_3$, 300 MHz), δ [ppm]: 7.18-7.13 (m, 2 H, phenyl-H), 7.02-6.98 (m, 2 H, phenyl-H), 6.17 (bs, 1 H, C=CH_2), 5.60 (bs, 1 H, C=CH_2), 4.54-4.51 (m, 2 H, CH^+-O-MMA), 4.29-4.26 (m, 2 H, phenyl-O-CH_2), 2.50 (s, 6 H, pyrrole-CH_2), 2.28 (q, J = 7.6 Hz, 4 H, pyrrole-C<u>H</u>2-CH3), 1.97 (s, 3 H, MMA-CH_3), 1.31 (s, 6 H, pyrrole-CH3), 0.96 (t, J = 7.6 Hz, pyrrole-CH_2-C<u>H</u>$_3$). MS (MALDI-TOF): m/z: 508.10 $[M]^+$, 489.07 $[M\text{-}F]^+$. Elemental analysis: Calcd. for $C_{39}H_{35}BF_2N_2O_3$ (508.41): C 68.51, H 6.94, N 5.51; found: C 68.62, H 6.89, N 5.42.

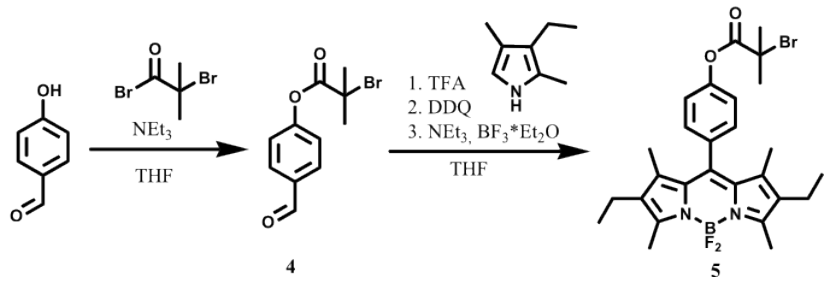

Figure 7.7: Synthesis of the BODIPY ATRP initiator (5).

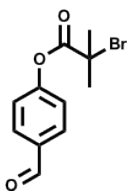

4-Formylphenyl 2-bromo-2methylpropanoate (4). 4-Hydroxybenzaldehyde (1.5 g, 12.3 mmol) was dissolved in dry THF (50 mL). NEt3 (6 mL, 43 mmol) was added and the reaction was cooled to 0 ℃. A solution of 2-bromo-2-methylpropanoate bromide (4.3 g, 1 mmol) in dry THF (10 mL) was then added and the reaction was stirred overnight at room temperature. Diluted hydrochloric acid (70 mL) was added and the mixture was extracted with DCM (3 x 50 mL). After drying over Na_2SO_4 and evaporation of the solvent, the crude product was purified by column chromatography (hexane:ethyl acetate = 5:4). **4** was obtained as a white (2.5 g, 75 %). ^{1}H NMR ($CDCl_3$, 300 MHz), δ [ppm]: 9.95 (s, 1 H, aldehyde-H), 7.91-7.87 (m, 2 H, phenyl-H), 7.28-7.25 (m, 2 H, phenyl-H), 2.04 (s, 6 H, CH_3).

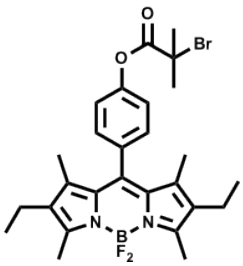

BODIPY ATRP initiator (5). **4** (0.58 g, 2.14 mmol) and 3-ethyl-2,4-dimethylpyrrole (0.58 g, 4.71 mmol) were dissolved in dry THF (60 mL). Ten drops of trifluoroacetic acid were added and the solution was stirred overnight at room temperature. A solution of DDQ (0.49 g, 2.14 mmol) in dry THF (20 mL) was added dropwise and the reaction was stirred for an additional 5 h. NEt_3 (9 mL, 64 mmol) was then added and the reaction was cooled to 0 ℃. BF_3*Et_2O (9 mL, 73 mmol) was added and the reaction was stirred overnight. The solvent was evaporated and the crude product was purified by column chromatography (hexane : ethyl acetate = 4:1). **5** was obtained as red solid (0.65 g, 56 %). ^{1}H NMR ($CDCl_3$, 300 MHz), δ [ppm]: 7.34-7.30 (m, 2 H, phenyl-H), 7.27-7.24 (m, 2 H, phenyl-H), 2.51 (s, 6 H, pyrrole-CH_3), 2.28 (q, J = 7.5 Hz, 4 H, pyrrole-CH_2-CH_3), 2.08 (s, 6 H, $C(CH_3)_2$), 1.31 (s, 6 H, pyrrole-CH_3), 0.96 (t, J = 7.5 Hz, pyrrole-CH_2-$C\underline{H}_3$). ^{13}C NMR (75 MHz, CD_2Cl_2), δ [ppm]:170.4, 154.3, 151.7, 139.6, 138.9, 134.0, 133.5, 131.1, 130.1, 122.4, 56.0, 30.8, 17.4, 14.8, 12.7, 12.0. MS (MALDI-TOF): m/z: 544.17 $[M]^+$, 525.11 $[M\text{-}F]^+$, 465.17 $[M\text{-}Br]^+$, 446.15 $[M\text{-}Br\text{-}F]^+$. Elemental analysis: Calcd. for $C_{27}H_{32}BBrF_2N_2O_2$ (545.27): C 59.47, H 5.92, N 5.14; found: C 59.70, H 5.21, N 5.10.

Typical procedures for the synthesis polymers from initiators **5**:

PMMA. A flame dried one-necked flask was charged with CuBr (8.8 mg, 62 μmol), PMDTA (13 μL, 62 μmol), **5** (16.9 mg, 31 μmol), methyl methacrylate (1 g, 10 mmol), and anisole (3 mL) under argon. After three freeze-pump-thaw circles, the polymerization was conducted at 65 ℃ for 1 h. The mixture was then diluted with THF (5 mL) and passed through a column of neutral alumina. The concentrated polymer solution was precipitated twice from methanol and then dried in vacuo.

PS. A flame dried one-necked flask was charged with CuBr (28.7, 0.2 mmol), 2,2'-bipyridine (31.2 mg, 0.2 mmol), **5** (54.5 mg, 0.1 mmol), styrene (1.5 g, 15 mmol), and anisole (2.5 mL) under argon. After three freeze-pump-thaw circles, the polymerization was conducted at 110 ℃ for 2 h. The mixture was then diluted with THF (5 mL) and passed through a column of neutral alumina. The concentrated polymer solution was precipitated twice from methanol and then dried in vacuo. The molecular weight of the polymers could be adjusted by variation of the reaction time.

Characterization

The molecular weight as well as the polydispersity index (PDI) of the polymers were measured by GPC with an Agilent Series 1260 device equipped with a PSS SECcurity pump and a UV detector at 488 nm wavelength (1260 VWD). The UV detector was chosen since it provides detection based on the absorption of the attached BODIPY dye which makes it comparable to what is detected in the FCS measurements. Three columns in a row (SDV) comprising pore sizes of 10^5, 10^3 and 50 nm respectively were used. THF was used as an eluent at a flow rate of 1.0 mL/min and at a temperature of 30 ℃. Calibration curves were measured with PS or PMMA as reference for the PS and PMMA samples, respectively. Additionally all GPC traces were fitted with a Schulz-Zimm distribution function (eq. 7.9) as shown in figure 7.8.

7.4.4. Synthesis of the polymers by free-radical polymerization

Materials

Toluene (Sigma-Aldrich, 99.7 %), methanol (Fluka, 99.99 %), and the fluorescent dye MMA-BODIPY were used without further purification. Styrene (Merck, 99 %) was purified on a column packed with neutral aluminum oxide (Merck) before use. The initiator 2,2'-azobis(2-methylpropionitrile) (AIBN, Fluka, 98 %) was recrystallized from methanol prior to use.

Synthesis

The polymer PS-III was synthesized by free radical polymerization in solution. 0.1 mg AIBN and 10 mg MMA-BODIPY were dissolved in 500 mg styrene and 500 μ L toluene. Argon was bubbled through the solution for 5 min. Afterwards, the temperature was increased to 72 ℃while stirring at 500 rpm for 100 h. Subsequently, the viscous polymer solution was precipitated into 200 mL methanol, filtrated and

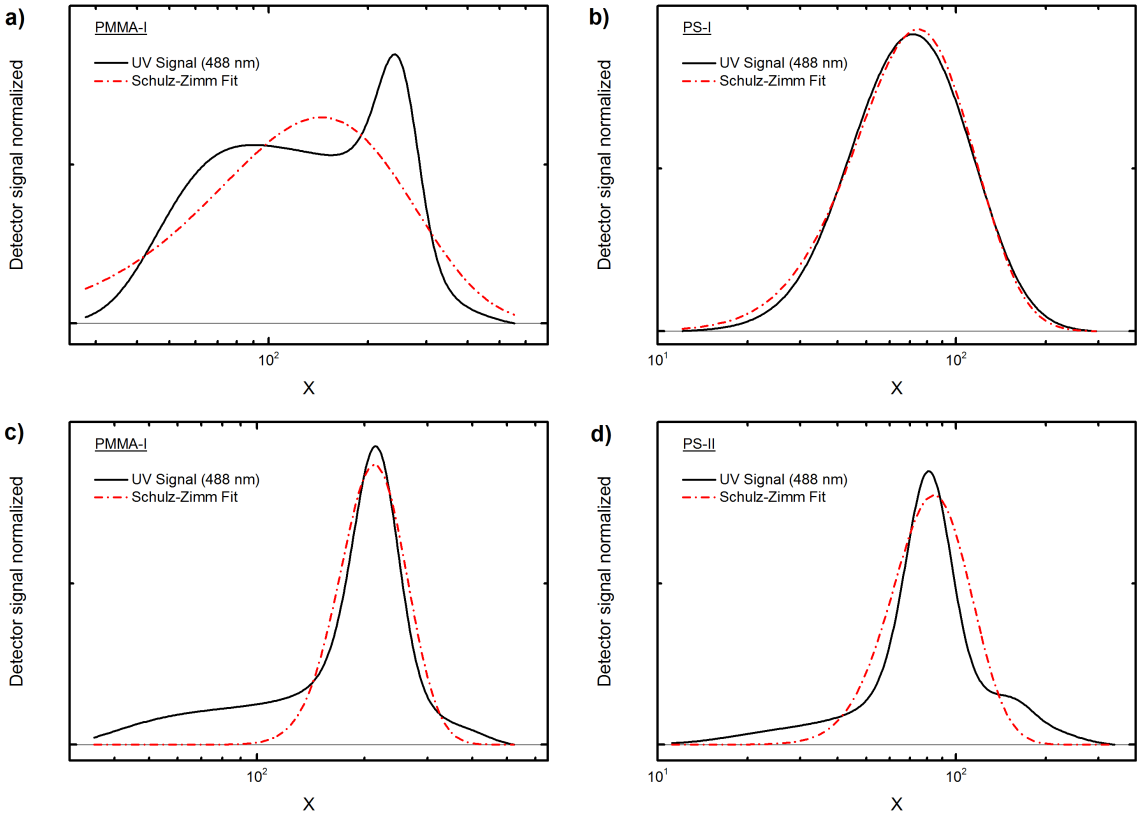

Figure 7.8: GPC traces (straight line) and Schulz-Zimm Fits (eq. 7.9) of BODIPY labelled PMMA and PS: PMMA-I (a), PMMA-II (c), PS-I (b), PS-II (d) and PS-II (d) (UV detector).

dissolved in toluene again. After precipitation in methanol, the polymer was dried in vacuo at 60 ℃overnight.

Characterization

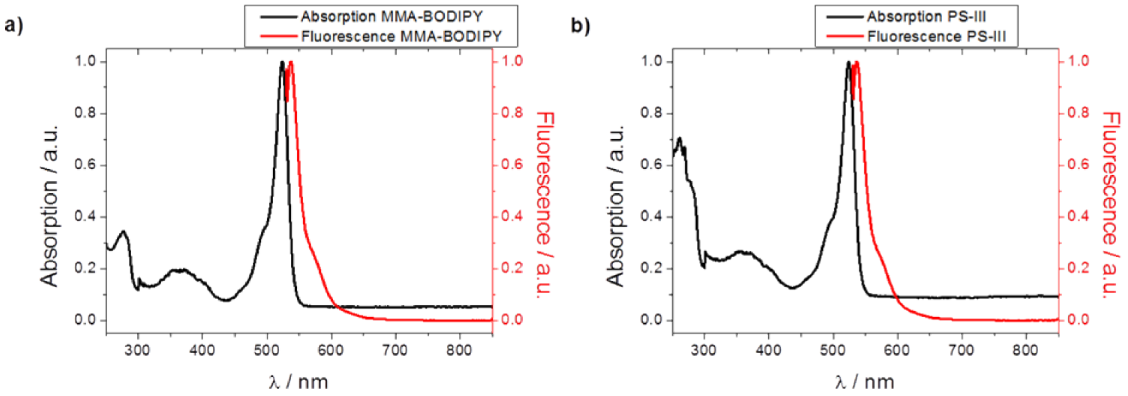

Figure 7.9: The fluorescence of the dye MMA-BODIPY (a) and PS-III remains after polymerization.

GPC characterization was similar to the characterization of the other polymer samples (see above). The spectra of the free dye and of the polymer were measured on a Tecan Plate Reader Infinite M1000 in THF solution (see Figure 7.9). For the fluorescence spectra, an excitation wavelength of 524 nm was employed.

7.4.5. Brownian dynamics simulations

Algorithm

The previously proposed fast TIR-FCS simulation algorithm[259] was adapted for the present FCS case. Briefly, Schulz-Zimm distribution (eq. 7.9) was used as a probability function for the generation of a chain with degree of polymerization X. To model the statistical labeling every 100th repeat unit was set as carrying a fluorophore, thus allowing only integer numbers of fluorophores per chain. This chain was then considered as a point like particle with diffusion coefficient given by eq. 7.6 (main text) and fluorescent brightness essentially linearly proportional to X. By generating a high number ($\sim 2 \cdot 10^5$) of such chains/particles at initial 3D positions assigned with a probability density proportional on the FCS 3D Gaussian observation volume, propagating them with Brownian dynamics procedure and averaging

their individual contributions[259], highly accurate auto-correlation curve is created. Figure 7.10 shows the generated FCS autocorrelation curves for the simulated PS polymer samples having the same number average degree of polymerization $\langle X \rangle = 1000$ and polydispersity indecies PDI of 1.0, 1.5, 2.0 and 2.5 respectiveley. The fits with the polydisperse (eq. 7.8 in the main text) and the monodisperse (eq. 7.2 in the main text) models and the corresponding residuals are also shown.

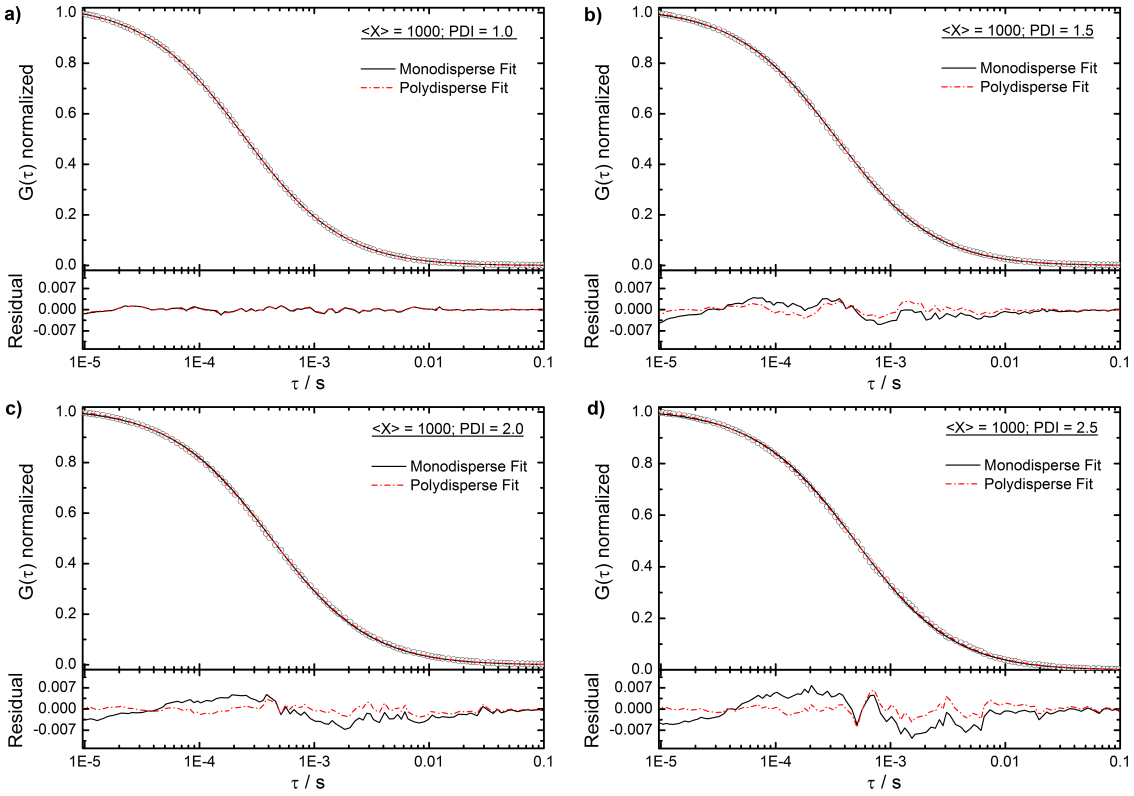

Figure 7.10: Simulated autocorrelation curves (symbols) of PS polymers with an average degree of polymerization of 1000 and polydispersity indices PDI of 1.0 (a), 1.5 (b), 2.0 (c) and 2.5 (d) in toluene solutions. The corresponding fits using the monodisperse model, eq. 7.2 (straight lines) and the polydisperse model, eq. 7.8 (dash dotted lines) are also shown. The low panels show the respective residuals.

7.4.6. Additional FCS data of sample PS-III

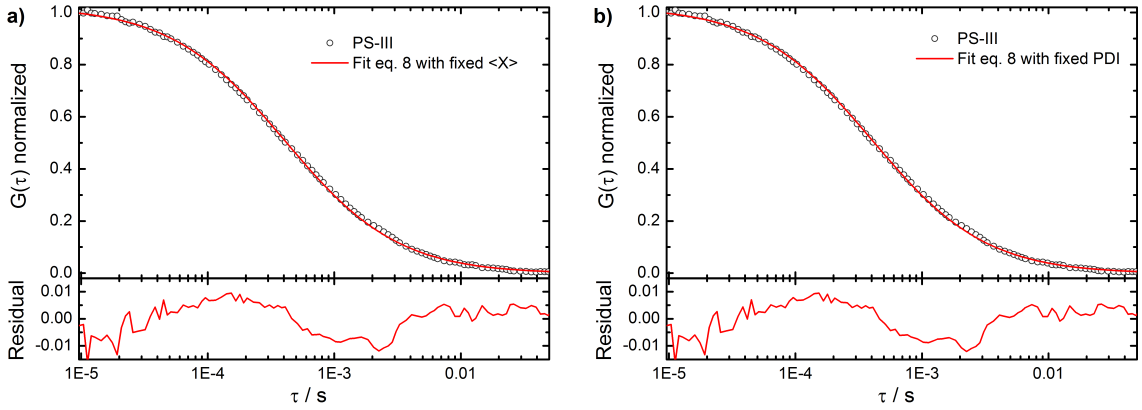

Figure 7.11: Experimental autocorrelation curves (symbols) of sample PS-III fitted with eq. 7.8 (line) by either fixing $\langle X \rangle$ (a) or the PDI (b) to their GPC-value.

Figure 7.11 shows the fits of eq. 7.8 to the experimental autocorrelation curve of sample PS-III while fixing either $\langle X \rangle$ to 1863 or the PDI to 2.49 which corresponds to the measured GPC-values. The fit yields $PDI_{\mathrm{FCS}} = 2.60 \pm 0.05$ or $\langle X_{\mathrm{FCS}} \rangle = 1960 \pm 47$, respectiveley.

7.5. Acknowledgment

The financial support from DFG (SPP 1066, Q2) is gratefully acknowledged. R. H. Staff gratefully acknowledges financial support from the Fonds der Chemischen Industrie.

8. Conclusions

In this thesis I studied the interaction and exchange between polymeric colloids. The main experimental technique I used was DC FCCS. Two different processes were studied. One is the preparation of polymeric nanoparticles from emulsion droplets and the second is the dynamic equilibrium exchange of building molecules between amphiphilic diblock copolymer micelles.

Coalescence is believed to be a major reason for the huge size distribution often observed in the nanoparticles suspension formulated by the SEED process. So far, only DLS was used to study the influence of coalescence which was found to be not suitable since the determined diameters of the droplets/particles depend of diluent and dilution. Other methods like, FCS, Zeta-potential measurements, cryo-TEM and FRET hint towards a minor role of coalescence but do not allow its quantification. However, DC FCCS was found to be a fast and reliable method to directly and unambiguously quantify coalescence. By additionally applying reverse Monte Carlo simulations I could show that coalescence does not play an important role during the SEED process and is not the reason for the huge size distribution observed in the final nanoparticles suspension. This hints towards the need of increased efforts to enhance the fabrication mechanism itself to reduce polydispersity. Furthermore, to corroborate the reliability of DC FCCS experiments for coalescence determination, I studied two other procedures for nanoparticles preparation. The results show that coalescence only plays a minor role within the preparation of polystyrene nanoparticles by minimemulsion polymerization. On the other hand, during the formation of nanocapsules from alkoxysilanes by interfacial polycondensation coalescence indeed plays a role.

The second colloidal system I studied were amphiphilic diblock copolymer micelles. DC FCCS was able to track the exchange and moreover quantify the exchange kinetics of building molecules between the micelles in thermodynamic equilibrium. So far, for such experiments only TR-SANS was used. A major advantage of DC FCCS is here, that it uses tabletop equipment and fluorescence labeling which makes the approach accessible to a large research community. The linear-brush block copolymer PS-POEGMA was chosen as a model system forming micelles compromis-

ing a short and bulky corona. Within the framework of earlier reported theories [37,45] I could verify that single molecule exchange is the dominating exchange mechanism. Moreover, by studying the exchange in different solvents and at various temperatures I was able to quantify the degree of swelling of the PS micelle core when exchange is observed below the nominal glass transition of the core forming PS. This shows, that solvent quality is of fastidious importance and allows extensive tuning of the exchange kinetics.

A property that the fabricated nanoparticles and the synthesized block copolymers have in common is polydispersity. I explored the effect of polydispersity on FCS measurements using fluorescently labeled polymers as model system. The polymers where either end-labeled with one dye per chain or statistically copolymerized with monomer bearing a fluorescent dye. A Schulz-Zimm distibution was introduced into the classical monodisperse FCS model directly accounting for polydispersity of the polymers and their fluorescence brightness distribution. This approach allowed evaluating the PDI by fitting the experimental FCS curves and yields results similar to GPC if the shape of the molar mass distribution does not deviate too strong from the assumed one. Furthermore, I used Brownian dynamics simulation to simulate ideal experiments and explore the range of validity of the new model. The results show the danger of fitting when experimental autocorrelation curves of a polydisperse system are fitted with the standard monodisperse model. This is commonly done throughout existing studies and might lead to false interpretation of the data when the influence of brightness distribution is not properly taken into account. In my case a fitting of the polymers bearing one and thus a constant number of dyes per chain with the monodisperse model will provide a value very close to the number average molecular weight of the molar mass distribution of the polymer. In contrast having a statistically labeled polymer the fit will yield a value even larger than the weight average molecular weight. Moreover, FCS has the capability not only to resolve size polydispersity of polymers but also to determine their fluorescence brightness distribution.

Part III.

Bibliography & appendix

A. Bibliography

[1] Nikiforow, I., Adams, J., König, A. M., Langhoff, A., Pohl, K., Turshatov, A., and Johannsmann, D. *Langmuir* **26**(16), 13162–13167 (2010).

[2] Facchetti, A. *Chem. Mater.* **23**(3), 733–758 (2011).

[3] Liu, C., Li, F., Ma, L.-P., and Cheng, H.-M. *Adv. Mater.* **22**(8), 28–62 (2010).

[4] Katti, K. S. *Colloid. Surface. B* **39**(3), 133 – 142 (2004).

[5] Langer, R. and Peppas, N. A. *AIChE Journal* **49**(12), 2990–3006 (2003).

[6] Kedar, U., Phutane, P., Shidhaye, S., and Kadam, V. *Nanomedicine* **6**(6), 714 – 729 (2010).

[7] Elsabahy, M. and Wooley, K. L. *Chem. Soc. Rev.* **41**, 2545–2561 (2012).

[8] Kim, S. A. and Schwille, P. *Curr. Opin. Neurobiol.* **13**(5), 583 – 590 (2003).

[9] Hess, S. T., Huang, S., Heikal, A. A., and Webb, W. W. *Biochemistry* **41**(3), 697–705 (2002).

[10] Koynov, K. and Butt, H.-J. *Curr. Opin Colloid In.* **17**(6), 377 – 387 (2012).

[11] Woll, D. *RSC Adv.* **4**, 2447–2465 (2014).

[12] Rigler, P. and Meier, W. *J. Am. Chem. Soc.* **128**(1), 367–373 (2006).

[13] Jaskiewicz, K., Larsen, A., Lieberwirth, I., Koynov, K., Meier, W., Fytas, G., Kroeger, A., and Landfester, K. *Angew. Chem. Int. Edit.* **51**(19), 4613–4617 (2012).

[14] Nuhn, L., Hirsch, M., Krieg, B., Koynov, K., Fischer, K., Schmidt, M., Helm, M., and Zentel, R. *ACS Nano* **6**(3), 2198–2214 (2012).

[15] Bonné, T. B., Ludtke, K., Jordan, R., Stepanek, P., and Papadakis, C. M. *Colloid Polym. Sci.* **282**(12), 1425–1425 (2004).

[16] Bonné, T. B., Papadakis, C. M., Ludtke, K., and Jordan, R. *Colloid Polym. Sci.* **285**(5), 491–497 (2007).

[17] Bonné, T. B., Ludtke, K., Jordan, R., and Papadakis, C. M. *Macromol. Chem. Phys.* **208**(13), 1402–1408 (2007).

[18] Zander, C., Enderlein, J., and Keller, R. A. *Single Molecule Detection in Solution - Methods and Applications*. Wiley-VCH, (2002).

[19] Kok, C. M. and Rudin, A. *Makromol. Chem.-Rapid* **2**(11), 655–659 (1981).

[20] Rubinstein, M. and Colby, R. H. *Polymer Physics*. Oxford University Press,

USA, (2003).

[21] Schwille, P., MeyerAlmes, F. J., and Rigler, R. *Biophys. J.* **72**(4), 1878–1886 (1997).

[22] Burton, G. W. and O'Farrel, C. P. *J. Elastom. Plast.* **9**, 94–101 (1977).

[23] Vanderhoff, J. W., El-Aasser, M. S., and Ugelstad, J. December (1979).

[24] Staff, R. H., Landfester, K., and Crespy, D. *Adv. Polym. Sci.* **262**, 329–344 (2013).

[25] Staff, R. H., Rupper, P., Lieberwirth, I., Landfester, K., and Crespy, D. *Soft Matter* **7**(21), 10219–10226 (2011).

[26] Staff, R. H., Lieberwirth, I., Landfester, K., and Crespy, D. *Macromol. Chem. Phys.* **213**(3), 351–358 (2012).

[27] Staff, R. H., Gallei, M., Mazurowski, M., Rehahn, M., Berger, R., Landfester, K., and Crespy, D. *ACS Nano* **6**(10), 9042–9049 (2012).

[28] Urban, M., Musyanovych, A., and Landfester, K. *Macromol. Chem. Phys.* **210**(11), 961–970 (2009).

[29] Mistlberger, G., Medina-Castillo, A. L., Borisov, S. M., Mayr, T., Fernández-Gutiérrez, A., Fernandez-Sanchez, J. F., and Klimant, I. *Microchim. Acta* **172**(3), 299–308 (2011).

[30] Quintanar-Guerrero, D., Allémann, E., Fessi, H., and Doelker, E. *Drug Dev. Ind. Pharm.* **24**(12), 1113–1128 (1998).

[31] Freiberg, S. and Zhu, X. *Int. J. Pharm.* **282**(1-2), 1–18 September (2004).

[32] Desgouilles, S., Vauthier, C., Bazile, D., Vacus, J., Grossiord, J.-L., Veillard, M., and Couvreur, P. *Langmuir* **19**(22), 9504–9510 (2003).

[33] Fryd, M. M. and Mason, T. G. *J. Phys. Chem. Lett.* **1**(23), 3349–3353 (2010).

[34] Schaeffel, D., Staff, R. H., Butt, H. J., Landfester, K., Crespy, D., and Koynov, K. *Nano Lett.* **12**(11), 6012–6017 (2012).

[35] Staff, R. H., Schaeffel, D., Turshatov, A., Donadio, D., Butt, H. J., Landfester, K., Koynov, K., and Crespy, D. *Small* **9**(20), 3514–3522 (2013).

[36] Aniansson, E. A. G., Wall, S. N., Almgren, M., Hoffmann, H., Kielmann, I., Ulbricht, W., Zana, R., Lang, J., and Tondre, C. *J. Phys. Chem.* **80**(9), 905–922 (1976).

[37] Halperin, A. and Alexander, S. *Macromolecules* **22**(5), 2403–2412 (1989).

[38] Dormidontova, E. E. *Macromolecules* **32**(22), 7630–7644 (1999).

[39] Kataoka, K., Harada, A., and Nagasaki, Y. *Adv. Drug Delivery Rev.* **47**(1),

113–131 (2001).

[40] Batrakova, E. V. and Kabanov, A. V. *J. of Control. Release* **130**(2), 98–106 (2008).

[41] Matsumura, Y. and Kataoka, K. *Cancer Sci.* **100**(4), 572–579 (2009).

[42] Prochazka, K., Bednar, B., Mukhtar, E., Svoboda, P., Trnena, J., and Almgren, M. *J. Phys. Chem.* **95**(11), 4563–4568 (1991).

[43] Jain, S. and Bates, F. S. *Macromolecules* **37**(4), 1511–1523 (2004).

[44] Lund, R., Willner, L., Stellbrink, J., Lindner, P., and Richter, D. *Phys. Rev. Lett.* **104**(4) (2010).

[45] Choi, S. H., Lodge, T. P., and Bates, F. S. *Phys. Rev. Lett.* **104**(4) (2010).

[46] Schaeffel, D., Kreyes, A., Zhao, Y., Landfester, K., Butt, H.-J., Crespy, D., and Koynov, K. *ACS Macro Lett.* **3**(0), 428–432 (2014).

[47] Starchev, K., Buffle, J., and Perez, E. *J. Colloid Interf. Sci.* **213**(2), 479–487 (1999).

[48] Pal, N., Verma, S. D., Singh, M. K., and Sen, S. *Anal. Chem.* **83**(20), 7736–7744 (2011).

[49] Sengupta, P., Garai, K., Balaji, J., Periasamy, N., and Maiti, S. *Biophys. J.* **84**(3), 1977–1984 (2003).

[50] Provencher, S. W. *Makromol. Chem.* **180**(1), 201–209 (1979).

[51] Provencher, S. W. *Comput. Phys. Commun.* **27**(3), 229–242 (1982).

[52] Provencher, S. W. *Comput. Phys. Commun.* **27**(3), 213–227 (1982).

[53] Magde, D., Webb, W. W., and Elson, E. *Phys. Rev. Lett.* **29**(11), 705 (1972).

[54] Magde, D., Elson, E. L., and Webb, W. W. *Biopolymers* **13**(1), 29–61 (1974).

[55] Koppel, D. E., Axelrod, D., Schlessinger, J., Elson, E. L., and Webb, W. W. *Biophys. J.* **16**(11), 1315–1329 (1976).

[56] Elson, E. L. and Magde, D. *Biopolymers* **13**(1), 1–27 (1974).

[57] Ehrenberg, M.and Rigler, R. *Chem. Phys.* **4**(3), 390–401 (1974).

[58] Aragon, S. R. and Pecora, R. *Biopolymers* **14**(1), 119–137 (1975).

[59] Magde, D., Webb, W. W., and Elson, E. L. *Biopolymers* **17**(2), 361–376 (1978).

[60] Rigler, R., Mets, U., Widengren, J., and Kask, P. *Eur. Biophys. J. Biophy.* **22**(3), 169–175 (1993).

[61] Webb, R. H. *Rep. Prog. Phys.* **59**(3), 427–471 (1996).

[62] Schwille, P. and Haustein, E. *Fluorescence Correlation Spectroscopy: An In-*

troduction to its Concepts and Applications.

[63] Schwille, P. *Flourescence Correlation Spectroscopy: Theory and Applications.* Springer, Berlin, (2001).

[64] Rigler, R. and Elson, E. *Fluorescence correlation spectroscopy : theory and applications.* Springer series in chemical physics, 65. Springer, Berlin; New York, (2001).

[65] Chen, Y., Muller, J. D., So, P. T. C., and Gratton, E. *Biophys. J.* **77**(1), 553–567 (1999).

[66] Kask, P., Palo, K., Ullmann, D., and Gall, K. *P. Natl. Acad. Sci. USA* **96**(24), 13756–13761 (1999).

[67] Muller, J. D., Chen, Y., and Gratton, E. *Biophys. J.* **78**(1), 474–486 (2000).

[68] Perroud, T. D., Huang, B., and Zare, R. N. *Biophys. J.* **86**(1), 157 (2004).

[69] Perroud, T. D., Huang, B., and Zare, R. N. *Chem.Phys.Chem.* **6**(5), 905–912 (2005).

[70] Palo, K., Metz, U., Jager, S., Kask, P., and Gall, K. *Biophys. J.* **79**(6), 2858–2866 (2000).

[71] Lakowicz, J. R. *Principles of Fluorescence Spectroscopy.* Springer, (2006).

[72] Atkins, P. *Physical Chemistry.* Oxford University Press, (1998).

[73] Schwille, P., Bieschke, J., and Oehlenschlager, F. *Biophys. Chem.* **66**(2-3), 211–228 (1997).

[74] Qian, H. and Elson, E. L. *Appl. Optics* **30**(10), 1185–1195 (1991).

[75] Starchev, K., Zhang, J., and Buffle, J. *J. Colloid Interf. Sci.* **203**(1), 189 – 196 (1998).

[76] Korlach, J., Schwille, P., Webb, W. W., and Feigenson, G. W. *P. Natl. Acad. Sci. USA* **96**(17), 9966–9966 (1999).

[77] Kohler, R. H., Schwille, P., Webb, W. W., and Hanson, M. R. *J. Cell Sci.* **113**(22), 3921–3930 (2000).

[78] Gosch, M., Blom, H., Holm, J., Heino, T., and Rigler, R. *Anal. Chem.* **72**(14), 3260–3265 (2000).

[79] Thompson, N. L. and Axelrod, D. *Biophys. J.* **33**(2), 183 (1981).

[80] Thompson, N. L., Burghardt, T. P., and Axelrod, D. *Biophys. J.* **33**(3), 435–454 (1981).

[81] Thompson, N. L. and Axelrod, D. *Biophys. J.* **37**(2), A355–A355 (1982).

[82] Starr, T. E. and Thompson, N. L. *Biophys. J.* **80**(3), 1575–1584 (2001).

[83] Lieto, A. M., Cush, R. C., and Thompson, N. L. *Biophys. J.* **85**(5), 3294–3302 (2003).

[84] Hassler, K., Leutenegger, M., Rigler, P., Rao, R., Rigler, R., Gosch, M., and Lasser, T. *Opt. Express* **13**(19), 7415–7423 (2005).

[85] Widengren, J., Mets, U., and Rigler, R. *J. Phys. Chem.* **99**(36), 13368–13379 (1995).

[86] Schwille, P., Kummer, S., Heikal, A. A., Moerner, W. E., and Webb, W. W. *P. Natl. Acad. Sci. USA* **97**(1), 151–156 (2000).

[87] Kask, P., Piksarv, P., Mets, U., Pooga, M., and Lippmaa, E. *Eur. Biophys. J. Biophy.* **14**(4), 257–261 (1987).

[88] Ehrenberg, M. and Rigler, R. *Q. Rev. Biophys.* **9**(1), 69–81 (1976).

[89] Kask, P., Piksarv, P., Pooga, M., Mets, U., and Lippmaa, E. *Biophys. J.* **55**(2), 213–220 (1989).

[90] Widengren, J., Mets, U., and Rigler, R. *Chem. Phys.* **250**(2), 171–186 (1999).

[91] Tsay, J. M., Doose, S., and Weiss, S. *J. Am. Chem. Soc.* **128**(5), 1639–1647 (2006).

[92] Dorfschmid, M., Mullen, K., Zumbusch, A., and Woll, D. *Macromolecules* **43**(14), 6174–6179 (2010).

[93] Kimble, H. J., Dagenais, M., and Mandel, L. *Phys. Rev. Lett.* **39**(11), 691–695 (1977).

[94] Kask, P., Piksarv, P., and Mets, U. *Eur. Biophys. J. Biophy.* **12**(3), 163–166 (1985).

[95] Basche, T., Moerner, W. E., Orrit, M., and Talon, H. *Phys. Rev. Lett.* **69**(10), 1516–1519 (1992).

[96] Felekyan, S., Kuhnemuth, R., Kudryavtsev, V., Sandhagen, C., Becker, W., and Seidel, C. A. M. *Rev. Sci. Instrum.* **76**(8) (2005).

[97] Brown, R. H. and Twiss, R. Q. *Nature* **178**(4541), 1046–1048 (1956).

[98] Brown, R. H. and Twiss, R. Q. *Nature* **178**(4548), 1447–1448 (1956).

[99] Brown, R. H. and Twiss, R. Q. *Nature* **177**(4497), 27–29 (1956).

[100] Wahl, M., Rahn, H. J., Gregor, I., Erdmann, R., and Enderlein, J. *Rev. Sci. Instrum.* **78**(3) (2007).

[101] Bohmer, M., Wahl, M., Rahn, H. J., Erdmann, R., and Enderlein, J. *Chem. Phys. Lett.* **353**(5-6), 439–445 (2002).

[102] Brinkmeier, M., Dorre, K., Stephan, J., and Eigen, M. *Anal. Chem.* **71**(3),

609–616 (1999).

[103] Schwille, P. *Cross-correlation analysis in FCS*, volume 1, 360–378. Springer Verlag (2001).

[104] Bacia, K. and Schwille, P. *Nat. Protoc.* **2**(11), 2842–2856 (2007).

[105] Weisshart, K., Jungel, V., and Briddon, S. J. *Curr. Pharm. Biotechno.* **5**(2), 135–154 (2004).

[106] Ries, J., Bayer, M., Csucs, G., Dirkx, R., Solimena, M., Ewers, H., and Schwille, P. *Opt. Express* **18**(11), 11073–11082 (2010).

[107] Cosgrove, T. *Colloid Science Principles, methods and applications.* Wiley VCH, (2010).

[108] Dörfler, H.-D. *Grenzflächen und kolloid-disperse Systeme.* Springer, Berlin, (2002).

[109] Gibbs, J. W. *Trans. Connect. Acad. Sci.* **3**, 108–248 (1876).

[110] Gibbs, J. W. *Trans. Connect. Acad. Sci.* **16**, 343–524 (1878).

[111] Butt, H.-J., Graf, K., and Kappl, M. *Physics and Chemistry of Interfaces.* Wiley, Weinheim, 2. edition, (2006).

[112] Overbeek, J. *J. Colloid Interf. Sci.* , 408–422 (1977).

[113] Toro-Mendoza, J., Lozsan, A., Garcia-Sucre, M., Castellanos, A. J., and Urbina-Villalba, G. *Phys. Rev. E* **81**(1) (2010).

[114] Ostwald, W. *Z. Phys. Chem.* **34**, 495 (1900).

[115] Hamaker, H. C. *Physica* **4**, 1058–1072 (1937).

[116] London, F. *Z. Phys.* **63**(3-4), 245–279 (1930).

[117] Derjaguin, B. *Acta Physicochim. Urs.* **10**(3), 333–346 (1939).

[118] Cao, G. *Nanostructures & Nanomaterials: Synthesis, Properties & Application.* Imperial College Press, (2004).

[119] Asakura, S. and Oosawa, F. *J. Polym. Sci.* **33**(126), 183–192 (1958).

[120] Landfester, K. *Macromol. Rapid Commun.* **22**(12), 896–936 (2001).

[121] Landfester, K. *Ann. Rev. Mater. Res.* **36**, 231–279 (2006).

[122] Lagaly, G., Schulz, O., and Zimehl, R. *Dispersionen und Emulsionen.* Steinkopf, Darmstadt, (1997).

[123] Wilde, P., Mackie, A., Husband, F., Gunning, P., and Morris, V. *Adv. Colloid Interfac.* **108**, 63–71 (2004).

[124] Tauer, K. In *Colloids and Colloids Assemblies.* Wiley (2004).

[125] Asua, J. M. *J. Polym. Sci. A Polym. Chem.* **42**(5), 1025–1041 (2004).

[126] Chern, C. *Prog. Polym. Sci.* **31**(5), 443–486 May (2006).

[127] Pavel, F. M. *J. Dispersion Sci. Technol.* **25**(1), 1–16 December (2004).

[128] Chow, P. Y. and Gan, L. M. In *Advances in Polymer Science,* Okubo, M., editor, volume 175, 257–298. Springer Berlin Heidelberg (2005).

[129] Landfester, K. *Macromol. Symp.* **150**(1), 171–178 (2000).

[130] Landfester, K. *Annu. Rev. Mater. Res.* **36**(1), 231–279 (2006).

[131] Landfester, K., Bechthold, N., Forster, S., and Antonietti, M. *Macromol. Rapid Comm.* **20**(2), 81–84 (1999).

[132] Crespy, D. and Landfester, K. *Beilstein J. Org. Chem.* **6**, 1132–1148 (2010).

[133] Wang, J. and Schwendeman, S. P. *J. Pharm. Sci.* **88**(10), 1090–1099 (1999).

[134] Mainardes, R. M. and Evangelista, R. C. *J. Microencapsul.* **22**(1), 13–24 (2005).

[135] Sansdrap, P. and Moës. *Int. J. Pharm.* **98**(1-3), 157–164 August (1993).

[136] Tanford, C. *Science* **200**(4345), 1012–1018 (1978).

[137] Riess, G. *Prog. Polym. Sci.* **28**(7), 1107–1170 (2003).

[138] Musolf, O. *Chemisches Schalten in Compositen aus Siliciumdioxid und Azobenzol-Guppen tragenden Tensiden.* PhD thesis, Universität Hannover, (2004).

[139] Zana, R. *Langmuir* **12**(5), 1208–1211 (1996).

[140] Mukerjee, P., Mysels, K. J., and Kapauan, P. *J. Phys. Chem.* **71**(13), 4166 (1967).

[141] Maiti, K., Mitra, D., Guha, S., and Moulik, S. P. *J. Mol. Liq.* **146**(1-2), 44–51 (2009).

[142] Hoffmann, H., Tagesson, B., and Ulbricht, W. *Ber. Bunsen. Phys. Chem.* **83**(2), 148–155 (1979).

[143] Klevens, H. B. *J. Am. Oil Chem. Soc.* **30**(2), 74–80 (1953).

[144] Esselink, F. J., Dormidontova, E., and Hadziioannou, G. *Macromolecules* **31**(9), 2925–2932 (1998).

[145] Lam, Y. M., Grigorieff, N., and Goldbeck-Wood, G. *Phys. Chem. Chem. Phys.* **1**(14), 3331–3334 (1999).

[146] Lee, M., Cho, B. K., and Zin, W. C. *Chem. Rev.* **101**(12), 3869–3892 (2001).

[147] Mueller, W., Koynov, K., Fischer, K., Hartmann, S., Pierrat, S., Basche, T., and Maskos, M. *Abstr. Pap. Am. Chem. S.* **237** (2009).

[148] Zhulina, E. B. and Borisov, O. V. *Macromolecules* **45**(11), 4429–4440 (2012).

[149] Halperin, A. *Macromolecules* **20**(11), 2943–2946 (1987).

[150] Zhulina, Y. B. and Birshtein, T. M. *Vysokomol. Soedin. B* **28**(10), 773–778 (1986).

[151] Alexander, S. *J. Phys.-Paris* **38**(8), 977–981 (1977). Ds743 Times Cited:369 Cited References Count:7.

[152] Degennes, P. G. *Macromolecules* **13**(5), 1069–1075 (1980).

[153] Daoud, M. and Cotton, J. P. *J. Phys.-Paris* **43**(3), 531–538 (1982).

[154] Birshtein, T. M. and Zhulina, E. B. *Polymer* **25**(10), 1453–1461 (1984).

[155] Leibler, L., Orland, H., and Wheeler, J. C. *J. Chem. Phys.* **79**(7), 3550–3557 (1983).

[156] Aniansson, E. A. G. and Wall, S. N. *J. Phys. Chem.* **78**(10), 1024–1030 (1974).

[157] Aniansson, E. A. G. and Wall, S. N. *J. Phys. Chem.* **79**(8), 857–858 (1975).

[158] Li, Z. L. and Dormidontova, E. E. *Macromolecules* **43**(7), 3521–3531 (2010).

[159] Tondré, C., Lang, J., and Zana, R. *J. Colloid Interf. Sci.* **52**(2), 372–379 (1975).

[160] Kramers, H. A. *Physica* **7**, 284–304 (1940).

[161] Lund, R., Willner, L., Pipich, V., Grillo, I., Lindner, P., Colmenero, J., and Richter, D. *Macromolecules* **44**(15), 6145–6154 (2011).

[162] Rouse, P. E. *J. Chem. Phys.* **21**(7), 1272–1280 (1953).

[163] Brigger, I., Dubernet, C., and Couvreur, P. *Adv. Drug Deliver. Rev.* **54**(5), 631–651 (2002).

[164] Peer, D., Karp, J. M., Hong, S., FaroKHzad, O. C., Margalit, R., and Langer, R. *Nat. Nanotechnol.* **2**(12), 751–760 (2007).

[165] Davis, M. E., Chen, Z., and Shin, D. M. *Nat. Rev. Drug Discov.* **7**(9), 771–782 (2008).

[166] Arico, A. S., Bruce, P., Scrosati, B., Tarascon, J. M., and Van Schalkwijk, W. *Nat. Mater.* **4**(5), 366–377 (2005).

[167] Crespy, D., Zuber, S., Turshatov, A., Landfester, K., and Popa, A.-M. *J. Polym. Sci. A Polym. Chem.* **50**(6), 1043–1048 (2012).

[168] Lovell, P. A. and El-Aasser, M. S. *Emulsion Polymerization and Emulsion Polymers*. John Wiley & Sons, (1997).

[169] Imhof, A. and Pine, D. J. *Nature* **389**(6654), 948–951 (1997).

[170] Capek, I. *Adv. Colloid Interfac.* **110**(1-2), 49–74 (2004).

[171] Gurny, R., Peppas, N. A., Harrington, D. D., and Banker, G. S. *Drug. Dev.*

Ind. Pharm. **7**(1), 1–25 (1981).

[172] Bodmeier, R. and Chen, H. G. *J. Control. Release* **12**(3), 223–233 (1990).

[173] Zhao, Y., Fickert, J., Landfester, K., and Crespy, D. *Small* **8**(9), 2954–2958 (2012).

[174] Schwille, P. *Cell Biochem. Biophys.* **34**(3), 383–408 (2001).

[175] Elson, E. L. *Biophys. J.* **101**(12), 2855–2870 (2011).

[176] Borsch, M., Turina, P., Eggeling, C., Fries, J. R., Seidel, C. A. M., Labahn, A., and Graber, P. *FEBS Lett.* **437**(3), 251–254 (1998).

[177] Ries, J. and Schwille, P. *Phys. Chem. Chem. Phys.* **10**(24), 3487–3497 (2008).

[178] Sukhishvili, S. A., Chen, Y., Muller, J. D., Gratton, E., Schweizer, K. S., and Granick, S. *Macromolecules* **35**(5), 1776–1784 (2002).

[179] Enderlein, J. *Phys. Rev. Lett.* **108**(10) (2012).

[180] Zhao, J. and Granick, S. *J. Am. Chem. Soc.* **126**(20), 6242–6243 (2004).

[181] Wong, J. S. S., Hong, L. A., Bae, S. C., and Granick, S. *Macromolecules* **44**(8), 3073–3076 (2011).

[182] Yang, Q. B. and Zhao, J. *Langmuir* **27**(19), 11757–11760 (2011).

[183] Grabowski, C. A. and Mukhopadhyay, A. *Macromolecules* **41**(16), 6191–6194 (2008).

[184] Liu, R. G., Gao, X., Adams, J., and Oppermann, W. *Macromolecules* **38**(21), 8845–8849 (2005).

[185] Woell, D., Uji-I, H., Schnitzler, T., Hotta, J. I., Dedecker, P., Herrmann, A., De Schryver, F. C., Muellen, K., and Hofkens, J. *Angew. Chem. Int. Edit.* **47**(4), 783–787 (2008).

[186] Zettl, U., Hoffmann, S. T., Koberling, F., Krausch, G., Enderlein, J., Harnau, L., and Ballauff, M. *Macromolecules* **42**(24), 9537–9547 (2009).

[187] Cherdhirankorn, T., Best, A., Koynov, K., Peneva, K., Muellen, K., and Fytas, G. *J. Phys. Chem. B* **113**(11), 3355–3359 (2009).

[188] Kalwarczyk, T., Ziebacz, N., Bielejewska, A., Zaboklicka, E., Koynov, K., Szymanski, J., Wilk, A., Patkowski, A., Gapinski, J., Butt, H. J., and Holyst, R. *Nano Lett.* **11**(5), 2157–2163 (2011).

[189] Michelman-Ribeiro, A., Boukari, H., Nossal, R., and Horkay, F. *Macromolecules* **37**(26), 10212–10214 (2004).

[190] Gianneli, M., Beines, P. W., Roskamp, R. F., Koynov, K., Fytas, G., and Knoll, W. *J. Phys. Chem. C* **111**(35), 13205–13211 (2007).

[191] Modesti, G., Zimmermann, B., Borsch, M., Herrmann, A., and Saalwachter, K. *Macromolecules* **42**(13), 4681–4689 (2009).

[192] Raccis, R., Roskamp, R., Hopp, I., Menges, B., Koynov, K., Jonas, U., Knoll, W., Butt, H. J., and Fytas, G. *Soft Matter* **7**(15), 7042–7053 (2011).

[193] Cherdhirankorn, T., Best, A., Koynov, K., Peneva, K., Muellen, K., and Fytas, G. *J. Phys. Chem. B* **113**(11), 3355–3359 (2009).

[194] Hwang, L. C. and Wohland, T. *Cell Biochem. Biophys.* **49**(1), 1–13 (2007).

[195] Landfester, K., Bechthold, N., Tiarks, F., and Antonietti, M. *Macromolecules* **32**(16), 5222–5228 (1999).

[196] Fickert, J., Rupper, P., Graf, R., Landfester, K., and Crespy, D. *J. Mater. Chem.* **22**(5), 2286–2291 (2012).

[197] Garcia a Moreno, I., Costela, A., Campo, L., Sastre, R., Amat-Guerri, F., Liras, M., Lopez Arbeloa, F., Banuelos Prieto, J., and Lopez Arbeloa, I. *J. Phys. Chem. A* **108**(16), 3315–3323 (2004).

[198] Petrasek, Z. and Schwille, P. *Biophys. J.* **94**(4), 1437–1448 (2008).

[199] Rao, J. P. and Geckeler, K. E. *Prog. Polym. Sci.* **36**(7), 887–913 (2011).

[200] Texter, J. *J. Dispers. Sci. Technol.* **22**(6), 499–527 (2001).

[201] Vitale, S. A. and Katz, J. L. *Langmuir* **19**(10), 4105–4110 (2003).

[202] Ganachaud, F. and Katz, J. L. *Chem. Eur. J. of Chem. Phys.* **6**(2), 209–216 (2005).

[203] Schubert, S., Delaney, Jr, J. T., and Schubert, U. S. *Soft Matter* **7**(5), 1581–1588 (2011).

[204] Crespy, D. and Landfester, K. *Macromol. Chem. Phys.* **208**(5), 457–466 (2007).

[205] O'Donnell, P. B. and McGinity, J. W. *Adv. Drug Deliver. Rev.* **28**(1), 25–42 (1997).

[206] Kietzke, T., Neher, D., Landfester, K., Montenegro, R., Guntner, R., and Scherf, U. *Nat. Mater.* **2**(6), 408–412 (2003).

[207] Fickert, J., Wohnhaas, C., Turshatov, A., Landfester, K., and Crespy, D. *Macromolecules* **46**(3), 573–579 (2013).

[208] Higuchi, T., Motoyoshi, K., Sugimori, H., Jinnai, H., Yabu, H., and Shimomura, M. *Macromol. Rapid Comm.*. **31**(20), 1773–1778 (2010).

[209] Okubo, M., Saito, N., Takekoh, R., and Kobayashi, H. *Polymer* **46**(4), 1151–1156 (2005).

[210] Saito, N., Kagari, Y., and Okubo, M. *Langmuir* **22**(22), 9397–9402 (2006).

[211] Tanaka, T., Nakatsuru, R., Kagari, Y., Saito, N., and Okubo, M. *Langmuir* **24**(21), 12267–12271 (2008).

[212] Tanaka, T., Saito, N., and Okubo, M. *Macromolecules* **42**(19), 7423–7429 (2009).

[213] Loxley, A. and Vincent, B. *J. Colloid Interf. Sci.* **208**(1), 49–62 (1998).

[214] Vauthier, C., Schmidt, C., and Couvreur, P. *J. Nanopart. Res.* **1**(3), 411–418 (1999).

[215] Goddeeris, C., Cuppo, F., Reynaers, H., Bouwman, W., and Van den Mooter, G. *Int. J. Pharm.* **312**(1-2), 187–195 (2006).

[216] Hadamard, J. S. *CR Acad. Sci.* **152**, 1735 (1911).

[217] Rybczynski, W. *Bull. Int. Acad. Sci. Cracovie, Ser. A* (1), 40–46 (1911).

[218] Sadhal, S. S. and Johnson, R. E. *J. Fluid Mech.* **126**, 237–250 (1983).

[219] Lowndes, J. *J. Fluid Mech.* **101**, 631–646 (1980).

[220] Carnie, S. L., Chan, D. Y. C., Lewis, C., Manica, R., and Dagastine, R. R. *Langmuir* **21**(7), 2912–2922 (2005).

[221] Dagastine, R. R., Manica, R., Carnie, S. L., Chan, D. Y. C., Stevens, G. W., and Grieser, F. *Science* **313**(5784), 210–213 (2006).

[222] Eigen, M. and Rigler, R. *Proc. Natl. Acad. Sci. USA* **91**(13), 5740–5747 (1994).

[223] Eastoe, J., Hetherington, K. J., Sharpe, D., Steytler, D. C., Egelhaaf, S., and Heenan, R. K. *Langmuir* **13**(9), 2490–2493 (1997).

[224] Di Venere, A., Nicolai, E., Rosato, N., Rossi, A., Finazzi Agro, A., and Mei, G. *FEBS J.* **278**(9), 1585–1593 (2011).

[225] Cherdhirankorn, T., Retsch, M., Jonas, U., Butt, H.-J., and Koynov, K. *Langmuir* **26**(12), 10141–10146 (2010).

[226] Turshatov, A. and Adams, J. *Polymer* **48**(26), 7444–7448 (2007).

[227] Turshatov, A., Adams, J., and Johannsmann, D. *Macromolecules* **41**(14), 5365–5372 (2008).

[228] Landfester, K., Montenegro, R., Scherf, U., Guntner, R., Asawapirom, U., Patil, S., Neher, D., and Kietzke, T. *Adv. Mater.* **14**(9), 651–655 (2002).

[229] Friedemann, K., Turshatov, A., Landfester, K., and Crespy, D. *Langmuir* **27**(11), 7132–7139 (2011).

[230] Busko, D., Baluschev, S., Crespy, D., Turshatov, A., and Landfester, K. *Micron* **43**(5), 583–588 (2012).

[231] Herrmann, C., Turshatov, A., and Crespy, D. *ACS Macro Lett.* **1**, 907–909 (2012).

[232] Crespy, D., Zuber, S., Turshatov, A., Landfester, K., and Popa, A. M. *Journal of Polymer Science Part a-Polymer Chemistry* **50**(6), 1043–1048 (2012).

[233] Lodge, T. P., Pudil, B., and Hanley, K. J. *Macromolecules* **35**(12), 4707–4717 (2002).

[234] Jain, S. and Bates, F. S. *Science* **300**(5618), 460–464 (2003).

[235] Halperin, A., Tirrell, M., and Lodge, T. P. *Adv. Polym. Sci.* **100**, 31–71 (1992).

[236] Li, Z. L. and Dormidontova, E. E. *Soft Matter* **7**(9), 4179–4188 (2011).

[237] Tian, M., Qin, A., Ramireddy, C., Webber, S. E., Munk, P., Tuzar, Z., and Prochazka, K. *Langmuir* **9**(7), 1741–1748 (1993).

[238] Willner, L., Poppe, A., Allgaier, J., Monkenbusch, M., and Richter, D. *Europhys. Lett.* **55**(5), 667–673 (2001).

[239] Lund, R., Willner, L., Stellbrink, J., Lindner, P., and Richter, D. *Phys. Rev. Lett.* **96**(6) (2006).

[240] Zinn, T., Willner, L., Lund, R., Pipich, V., and Richter, D. *Soft Matter* **8**(3), 623–626 (2012).

[241] Choi, S. H., Bates, F. S., and Lodge, T. P. *Macromolecules* **44**(9), 3594–3604 (2011).

[242] Lu, J., Choi, S., Bates, F. S., and Lodge, T. P. *ACS Macro Lett.* **1**(8), 982–985 (2012).

[243] Lu, J., Bates, F. S., and Lodge, T. P. *ACS Macro Lett.* **2**(5), 451–455 (2013).

[244] Jaskiewicz, K., Larsen, A., Schaeffel, D., Koynov, K., Lieberwirth, I., Fytas, G., Landfester, K., and Kroeger, A. *ACS Nano* **6**(8), 7254–7262 (2012).

[245] Lutz, J.-F. *Adv. Mater.* **23**(19), 2237–2243 (2011).

[246] Fowkes, F. M. *J. Phys. Chem.* **66**(2), 382 (1962).

[247] Li, I. T. S. and Walker, G. C. *J. Am. Chem. Soc.* **132**(18), 6530–6540 (2010).

[248] Chapman, B. R., Hamersky, M. W., Milhaupt, J. M., Kostelecky, C., Lodge, T. P., von Meerwall, E. D., and Smith, S. D. *Macromolecules* **31**(14), 4562–4573 (1998).

[249] Shibu, E. S., Sonoda, A., Tao, Z., Feng, Q., Furube, A., Masuo, S., Wang, L., Tamai, N., Ishikawa, M., and Biju, V. *ACS Nano* **6**(2), 1601–1608 (2012).

[250] Kwart, H. and Burchuk, I. *J. Am. Chem. Soc.* **74**(12), 3094–3097 (1952).

[251] Erdoğan, M., Hizal, G., Tunca, U., Hayrabetyan, D., and Pekcan, O. *Polymer* **43**(6), 1925–1931 (2002).

[252] Szymanski, J. and Weiss, M. *Physical Review Letters* **103**(3) (2009).

[253] Vagias, A., Raccis, R., Koynov, K., Jonas, U., Butt, H. J., Fytas, G., Kosovan, P., Lenz, O., and Holm, C. *Physical Review Letters* **111**(8) (2013).

[254] Cherdhirankorn, T., Harmandaris, V., Juhari, A., Voudouris, P., Fytas, G., Kremer, K., and Koynov, K. *Macromolecules* **42**(13), 4858–4866 (2009).

[255] Yang, J. F., Zhao, J., and Han, C. C. *Macromolecules* **41**(20), 7284–7286 (2008).

[256] Huber, K., Bantle, S., Lutz, P., and Burchard, W. *Macromolecules* **18**(7), 1461–1467 (1985).

[257] Termeer, H. U., Burchard, W., and Wunderlich, W. *Colloid and Polymer Science* **258**(6), 675–684 (1980).

[258] Press, W. H., Teukolsky, S. A., Vetterling, W. T., and Flannery, B. P. *Numerical Recipes: The Art of Scientific Computing*. Cambridge University Press, 3 edition, (2007).

[259] Schmitz, R., Yordanov, S., Butt, H.-J., Koynov, K., and DÃ¼nweg, B. *Phys. Rev. E* **84**, 066306 (2011).

B. List of Abbreviations

A	absorption
AIBN	2;2'Azobis(2-methylpropionitrile)
An-PS-POEGMA	anthracene-polystyrene-*block*-poly[oligo(ethylene glycol) methyl ether methacrylate]
APD	avalanche photo diode
CEF	collection efficiency function
CMC	critical micelle concentration
CONTIN	A constrained regularization method for inverting data represented by linear algebraic or integral equations.[50–52]
cryo-TEM	cryogenic transmission electron microscopy
CTMA-Cl	cetyltrimethylammonium chloride
CuBr	copper(I) bromide
DAD	diode array detector
DC FCCS	dual color fluorescence cross correlation spectroscopy
DCM	dichloromethane
DLS	dynamic light scattering
DLVO	Derjaguin; Verwey; Landau and Overbeek
DMF	dimethylformamid
DNA	deoxyribonucleic acid
EC	ethyl cellulose
fcFCS	full correlation fluorescence correlation spectroscopy
FCS	fluorescence correlation spectroscopy
FIDA	fluorescence intensity distribution analysis
FRET	fluorescence resonance energy transfer
GPC	gel permeation chromatography
HPLC	high pressure liquid chromatography
IC	internal conversion
IP	image plane
IR	infrared

MALDI TOF	matrix assisted laser desorption/ionization and time of flight
MDE	molecular detection efficiency
MEP	miniemulsion polymerization
MW	microwave
NA	numerical aperture
NC	nanocontainer
PLA	[1-(4-nitrophenyl)-2-pyrrolidinmethyl]
OEGMA	oligo(ethylene glycol) methyl ether methacrylate
PC	polycondensation
PCH	photon counting histogram
PDI	polydispersity index
PDMS-*b*-PMOXA	poly(dimethylsiloxane)-*block*-(2-methyloxazoline)
PLA	poly(lactic acid)
PMDTA	N;N;N';N';N"-pentamethyldiethylenetriamine
PMI	N-(2;6-diisopropylphenyl)-perylene-3;4-dicarbonacidimide
PS	polystyrene
PS-POEGMA	polystyrene-*block*-poly[oligo(ethylene glycol) methyl ether methacrylate]
PSF	point spread function
Q	quenching
RI	refractory index
RNA	ribonucleic acid
S	electronic state
SANS	small angle neutron scattering
SDS	sodium dodecyl sulfate
SEED	solvent evaporation from emulsion droplets
SEM	scanning electron microscopy
SiO_2	silicon dioxide
siRNA	small interfering ribonucleic acid
SPAD	single-photon-counting avalanche photo-diode
TCSPC	time correlated single photon counting
TEOS	tetraethyl orthosilicate
THF	tetrahydrofuran

TR-SANS	time resolved small angle neutron scattering
UV	ultraviolet
VdW	van der Waals
VIS	visual
PLA	9-vinylphenanthrene
WLF	Williams-Landel-Ferry

C. Acknowledgment

...

Scientific contributions

Publications

[1] D. Schaeffel, S. Yordanov, R.H. Staff, A. Kreyes, Y. Zhao, K. Landfester, J. Hofkens, H.-J. Butt, D. Crespy, K. Koynov: Measuring the molar mass dispersity of polymers with Fluorescence Correlation Spectroscopy, *submitted*

[2] M.A. Hood, U. Paiphansiri, D. Schaeffel, K. Koynov, M. Kappl, K. Landfester, R. Muñoz-Espi: Hybrid Poly(urethane urea)/Silica Nanocapsules with pH-Sensitive Regimes as a Controllable Destroyable Nanocontainer, *in preparation*

[3] L. Nuhn, L. Braun, I. Overhoff, A. Kelsch, D. Schaeffel, K. Koynov, R. Zentel: Degradable Cationic Nanohydrogel Particles for Stimuli-Responsive Release of siRNA, *submitted*

[4] J. Bühler, S. Gietzen, A. Reuter, C. Kappel, K. Fischer S. Decker, D. Schaeffel, K. Koynov, M. Bros, I. Tubbe S. Grabbe, K. Fischer, M. Schmidt: Selective Uptake of Clyindrical Poly(2-Oxazoline) Brush-AntiDEC205 Antibody OVA Antigen Conjugates into DEC-Positive Dendritic Cells and Subsequent T-Cell Activation, *Chem. Eur. J.*, **2014**, DOI: 10.1002/chem.201403942

[5] D. Schaeffel, A. Kreyes, Y. Zhao, K. Landfester, H.-J. Butt, D. Crespy, K. Koynov: Molecular Exchange Kinetics of Diblock Copolymer Micelles monitored by Fluorescence Correlation Spectroscopy, *ACS Macro Lett.*, **2014**, *3*(5), 428-432

[6] J. Fickert, D. Schaeffel, K. Koynov, K. Landfester, D. Crespy: Silica nanocapsules for redox-responsive deilvery, *Colloid Polym. Sci.*, **2014**, *292*(1), 251-255

[7] C. Moers, L. Nuhn, M. Wissel, R. Stangenberg, M. Mondeshki, E. Berger-Nicoletti, A. Thomas, D. Schaeffel, K. Koynov, M. Klapper, R. Zentel, H. Frey: Supramolecular Linear-*g*-hyperbranched Graft Polymers: Topology and Binding Strength of Hyperbranched Side-Chains, *Macromolecules*, **2013**, *46*(24), 9544-9553

[8] D. Weller, A. Medina-Oliva, H. Claus, S. Gietzen, K. Mohr, A. Reuter, D. Schaeffel, S. Schöttler, K. Koynov, M. Bros, S. Grabbe, K. Fischer, M. Schmidt: Solution Properties and Potential Biological Application of Zwitterionic Poly(ε-N-methacryloyl-L-lysine), *Macromolecules*, **2013**, *46*(21), 8519-8527

[9] R. H. Staff, D. Schaeffel, A. Turshatov, D. Donadio, H.-J. Butt, K. Landfester, K. Koynov, D. Crespy: Unraveling the Mechanism of Particle Formation in the Emulsion Solvent Evaporation Process, *Small*, **2013**, *9*(20), 3514-3522

[10] D. Schaeffel, S. Yordanov, M. Schmelzeisen, T. Yamamoto, M. Kappl, R. Schmitz, B. Dünweg, K. Koynov, H.-J. Butt: Hydrodynamic boundary condition of water on hydrophilic and hydrophobic surfaces, *Phys. Rev. E*, **2013**, *87*(5), 051001(R)

[11] S. Winzen, M. Bernhardt, D. Schaeffel, A. Koch, M. Kappl, K. Koynov, K. Landfester, A. Kroeger: Small unilamellar hybrid vesicles consisting of polymer-lipid and polymer-cholesterol blends, *Soft Matter*, **2013**, *9*(25), 5883-5890

[12] D. Pilat, P. Papadopoulos, D. Schaeffel, D. Vollmer, R. Berger, H.-J. Butt: Dynamic Measurement of the Force Required to Move a Liquid Drop on a Solid Surface, *Langmuir*, **2012**, *28*(49), 16812-16820

[13] D. Schaeffel, R. H. Staff, , H.-J. Butt, K. Landfester, D. Crespy, K. Koynov: Fluorescence Correlation Spectroscopy directly monitors coalescence during nanoparticles preparation, *Nano Lett.*, **2012**, *12*(11), 6012-6017

[14] K. Jaskiewicz, A. Larsen, D. Schaeffel, K. Koynov, G. Fytas, K. Landfester, A. Kroeger: Incorporation of Nanoparticles into Polymersomes: Size and Concentration Effects, *ACS Nano*, **2012**, *6*(8), 7254-7262

Oral presentations and posters

Oral presentation **88th ACS Colloids & Surface Science Symposium**, *Philadelphia, PA, USA*, June 2014.
"Direct monitoring of the exchange kinetics between diblock copolymer micelles by Fluorescence Correlation Spectroscopy"

Poster **11th International Symposium on Polymer Physics**, *Nanjing, Jiangsu, China*, June 2014.
"Measuring the Molar Mass Dispersity of Polymers with Fluorescence Correlation Spectroscopy"

Oral presentation **10th Zsigmondy Kolloquium**, *Konstanz*, April 2014.
"Direct monitoring of kinetic processes in polymer based colloidal systems by Fluorescence Correlation Spectroscopy"

Oral presentation **DPG Frühjahrstagung**, *Dresden*, March/April 2014.
"Fluorescence Correlation Spectroscopy Directly Monitors the Equilibrium Chain Exchange Kinetics of Diblock Copolymer Micelles"

Oral presentation **Workshop FCS in Polymer Science**, *Garching*, October 2013.
"Dual color FCCS directly monitors coalescence of nandroplets and the dynamic equilibrium exchange kinetics of copolymer micelles"

Oral presentation **87th ACS Colloids & Surface Science Symposium**, *Riverside, CA, USA*, June 2013.
"Fluorescence Correlation Spectroscopy as a tool to directly study coalescence during nanoparticle preparation"

Oral presentation **4th Bratislava Young Polymer Scientists workshop (BYPOS)**, *Lipovský Ján, Slovakei*, October 2012.
"Fluorescence Correlation Spectroscopy as a tool to directly study coalescence during nanoparticle preparation"

Oral presentation **26th Conference of the European Colloid and Interface Society (ECIS)**, *Malmö, Schweden*, September 2012.
"Measuring the boundary slip of water on smooth surfaces by total internal reflection fluorescence cross-correlation spectroscopy"

Poster **8th Zsigmondy Kolloquium**, *Darmstadt*, March 2012.
"Particle Formation by the Emulsion-Solvent Evaporation Technique: A Comprehensive Study"